Evolution of divergent and strike-slip boundaries in response to surface processes

---

Derek Neuharth

Kumulative Dissertation

zur Erlangung des akademischen Grades

"doctor rerum naturalium"

(Dr. rer. nat.)

in der Wissenschaftsdisziplin "Geowissenschaften"

eingereicht an der

Mathematisch-Naturwissenschaftlichen Fakultät

Institut für Geowissenschaften

der Universität Potsdam

und

Sektion 2.5: Geodynamische Modellierung

Deutsches GeoForschungsZentrum Potsdam

Ort und Tag der Disputation: Potsdam, 21/3/2022

BetreuerInnen
1. Dr. Sascha Brune, GFZ Potsdam, Universität Potsdam
2. Dr. Stephan Sobolev, GFZ Potsdam, Universität Potsdam

Gutachter
1. Dr. Sascha Brune, GFZ Potsdam, Universität Potsdam
2. Dr. John Naliboff, New Mexico Tech
3. Dr. Laetitia Le Pourhiet, Sorbonne Université

Published online on the
Publication Server of the University of Potsdam:
https://doi.org/10.25932/publishup-43571
https://nbn-resolving.org/urn:nbn:de:kobv:517-opus4-435713

Abstract

Plate tectonics describes the movement of rigid plates at the surface of the Earth as well as their complex deformation at three types of plate boundaries: 1) divergent boundaries such as rift zones and mid-ocean ridges, 2) strike-slip boundaries where plates grind past each other, such as the San Andreas Fault, and 3) convergent boundaries that form large mountain ranges like the Andes. The generally narrow deformation zones that bound the plates exhibit complex strain patterns that evolve through time. During this evolution, plate boundary deformation is driven by tectonic forces arising from Earth's deep interior and from within the lithosphere, but also by surface processes, which erode topographic highs and deposit the resulting sediment into regions of low elevation. Through the combination of these factors, the surface of the Earth evolves in a highly dynamic way with several feedback mechanisms. At divergent boundaries, for example, tensional stresses thin the lithosphere, forcing uplift and subsequent erosion of rift flanks, which creates a sediment source. Meanwhile, the rift center subsides and becomes a topographic low where sediments accumulate. This mass transfer from foot- to hanging wall plays an important role during rifting, as it prolongs the activity of individual normal faults. When rifting continues, continents are eventually split apart, exhuming Earth's mantle and creating new oceanic crust. Because of the complex interplay between deep tectonic forces that shape plate boundaries and mass redistribution at the Earth's surface, it is vital to understand feedbacks between the two domains and how they shape our planet.

In this study I aim to provide insight on two primary questions: 1) How do divergent and strike-slip plate boundaries evolve? 2) How is this evolution, on a large temporal scale and a smaller structural scale, affected by the alteration of the surface through erosion and deposition? This is done in three chapters that examine the evolution of divergent and strike-slip plate boundaries using numerical models. *Chapter 2* takes a detailed look at the evolution of rift systems using two-dimensional models. Specifically, I extract faults from a range of rift models and correlate them through time to examine how fault networks evolve in space and time. By implementing a two-way coupling between the geodynamic code ASPECT and landscape evolution code FastScape, I investigate how the fault network and rift evolution are influenced by the system's erosional efficiency, which represents many factors like lithology or climate. In *Chapter 3*, I examine rift evolution from a three-dimensional perspective. In this chapter I study linkage modes for offset rifts to determine when fast-rotating plate-boundary structures known as continental microplates form. *Chapter 4* uses the two-way numerical coupling between tectonics and landscape evolution to investigate how a strike-slip boundary responds to large sediment loads, and whether this is sufficient to form an entirely new type of flexural strike-slip basin.

Zusammenfassung

Plattentektonik beschreibt die Bewegung starrer tektonischer Platten an der Erdoberfläche sowie deren komplexe Deformation an drei Arten von Plattengrenzen: 1) divergenten Grenzen wie Grabenbrüchen und mittelozeanische Rücken, 2) transversalen Grenzen, an denen Platten gegeneinander verschoben werden, wie die San-Andreas-Verwerfung, und 3) konvergenten Grenzen, die große Gebirgszüge wie die Anden bilden. Diese schmalen Deformationszonen, die Platten begrenzen, weisen meist komplexe Dehnungsmuster auf, die sich im Laufe der Zeit entwickeln. Während dieser Entwicklung wird die Verformung der Plattengrenzen durch tektonische Kräfte aus dem tiefen Erdinneren und der Lithosphäre, aber auch durch Oberflächenprozesse, welche topografische Erhebungen erodieren und die daraus resultierenden Sedimente in tiefer gelegenen Gebieten ablagern, angetrieben. Durch das Zusammenwirken und die Rückkopplung dieser Faktoren entwickelt sich die Erdoberfläche in einer extrem dynamischen Art und Weise. An divergenten Grenzen beispielsweise dünnen Zugspannungen die Lithosphäre aus, was zu einer Hebung und anschließenden Erosion der Flanken eines Grabenbruchs führt, wobei wiederum Sedimente freigesetzt werden. Währenddessen sinkt das Zentrum des Grabens ab und wird zu einer topografischen Senke, in der sich Sedimente ablagern. Diese Massenumverteilung vom Fuß zum Hang einer Verwerfung spielt eine wichtige Rolle, da er die Aktivität einzelner Verwerfungen verlängert. Durch anhaltende Divergenz werden Kontinente schließlich auseinandergerissen, wodurch der Erdmantel an die Erdoberfläche gefördert und neue ozeanische Kruste gebildet wird. Aufgrund des komplexen Zusammenspiels zwischen tektonischen Kräften aus dem tiefen Erdinneren und der Massenumverteilung an der Erdoberfläche ist es von entscheidender Bedeutung, die Rückkopplungen zwischen diesen beiden Bereichen zu verstehen.

In dieser Studie möchte ich Einblicke zu zwei Hauptfragen geben: 1) Wie entwickeln sich divergierende Plattengrenzen? 2) Wie wird diese Entwicklung auf einer großen zeitlichen und einer kleinen strukturellen Skala durch die Veränderung der Oberfläche durch Erosion und Sedimentation beeinflusst? In drei Kapiteln untersuche ich die Entwicklung von divergenten und streichenden Plattengrenzen anhand numerischer Modelle. In Kapitel 2 wird die Entwicklung von Grabenbrüchen anhand zweidimensionaler Modelle im Detail erforscht. Dabei extrahiere ich Verwerfungen aus einer Reihe von Modellen und korreliere sie über die Zeit, um zu untersuchen, wie sich Verwerfungsnetzwerke räumlich und zeitlich entwickeln. Durch die bidirektionale Kopplung des Geodynamik-Codes ASPECT und des Erdoberflächen-Codes FastScape untersuche ich, wie diese Verwerfungsnetzwerk und der Grabenbruch im Allgemeinen durch die Erosionseffizienz des Systems, welche viele Faktoren wie Lithologie oder Klima abbildet, beeinflusst werden. In Kapitel 3 untersuche ich die Entwicklung eines Grabenbruchs aus einer dreidimensionalen Perspektive. In diesem Kapitel analysiere ich wie sich gegeneinander versetzte Grabenbrüche verbinden und wann sich dabei schnell rotierende kontinentale Mikroplatten bilden. In Kapitel 4 nutze ich die entwickelte bidirektionale Kopplung zwischen Geodynamik und Erdoberflächenprozessen, um zu verstehen, wie transversale Plattengrenzen auf Sedimentlasten reagieren und ob die ausreicht, um einen völlig neue Art von Sedimentbecken in dieser Umgebung zu formen.

Declarations of Author Contributions

In this thesis, Chapters 2, 3, and 4 consist of studies that are either in review (Chapter 2) or published (Chapter 3 and 4). The author contribution for each of these studies is as follows:

Chapter 2: Neuharth, D., Brune, S., Wrona, T., Glerum, A., Braun, J., and Yuan, X.P., (in review at Tectonics), Evolution of rift systems and their fault networks in response to surface processes.

- *Derek Neuharth* – Coded the ASPECT-FastScape coupling. Setup and ran numerical models. Interpreted the results, created the figures, and wrote the manuscript text.
- *Sascha Brune* – Provided supervision for the ASPECT-FastScape coupling, and helped interpret the results, write, and edit the text.
- *Thilo Wrona* – Coded the Fatbox python code used in the study, provided supervision, and helped interpret the results, write, and edit the text.
- *Anne Glerum* - Provided supervision for the ASPECT-FastScape coupling, and helped interpret the results, write, and edit the text.
- *Xiaoping Yuan* – Helped with the ASPECT-FastScape coupling and text edits/comments.
- *Jean Braun* - Helped with the ASPECT-FastScape and text edits/comments.

Chapter 3: Neuharth, D., Brune, S., Glerum, A., Heine, C., and Welford, K., 2021, Formation of continental micropalts through rift linkage: numerical modeling and its application to the Flemish Cap and Sao Paulo Plateau: Geochemistry, Geophysics, Geosystems, v. 22. Doi:10.1029/2020GC009615

- *Derek Neuharth* – Setup and ran the numerical models. Interpreted the results, created the figures, and wrote the manuscript text.
- *Sascha Brune* – Provided supervision, and helped interpret the results, write, and edit the text.
- *Anne Glerum* - Provided supervision, and helped interpret the results, write, and edit the text.
- *Christian Heine* – Provided data and helped interpret and write the Sao Paulo Plateau section and edit the text.
- *J. Kim Welford* – Provided data and helped interpret and write the Flemish Cap section and edit the text.

Chapter 4: Neuharth D., Brune, S., Glerum, A., Morley, C.K., Yuan, X.P., and Braun, J., 2021, Flexural strike-slip basins: Geology, doi: https://doi.org/10.1130/G49351.1

- *Derek Neuharth* –Setup and ran the numerical models. Interpeted the results, created the figures, and wrote the manuscript text.
- *Sascha Brune* – Provided supervision, and helped interpret the results, write, and edit the text.
- *Anne Glerum* - Provided supervision, and helped interpret the results, write, and edit the text.
- *Chris K. Morley* – Provided data and helped interpret and write the Andaman Sea sections and edit the text.
- *Xiaoping Yuan* – Helped with the Fastscape portion of the text and edits/comments.
- *Jean Braun* - Helped with the Fastscape portion of the text and edits/comments.

Table of contents

List of Figures

List of Tables

List of Symbols and Abbreviations

Parameter	Symbol	Unit
ASPECT		
Thermal expansivity	α	K^{-1}
Thermal diffusivity	κ	$m^2\ s^{-1}$
Thermal conductivity	k	$W\ m^{-1}\ K^{-1}$
Heat capacity	C_p	$J\ kg^{-1}\ K^{-1}$
Heat production	H	$W\ m^{-3}$
Cohesion	C	Pa
Internal friction angle (unweakened)	ϕ	◦
Plastic strain weakening factor	ϕ_{wf}	-
Stress exponent (dis)	n	-
Constant prefactor (dis)	A_{dis}	$Pa^{-n}\ s^{-1}$
Activation energy (dis)	E_{dis}	$J\ mol^{-1}$
Activation volume (dis)	V_{dis}	$m^3\ mol^{-1}$
Constant prefactor (diff)	A_{diff}	$Pa^{-1}\ s^{-1}$
Activation energy (diff)	E_{diff}	$J\ mol^{-1}$
Activation volume (diff)	V_{diff}	$m^3\ mol^{-1}$
Grain size (diff)	d	m
Grain size exponent (diff)	m	-
Gas constant	R	$J\ K^{-1}\ mol^{-1}$
gravity	$\boldsymbol{g}$	$m\ s^{-2}$
velocity	$\boldsymbol{u}$	$m\ yr^{-1}$
Strain rate tensor	$\dot{\varepsilon}$	s^{-1}
Temperature	T	K
Viscosity	η	Pa s
Effective viscosity	η_{eff}	Pa s
Pressure	P	Pa
Density	ρ	$kg\ m^{-3}$
Reference adiabatic density	$\bar{\rho}$	$kg\ m^{-3}$
Time	t	yr
Compositional field	c_i	-
Reaction rate	q_i	-
FastScape and coupling		
Drainage area exponent	m	-
Slope exponent	n	-
Bedrock/sediment diffusivity	K_c	m^2/yr
Bedrock/sediment erodibility	K_f	$m^{0.2}/yr$
Bedrock/sediment deposition coefficient	G	-
Marine diffusivity	K_m	m^2/yr
Sand/shale ratio	F	-
Sand/shale porosity	φ	-
Sand/shale e-folding depth	z	m
Depth averaging thickness	L	m
Uplift rate	U	$m\ yr^{-1}$
Topographic elevation	h	m
Drainage area	A	m^2
Lateral velocity	$\boldsymbol{v}$	$m\ yr^{-1}$
Vertical mesh velocity	$\boldsymbol{V_z}$	$m\ yr^{-1}$
Current surface height	h_f	m
Previous surface height	h_p	m
ASPECT timestep	dt_a	yr

Abbreviation	Explanation
ABCF	Andaman Basin Central Fault
AR	Abimael Ridge
ASPECT	Advanced Solver for Problems in Earth's ConvecTion
ASSC	Andaman Sea Spreading Center
BP	Bonavista Platform
CFB	Cabo Frio-Benguela Fracture zone
EAB	East Andaman Basin
FC	Flemish Cap
FFz	Florianopolis Fracture zone
GB	Grand Banks
LAB	Lithosphere Asthenosphere Boundary
LC	Lower Crust
MC	Middle Crust
NL	Newfoundland
OB	Orphan Basin
OK	Orphan Knoll
SP	Surface Processes
SPL	Stream Power Law
SPP	Sao Paulo Plateau
SRTM	Shuttle Radar Tomography Mission
TC	Tristan da Cunha
UC	Upper Crust

Chapter 1 : Introduction

Earth surface deformation primarily occurs in narrow boundaries between evolving lithospheric plates. The movement of plates described in plate tectonics can happen in three ways that are responsible for the creation or destruction of plate material: 1) Plate divergence forms new plate material (Fig 1.1). When a plate is pulled apart, the lithosphere thins creating a rift, a process responsible for splitting apart continents. 2) Strike-slip motion where plates are neither destroyed nor created but grind past each other creates large shear forces along transform boundaries (e.g., the San Andreas Fault; Powell and Weldon, 1992). 3) Plate convergence effectively consumes plates at convergent margins, where plates can subduct into the mantle and compress continental crust forming large mountain ranges (e.g., the Himalayas; Le Fort, 1975). Through the creation and destruction of plate material, and through shifts in plate movement related to the Earth's convection, the plate boundaries evolve. Studying the underlying processes that control widespread plate boundary evolution, and the smaller scale mechanisms (e.g., faulting) that facilitate rock deformation is thus vital to understand our planet.

Plate tectonics can explain the first order evolution of our planet's surface, but it is not the only factor that deforms the Earth's surface. The surface also interacts with the atmosphere, where topographic highs are weathered and eroded, creating sediments. These sediments are carried to areas of low elevation, where they are deposited forming sedimentary basins (Allen and Allen, 2013). This landscape evolution caused by surface processes redistributes loading at the surface and is an important factor in the mechanisms and structures along all types of plate boundaries. For example, at subduction zones deposited sediment can help lubricate the subducting plate, possibly increasing the subduction rate (Lamb and Davis, 2003; Sobolev and Brown, 2019). At strike-slip boundaries, sedimentation can force plate flexure along the weakened boundary and form flexural strike-slip basins (Mahattanachai et al., 2021). Along rift zones, rift flanks are eroded as they are uplifted and the resulting sediments are deposited within the central graben, promoting fault activity (e.g., Andrés-Martínez et al., 2019). Thus, it is important to not only understand the large-scale evolution of the Earth's surface through interaction between its interior and the stronger lithosphere, but also through changes to the Earth's surface from erosion and deposition, where regional differences in the climate and rock lithology affect the efficiency of surface processes and determine how quickly the surface moves up or down.

Earth surface evolution occurs over timescales of millions of years; thus, it is not possible to directly witness how the surface changes through time. Using observational data from sources such as seismic data along rifted margins (Lymer et al., 2019), seafloor spreading related magnetic anomalies (Purucker and Dyment, 2000), and field outcrop observations, we can get snapshots of different evolutionary stages from the rock record. However, this record can have significant gaps, requiring interpretations. Numerical modeling software provides a tool to fill these gaps by accounting for physical laws (e.g., conservation of mass and momentum) and by incorporating rheological constraints (e.g., Mohr-Coulomb or Drucker-Prager failure). Utilizing the framework provided by observational data and information about how rocks deform under certain pressure-temperature conditions, we can set up tectonic models that

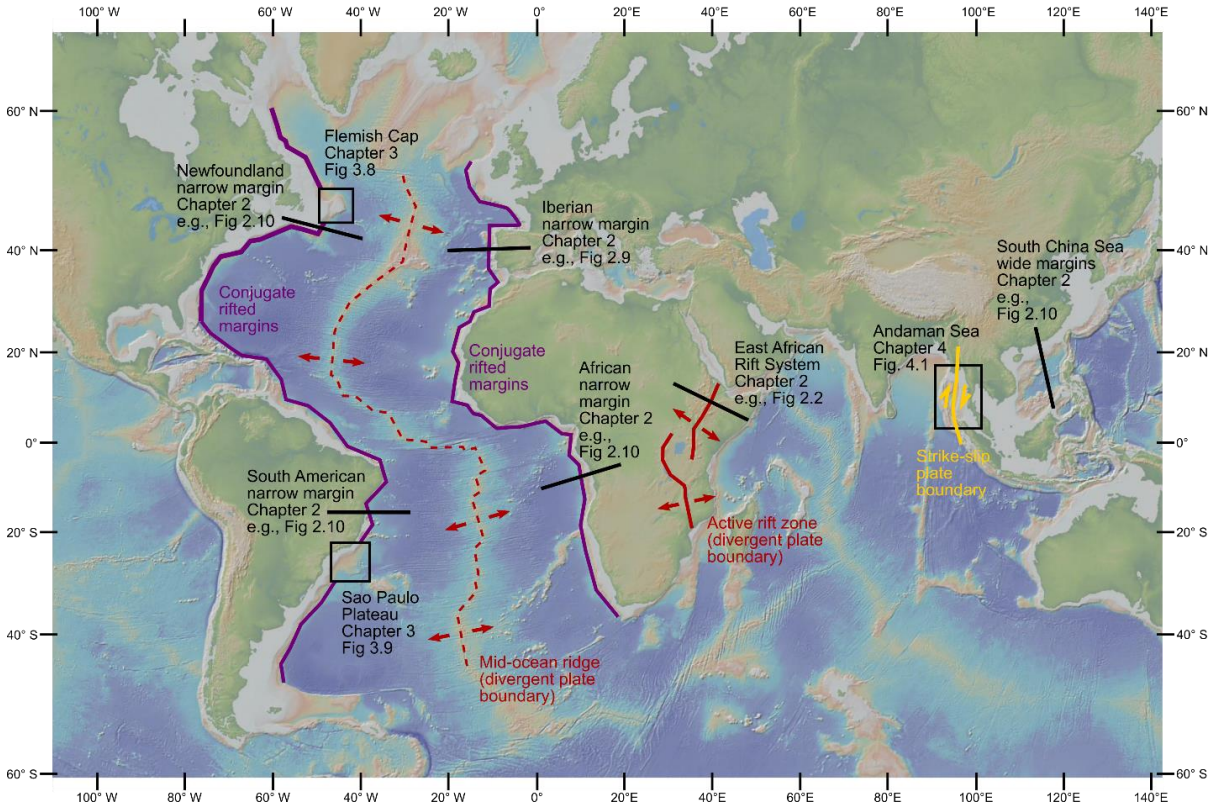

Figure 1.1 Overview figure showing selected divergent plate boundaries (red) and their associated rifted margins (purple), and strike-slip boundaries (yellow). Regions specific to the chapters are shown in black boxes or with black lines for 2D studies. The background image was created with GeoMapApp (Ryan et al., 2009).

evolve according to a set of rules that mimic the Earth (e.g., codes like ASPECT, Kronbichler et al., 2012; Heister et al., 2017; pTatin3D, May et al., 2014, 2015; LaMEM, Kaus et al., 2016; Underworld, Mansour et al., 2020). This provides a dynamic way to see how an Earth-like system evolves through time and under what conditions specific real-world features form. Using such numerical models, we can test the viability of geological interpretations made to explain observational data.

Numerical models help to validate interpretations made from observations, and said observations are required to test the predictive value of the model in replicating Earth-like deformation and features. For the first-order evolution of the Earth's surface through mantle convection and plate tectonics, it is important to compare modelled geological features to those seen along plate boundaries, such as fault activity patterns seen in active rifts like the East African Rift System (Corti, 2012; Glerum et al., 2020) or deformation patterns along passive margins that describe the history of rift deformation from initiation to continental breakup (Chenin et al., 2021). However, without erosion and deposition tectonic models often produce unrealistic topographies. Thus, including processes that shape the Earth's surface in models through the use of a landscape evolution code (e.g., FastScape, Braun and Willett, 2013; Badlands, Salles, 2016) becomes important. The inclusion of surface processes helps us produce more realistic topographies and allows us to compare sedimentary basins formed within our models to those in nature.

In this thesis I link mantle-lithosphere interactions with surface processes to explore how divergent and strike-slip plate boundaries subjected to erosion and deposition evolve through time. I achieve this by implementing a new two-way coupling between two codes: 1) the

tectonic code ASPECT that describes the mechanics and evolution of the mantle and lithosphere, and 2) the landscape evolution code FastScape that describes changes to the Earth's surface through the erosion and deposition of surface material. This thesis investigates the evolution of rift fault-systems in response to varying levels of surface process efficiency (*Chapter 2*), the large-scale interaction between offset rift segments and the geologic features they form (e.g., microplates; *Chapter 3*), and the formation of a new type of flexural strike-slip basin from sedimentation along a strike-slip fault (*Chapter 4*). The predictive value of the models is showcased through comparisons to geological observations such as crustal thickness and fault-structure related structural domains seen in seismic data along rifted margins (Lavier and Manatschal, 2006; Peron-Pinvidic et al., 2013), remnant continental microplates found along passive margins (e.g., the Flemish Cap, Welford et al., 2012), and a likely flexural strike-slip basin that formed in the Andaman Sea along an active strike-slip fault (Mahattanachai et al., 2021).

1.1 Rifts and rifted continental margins

In the early stages of divergent boundaries, continents are broken apart through the process of continental rifting (Dunbar and Sawyer, 1988). Rifting occurs as far-field stresses (McKenzie, 1978) or local buoyancy forces (e.g., Stamps et al., 2010) extend a lithospheric plate. A major mechanism during rifting is lithospheric necking, where deformation is focused in a small region of the lithosphere (Buck, 2015). As the region is stretched through a combination of ductile and brittle deformation, the lithosphere thins accommodating the upwelling warm asthenosphere and simultaneously forming large topographic lows at the surface. Eventually, the asthenosphere is exhumed at the surface signifying continental breakup and the start of seafloor spreading, wherein oceanic crust forms through decompression melting (Fig. 1.2a).

Using two-dimensional numerical models, we can examine rifting from initiation to continental breakup in detail. Many studies have investigated rift mechanics and found that rifts progress through different phases of deformation (Naliboff et al., 2017; Chenin et al., 2021) that produce distinct structural domains based on their crustal thicknesses (Fig 1.2b; Lavier and Manatschal, 2006; Peron-Pinvidic et al., 2013). These domains can be seen in seismic images of rifted margins around the globe. Additionally, numerical models that include sedimentation and its effect on the small-scale faults that dismember the crust as it thins demonstrate that sediment loading affects faults, when uplifted rift flanks are eroded and sediment is deposited into the central graben (Andrés-Martínez et al., 2019; Theunissen and Huismans, 2019). However, these studies evaluate fault growth qualitatively and thus may miss small quantitative changes of fault systems through time. In *Chapter 2* I quantitatively investigate how fault networks in a rift system evolve during different deformation phases and how these phases respond to varying levels of surface process efficiency. Moreover, I take a detailed look into the mechanics responsible for rift migration and the formation of asymmetric margins (Fig 1.1).

Two-dimensional modelling can explore the mechanisms of rifting in detail, however, as Earth's rifts exhibit along-strike heterogeneity, it is important to model how rifts evolve in three dimensions. Due to crustal and lithospheric heterogeneity (e.g., mantle scarring, Heron et al., 2019), rifts responding to the same forces may form at offsets of hundreds of kilometers.

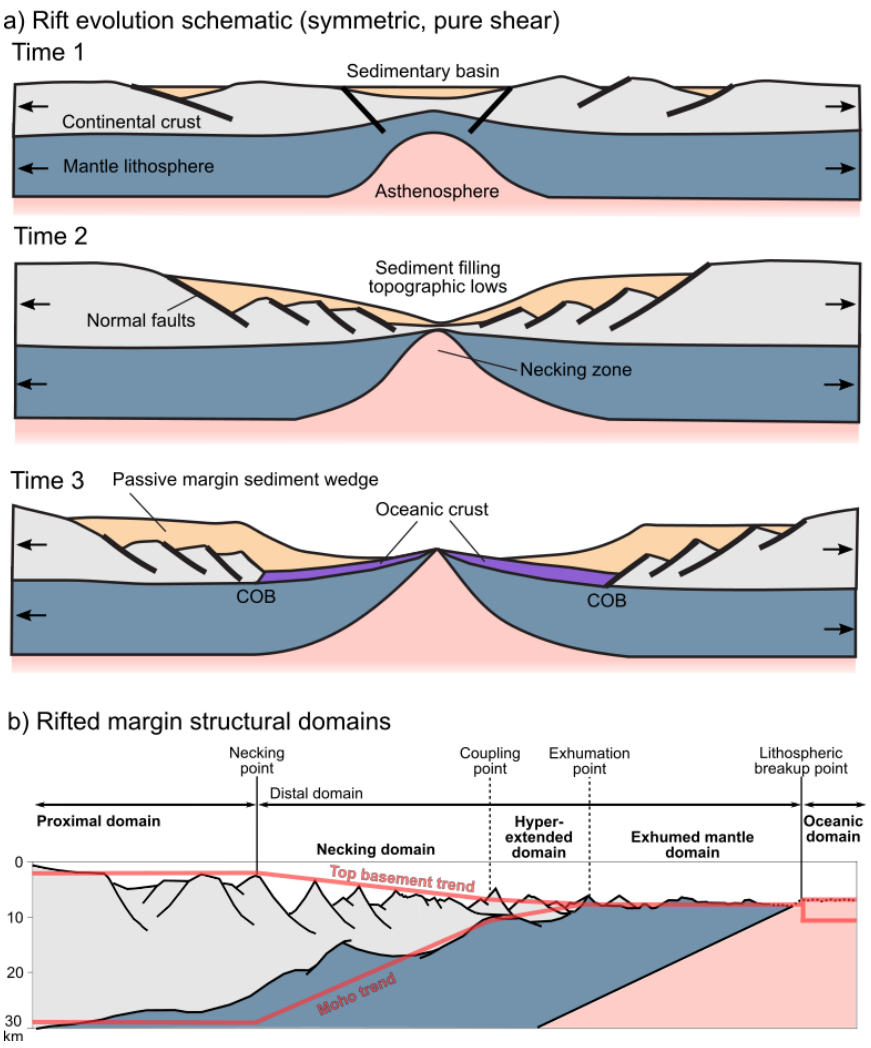

Figure 1.2 Examples of rift evolution. a) Schematic of symmetric rift evolution with sediment infill, showing the initial thinning of the lithosphere at time 1 until continental breakup and the formation of oceanic crust at time 3 (modified from Allen and Allen, 2013). b) Schematic of a rifted margin following a rifting event, divided into different structural domains. (modified from Chenin et al., 2021).

Continental margins give us glimpses on how such rifts connected in the past, but they cannot demonstrate why these rifts connected as they did. Numerical and analog models of 3D rift systems have been used to research how offset rifts in either crustal (Allken et al., 2011, 2012; Zwaan et al., 2016) or lithospheric scale models link (Tentler and Acocella, 2010; Le Pourhiet et al., 2017). They showed that depending on e.g., the strike-perpendicular offset, and in the case of analog models, the strike-parallel offset, rifts can link through oblique or strike-slip rift segments. In some cases, the offset rifts even overlap and rotate the central region between them. Such rotated structures are seen in oceanic (e.g., Easter Microplate, Naar and Hey, 1991) and continental (Victoria microplate, Glerum et al., 2020) crust and are referred to as microplates. While we see modern examples of these microplates, the conditions for their formation in continental crust are not well understood. In *Chapter 3* I therefore explore how offset rift segments link given different 3D geometric and crustal configurations, and under what conditions continental microplates form.

1.2 Strike-slip boundaries

Strike-slip boundaries describe regions like the San Andreas fault, where two plates grind past each other (Powell and Weldon, 1992). Like the divergent plate boundaries before, transform boundaries are not linked in straight lines, but are instead made up of multiple offset segments that accommodate shear forces between the plates. Depending on the segment orientation, the region between these segments is either compressed (restraining bend; McClay and Bonora, 2001) or extended (releasing bend; Mann et al., 1983), forming two major strike-slip features: flower structures and pull-apart basins. Pull apart basins are the only major basin type associated with transform boundaries and form at releasing bends where the region between offset segments is extended.

Sedimentary basins form through the creation of accommodation space where sediment accumulates. Pull-apart basins may be the only well-characterized major basin type along strike-slip boundaries, however, at other boundaries multiple types of basins form and these can be categorized based on how accommodation space is created: through 1) lithospheric thinning and cooling, or through 2) lithospheric flexure (Allen and Allen, 2013). Pull-apart basins belong to the former category, where extension forces thin the lithosphere leading to subsidence in the region. The latter category contains foreland basins where large tectonic loads flex the lithosphere downward creating accommodation space. However, strike-slip boundaries are known to be highly weakened boundaries (Zoback et al., 1987; Provost and Houston, 2003), which in some cases form in areas where stretching and subsidence have led to high sedimentation. Because of these factors, the question arises: How do weak strike-slip boundaries respond to large sediment loads? In *Chapter 4* I set up a submerged strike-slip model analogous to the Andaman Basin Central Fault in the Andaman Sea (Fig 1.1; Mahattanachai et al., 2021) and explore strike-slip fault mechanics when subjected to varying amounts of sediment.

Chapter 2 : Evolution of rift systems and their fault networks in response to surface processes

An updated manuscript version of this study was published in:
Neuharth, D., Brune, S., Wrona, T., Glerum, A., Braun, J., & Yuan, X. (2022). Evolution of rift systems and their fault networks in response to surface processes. *Tectonics*, 41, e2021TC007166. https://doi.org/10.1029/2021TC007166

Supplementary animations can be found at: https://doi.org/10.1029/2021TC007166

Abstract

Continental rifting is responsible for the generation of major sedimentary basins, both during rift inception and during the formation of rifted continental margins. Geophysical and field studies revealed that rifts feature complex networks of normal faults but the factors controlling fault network properties and their evolution are still matter of debate. Here, we employ high-resolution 2D geodynamic models (ASPECT) including two-way coupling to a surface processes code (FastScape) to conduct 12 models of major rift types that are exposed to various degrees of erosion and sedimentation. We further present a novel quantitative fault analysis toolbox (Fatbox), which allows us to isolate fault growth patterns, the number of faults, and their length and displacement throughout rift history. Our analysis reveals that rift fault networks may evolve through five major phases: 1) distributed deformation and coalescence, 2) fault system growth, 3) fault system decline and basinward localization, 4) rift migration, and 5) breakup. These phases can be correlated to distinct rifted margin domains. Models of asymmetric rifting suggest rift migration is facilitated through both ductile and brittle deformation within a weak exhumation channel that rotates subhorizontally and remains active at low angles. In sedimentation-starved settings, this channel satisfies the conditions for serpentinization. We find that surface processes are not only able to enhance strain localization and to increase fault longevity but that they also reduce the total length of the fault system, prolong rift phases and delay continental breakup.

2.1 Introduction

Rift-related thinning of the crust generates major depressions that are often filled with sediments. These sedimentary basins may provide a range of georesources such as geothermally exploitable hot aquifers (Jolie et al., 2021), ore deposits (Wilkinson, 2014), or perhaps even natural hydrogen (Lefeuvre et al., 2021). Our understanding of the processes that shape rifts, rifted margins, and their sedimentary basins is however inhibited among others by three challenges: (1) the cross-scale nature of deformation processes, (2) the interaction between faults and surface processes, (3) the interplay between complex mechanisms that facilitate rift migration. In the next paragraphs we describe these challenges by summarizing the current knowledge and its limits.

Rifting is an inherently cross-scale process. Normal faults that accommodate most of the extension in many rifts worldwide feature a width ranging from several centimeters to tens of meters (Scholz, 2019). Spacing in-between major normal faults can vary from 1 km (Muirhead et al., 2016) up to a few tens of kilometers (Whitmarsh et al., 2001). The extending lithosphere,

however, is typically hundreds of kilometers thick. Bridging these scales by means of geodynamic modelling tools remains a major challenge, even if fault localization processes are parameterized and if additional processes like melt generation and diking are neglected. Recent advances in computational techniques allowed for a steadily growing resolution of numerical rift models that lead to insights on rift migration processes (Brune et al., 2014), deformation phases (Naliboff et al., 2017), and fault-related unconformities (Pérez-Gussinyé et al., 2020). But deducing the evolution of variables that describe the kinematics of discrete faults like instantaneous slip rate, cumulative displacement or the number of active faults has remained very difficult in lithospheric-scale models so far.

One of the key factors shaping rift and rifted margin architectures are surface processes (e.g. Gawthorpe and Leeder, 2000; Clerc et al., 2018). Topographic erosion and sediment deposition modify Earth's surface through time, changing upper crustal temperatures and affecting crustal pressure conditions through sediment loads (e.g., Olive et al., 2014). The change in loading is an important factor for the evolution of individual faults, where mass redistribution from the uplifted and eroding footwall to the subsiding depositional hanging wall aids strain localization (Maniatis et al., 2009) and prolongs fault activity (Andrés-Martínez et al., 2019; Theunissen and Huismans, 2019; Beucher and Huismans, 2020). Similarly, sedimentation promotes rift migration by enhancing hyperextension of the crust and possibly delays continental breakup (Buiter, 2021). Previous studies have used 2D numerical models to investigate the interplay between surface processes and rift evolution (Andrés-Martínez et al., 2019; Theunissen and Huismans, 2019; Beucher and Huismans, 2020; Pérez-Gussinyé et al., 2020). These studies take a qualitative look at changes to rift system evolution, but do not quantitatively analyze variations in fault properties over time. Three-dimensional analog models suggest that surface processes do not have a large effect on overall rift evolution, but do affect the internal structure of rifts and produce more realistic rift geometries (Zwaan et al., 2018). These points highlight the importance of a quantitative fault analysis to understand the geometry and kinematics of fault networks, and how they evolve for varying degrees of surface process efficiency.

Previous numerical studies have shown a striking similarity in rift evolution when modeling rift migration, crustal hyper-extension and the formation of asymmetric rifted margins (Brune et al., 2014; Jammes and Lavier, 2016; Tetreault and Buiter, 2018; Pérez-Gussinyé et al., 2020). Comparing these models to concepts based on geophysical data, however, has led to discrepancies resulting in ongoing discussions on the mechanisms responsible (Lymer et al., 2019). The debate focusses on two issues: 1) Are key normal faults active at the same time (Sibuet, 1992; McDermott and Reston, 2015), or is faulting sequential such that a given fault will become extinct before a new one forms (Goldsworthy and Jackson, 2001; Ranero and Pérez-Gussinyé, 2010)? 2) Do basal detachment faults exist and slip at low angles (Reston and Pérez-Gussinyé, 2007; Lymer et al., 2019), or did they form as steeply dipping normal faults that were rotated passively similar to a rolling hinge (Buck, 1988; Choi et al., 2013)? It has been suggested that for slip to occur at low-angles weak rocks like serpentine are needed (Pérez-Gussinyé et al., 2001). Serpentinization of exhumed mantle rocks occurs in the presence of large amounts of seawater, requiring active faults within a thin portion of an entirely brittle crust (<10 km; Reston and Pérez-Gussinyé, 2007; Reston, 2010; Bayrakci et al., 2016; Muldashev et al., 2021). Assessing these factors requires both high-resolution models to determine the mechanisms that influence rift migration, and a way to quantitatively evaluate slip and activity time along discrete faults.

In this study we address three primary questions: 1) How do fault networks evolve in different rifts and rifted margins? 2) How are fault systems affected by surface processes? 3) How do detachment faults and fault sequentiality evolve during rift migration? We first describe the setup of our geodynamic model that pairs the tectonic code ASPECT with the landscape evolution code FastScape. We then introduce a new toolbox to extract discrete faults from our model results, track them through time and compute key fault properties such as the number of faults, slip, displacement, and fault length. We focus on three distinct rift settings to describe the joint evolution of fault networks and sedimentation patterns. Finally, we highlight new insights into fault sequentiality, deformation processes and serpentinization at rifted margins.

2.2 Methods

We use a two-way coupling between the geodynamic code ASPECT (Advanced Solver for Problems in Earth's ConvecTion; version 2.3.0-pre, commit e27f643; Kronbichler et al., 2012; Heister et al., 2017; Rose et al., 2017; Glerum et al., 2018; Gassmöller et al., 2018) and the landscape evolution model FastScape (version fastscapelib-fortran, commit 18f2588; Braun and Willett, 2013; Yuan et al., 2019a, 2019b) to simulate a 2D extensional system with erosion and sediment deposition.

2.2.1 Geodynamic model

The geodynamic code ASPECT assumes an extended Boussinesq approximation with an infinite Prandtl number (i.e., no inertial term) and solves the following conservation equations,

$$-\nabla \cdot (2\eta\dot{\varepsilon}) + \nabla P = \rho \boldsymbol{g}\,, \tag{2.1}$$

$$\nabla \cdot \boldsymbol{u} = 0\,, \tag{2.2}$$

$$\begin{aligned} \bar{\rho} C_p \left(\frac{\partial T}{\partial t} + \boldsymbol{u} \cdot \nabla T\right) - \nabla \cdot k\nabla T = \bar{\rho} H \\ + (2\eta\dot{\varepsilon}) : \dot{\varepsilon} \\ + \alpha T \left(\boldsymbol{u} \cdot \nabla P\right), \end{aligned} \tag{2.3}$$

$$\frac{\partial c_i}{\partial t} + \boldsymbol{u} \cdot \nabla c_i = q_i\,, \tag{2.4}$$

where (2.1) is the conservation of momentum, with the effective viscosity η, the deviator of the strain rate tensor $\dot{\varepsilon}$ (defined as $\frac{1}{2}(\nabla \boldsymbol{u} + (\nabla \boldsymbol{u})^T)$), the velocity $\boldsymbol{u}$, the pressure P, the density ρ, and $\boldsymbol{g}$ the gravity. Equation (2.2) describes the conservation of mass. Equation (2.3) is the conservation of energy, where $\bar{\rho}$ is the reference adiabatic density, C_p the specific heat capacity, T the temperature, k the thermal conductivity, H the radiogenic heating, and α the thermal expansivity. As right-hand-side heating terms, we include radioactive heating, frictional heating, and adiabatic heating from top to bottom, respectively. Finally, we solve the advection equation (2.4) for each compositional field c_i (e.g., upper crust, sediment age, and accumulated plastic strain), with reaction rate q_i nonzero for the plastic strain and viscous strain fields.

2.2.1.1 Rheology equations

The model uses a viscoplastic rheology (Glerum et al., 2018) that includes both plastic and viscous weakening. To simulate plastic weakening, the angle of friction is weakened by 75% from an initial value of 26.56° to 6.64° (corresponding to friction coefficients of 0.5 and 0.X, respectively) as plastic strain accumulates over the interval from 0 to 1. The viscous portion of the model is an averaged composite of diffusion and dislocation creep following Karato and Wu (1993; see parameter values in Table A.1). Viscous weakening reduces the creep prefactors by 75% over an accumulated viscous strain interval of 0 to 1.

2.2.2 Landscape evolution model

FastScape changes the model surface accounting for the stream-power law (SPL) fluvial erosion, hillslope or marine diffusion, lateral advection, and vertical uplift (Braun and Willett, 2013; Yuan et al., 2019a, 2019b). These processes are described by,

$$\frac{dh}{dt} = \boldsymbol{U} - K_f A^m S^n + \frac{G}{A}\int_A \left(\boldsymbol{U} - \frac{dh}{dt}\right) dA + K_c \nabla^2 h + \boldsymbol{v}\cdot\nabla h \,, \quad for\ h \geq h_{sea} \quad (2.5)$$

$$\frac{dh}{dt} = K_m \nabla^2 h + Q_s + \boldsymbol{v}\cdot\nabla h \,, for\ h < h_{sea} \quad (2.6)$$

where h is the topographic elevation, $\boldsymbol{U}$ the uplift rate, K_f the bedrock erodibility, A the drainage area, S the slope, m the drainage area exponent, n the slope exponent, G the deposition coefficient, K_c the continental diffusion coefficient, $\mathbf{v}$ the lateral velocity, K_m the marine diffusion coefficient, and Q_s the total continental sediment flux. Equation (2.5) represents processes in the continental domain and from top to bottom including the uplift rate, SPL fluvial erosion, sediment deposition, hillslope diffusion, and lateral advection. Equation (2.6) represents marine processes. In the following, we use m = 0.4, n = 1, and G = 1 following previous studies (Yuan et al., 2019a, 2019b; Guerit et al., 2019).

2.2.3 ASPECT-FastScape coupling

The two-way coupling between ASPECT and FastScape is implemented through a back-and-forth transfer of surface velocities and surface topography (see supplement, Neuharth et al., 2021). During the first timestep, ASPECT initializes and runs FastScape using the initial model surface topography and velocities from the zeroth timestep. In 2D (X-Z) ASPECT models, velocities and topographies are duplicated along the Y-direction to provide a horizontal X-Y grid of values for FastScape. FastScape uses the ASPECT values to advect/uplift the surface and further alters the surface using equations (2.5) and (2.6). After FastScape has run, the new surface is compared to the previous surface from the start of the timestep and converted to a vertical (Z) mesh velocity updating the ASPECT surface at each nodal point,

$$\boldsymbol{V}_{\boldsymbol{z}(\boldsymbol{x},\boldsymbol{y})} = \frac{h_{f(x,y)} - h_{p(x,y)}}{dt_a}, \quad (2.7)$$

where $\boldsymbol{V}_{\boldsymbol{z}}$ is the vertical mesh velocity, h_f the nodal height of the current surface, h_p the height of the previous surface, and dt_a the ASPECT timestep.

Because FastScape represents a 2D surface in X and Y and the ASPECT model is a 2D slice in X and Z, vertical mesh velocities computed from the FastScape are averaged along Y. ASPECT then computes the internal changes of the mesh by solving the Laplace equation constrained by the surface mesh velocities (Rose et al., 2017). ASPECT subsequently responds to the topography changes during the solving of Eqs. (2.1-2.4) and the process repeats in the next timestep. However, in subsequent timesteps only the surface velocities are sent to FastScape, while FastScape retains its own copy of the surface topography. This is done to avoid resolution loss in the topography.

In 2D models, FastScape is geometrically initialized with an extent in the Y-direction that is chosen by the user (here 100 km), and an X-length that is the ASPECT length plus two additional FastScape nodes on either side. These additional nodes represent FastScape "ghost nodes" that exist outside the ASPECT model domain, and thus the values are not considered when interpolating the surface back to ASPECT. The ghost nodes are primarily used to avoid boundary artifacts in FastScape (i.e., no uplift from advected topography) from appearing in ASPECT. To avoid issues that may arise from artificial boundary slopes, the ghost nodes are updated each timestep to be identical to the nearest ASPECT boundary node.

2.2.4 Fault extraction and analysis

To perform a comprehensive fault analysis, we extract fault networks from our model results using tools from the field of computer vision (https://github.com/thilowrona/fatbox). This process describes fault systems as 2D networks (or graphs, i.e., structures consisting of nodes and edges), where faults are sets of connected nodes. The fault extraction workflow consists of five main steps: 1) Thresholding: We separate shear zones from the background of our model using a plastic strain threshold of 10% of the maximum non-initial plastic strain, or anything above 1 (fully weakened). This value assures the extraction of all major shear zones from our models. 2) Skeletonization: We collapse these shear zones to one-pixel wide lines that represent discrete faults using skeletonization (Guo and Hall, 1992). 3) Connecting components: we label adjacent pixels as connected components (Wu et al., 2009). 4) Graph building: We build our graph from these components using pixels as nodes and connections as edges. 5) Junction splitting: We split up triple junctions to identify individual fault and remove any faults less than 1.5 km in length.

Once fault networks are extracted from each timestep, we correlate them across timesteps to track their temporal evolution throughout the simulation. This correlation relates faults through time based on their geometric similarity, allowing for faults to initiate, merge, split and die.

Once correlated, we can track fault and fault system properties through time. For our analysis, we focus on the number of faults, fault lengths (sum of edges) and fault displacements. Fault displacement is computed as the cumulative sum of an individual fault's slip from all previous timesteps, and the fault slip is computed from the velocity difference between hanging wall

and footwall across the fault. Because of this, displacement held on a fault is sensitive to how long a fault is active for.

2.2.5 Model setup

To investigate fault system evolution in response to erosion and sedimentation during asymmetric, symmetric, and wide rifting, we set up a rectangular 2D tectonic ASPECT model with dimensions 450x200 km (X and Z) initialized with 4 rheologic layers (Fig. 2.1): a wet quartzite upper crust (20 km thick; Rutter and Brodie, 2004), wet anorthite lower crust (15 km thick; Rybacki et al., 2006), and dry olivine mantle lithosphere extending to the Lithosphere-Asthenosphere Boundary (LAB) that is set to a value typical of a non-orogenic or cratonic intracontinental setting (120 km; Artemieva, 2006; Pasyanos et al., 2014). Beneath the LAB, asthenospheric material is composed of wet olivine (Hirth and Kohlstedt, 2003). To initiate continental rifting in the model center, we thicken the warmer upper crust to 25 km (leading to a total crustal thickness of 40 km) and thin the mantle lithosphere so that the LAB still occurs at 120 km. In addition, we distribute randomized initial plastic strain within the model domain mimicking small-scale inheritance. In all models, the value of the compositional fields is prescribed along the top and bottom boundaries. Any increases in surface topography from FastScape due to sediment deposition and not tectonics will thus be considered as sediment accumulation.

The model initial temperature is prescribed using a steady-state geotherm from the surface to the LAB at 120 km. Below the LAB, temperature is determined by a mantle adiabat. Temperature boundary conditions fix the top boundary at 0° C, the bottom temperature is prescribed according to the initial mantle adiabat, and the left and right boundary are prescribed with a zero heat-flux.

The left and right boundaries are extended at a rate of 5 mm/yr, giving a total extension rate of 10 mm/yr, which amounts to 300 km of total extension over 30 Myr. Outflow at these boundaries is compensated by inflow along the bottom boundary (~4.4 mm/yr) to conserve volume. The top boundary is deformed using FastScape.

On timestep 1 FastScape is initialized as a 2D surface that matches the initial ASPECT surface (including initial topography) where the user-defined ASPECT Z-extent is an elevation of zero in FastScape. To simulate erosion and deposition, we utilize the marine and land components of FastScape and assume a sea-level 500 m below the initial ASPECT height. Above sea-level, we use a diffusion coefficienct of $5 \cdot 10^{-3}$ m^2/yr for bedrock and sediment (Martin, 2000; Densmore et al., 2007; Armitage et al., 2013). Since the bedrock erodibility represents multiple factors such as precipitation, lithology, and vegetation (Whipple and Tucker, 1999) and can vary over multiple orders of magnitude in nature (10^{-7} to 10^{-2} $m^{0.2}/yr$; Stock and Montgomery, 1999), we vary K_f between 10^{-6} and 10^{-4} $m^{0.2}/yr$ to represent low to high surface process efficiency (Wolf et al., 2021). Below sea-level, we use a diffusion coefficient consistent with marine settings (200 m^2/yr; Rouby et al., 2013). Additionally, in the marine environment we assume there is some pelagic/hemipelagic sedimentation and add a uniform time-dependent topography increase to regions below sea-level accordingly (Table A.2).

The model mesh resolution ranges from a minimum 10 km to a maximum of 156 m in the sediment composition. Areas without sediment can reach a maximum resolution of 312 m,

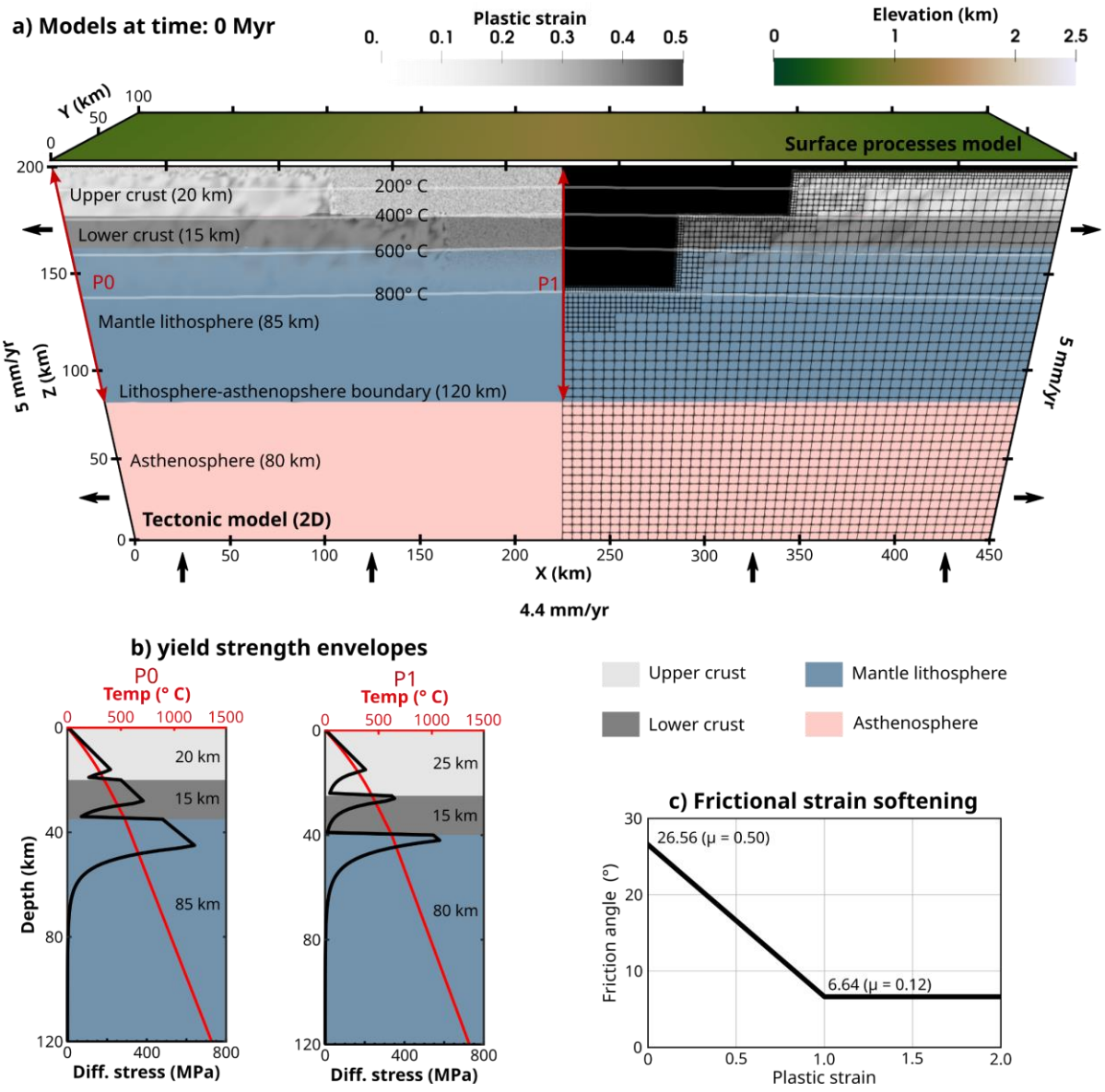

Figure 2.1 Reference asymmetric rift model setup at 0 Myr. a) Topography of the surface process model (FastScape) is shown on top colored by elevation. Below is the 2D tectonic model ASPECT colored by material layers. White lines indicate temperature contours. Red lines show strength profile locations for the outer (P0) and central (P1) portions of the models that have different layer thicknesses. Right side shows the model mesh refinement. b) Yield strength profiles P0 and P1 indicated in A, showing the integrated strength (black) and temperature (red). c) Graph showing the plastic weakening interval.

which occurs in any cell that contains particles. Passive particles are initially uniformly distributed within a 100 km wide box in the upper 55 km of the model around the center (Gassmöller et al., 2018). The mesh is updated every 5 timesteps, and as the particles are advected with the material velocity the faulted areas remain highly refined. The FastScape mesh has a uniform resolution of 312 m.

Our models provide a detailed look at fault and landscape evolution in 2D rift systems, however, multiple limitations exist. While extensional slip along our faults accounts for most of the expected extension in the model (according to the fault analysis results; Fig. A.1), we do not include faults smaller than 1.5 km in the analysis and thus neglect smaller fault dynamics, especially in late breakup stages where the brittle envelope may be thinner than 1.5 km. Additionally, since our tectonic model is 2D, we do not consider how fault system evolution is

impacted along-strike by variability in loading related to erosion, deposition and inheritance (e.g., Heron et al., 2019; Naliboff et al., 2020). Also, we assume our models represent passive margins without magmatic activity, as such we do not account for the inclusion of melt possibly altering rift dynamics (e.g., Bahadori and Holt, 2019).

2.3 Results

We present the general and fault system evolution of three different model setups that result in endmembers for rifted margin formation: narrow rifting leading to (1) asymmetric and (2) symmetric margin configurations and (3) rifting where deformation occurs over a wide region resulting in a large zone of thinned continental crust. Our reference model of an asymmetric narrow rift has been described in the previous section. To achieve a symmetric narrow rift, we reduce the frictional angle weakening from the 75% used in the reference model to 50% (Huismans and Beaumont, 2003). Wide rifts generally occur in regions with thick crust and high heat flow (Buck et al., 1999), as such we again use a frictional angle weakening of 50% and increase the radiogenic heating of the upper crust from $1.0 \cdot 10^{-5}$ to $1.5 \cdot 10^{-5}$ W/m^3 and change the crustal thicknesses to 35 km upper crust and 5 km lower crust in the middle of the model domain, and to 25 km of upper crust and 10 km lower crust elsewhere. All other parameters remain identical between the three model sets.

2.3.1 Asymmetric rift systems

In this section we discuss the reference asymmetric model (bedrock erodibility, $K_f = 10^{-5}$ $m^{0.2}$/yr) and compare it to additional models where we have no Surface Processes (SP) or vary the K_f value.

We find from a quantitative analysis of the evolution of the number and cumulative length and displacement of active faults in the system, that regardless of the SP efficiency the system can be divided into five distinct phases: 1) *distributed deformation and coalescence*, 2) *fault system growth*, 3) *fault system decline and basinward localization*, 4) *rift migration*, and 5) *continental breakup*.

2.3.1.1 Asymmetric reference model evolution

Initially, many small faults accumulate small amounts of strain within the model center. By 0.4 Myr (Fig 2.2a; Video A.1), these faults have coalesced into two major normal faults that connect at ~45 km depth in the mantle lithosphere (Huismans and Beaumont, 2003; Albaric et al., 2009). These major faults accumulate displacement, forming rift flanks as the central block sinks. This sinking causes the major faults to define the land and sea boundary, and the region between them becomes a sediment trap. As the uplifted rift flanks erode, a seaward thinning

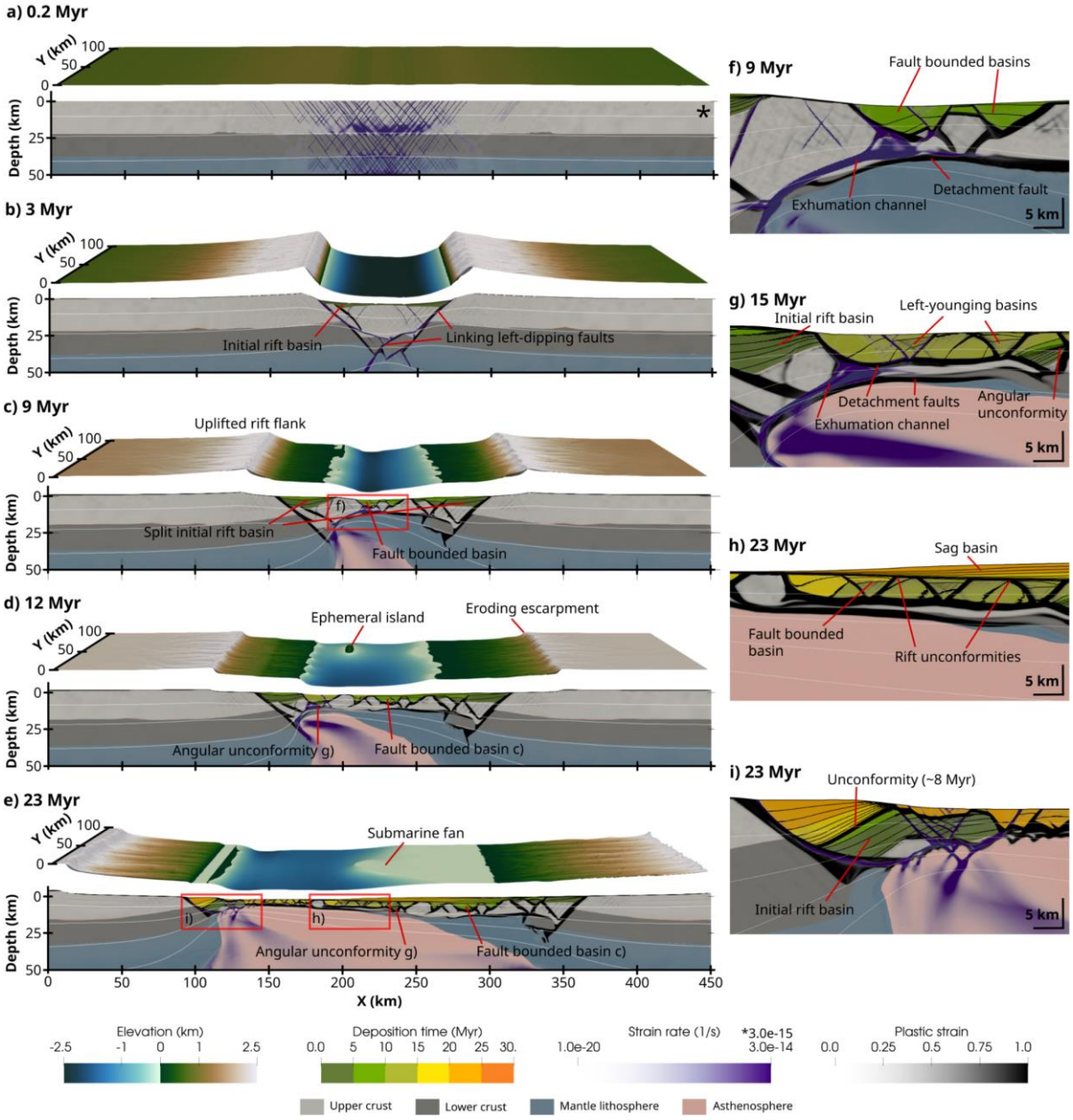

Figure 2.2 Evolution of the reference asymmetric rift model (Videos A.1 and A.2) depicting the formation of surface faults within a thinning brittle layer, and underlying detachment faults related to an exhumation channel. (a-e) The FastScape model (3x vertical exaggeration) is shown on top. The ASPECT model is shown on the bottom showing the strain rate (transparent to purple), plastic strain (transparent to black), isotherms, and sediment deposition time (shown in 5 Myr intervals). White contours indicate temperature between 200 and 800 C. *Strain rate scale is reduced in A to highlight distributed deformation. (f-i) Close up views to highlight specific basin and fault features, with black contours indicating sediment age at 1 Myr intervals.

basin forms between the border faults (Pérez-Gussinyé et al., 2020). At ~3 Myr, the left-dipping border fault links to the viscously deforming mantle lithosphere through a secondary left-dipping fault in the lower crust of the central block. The linkage of these faults generates a concave downward left-dipping detachment fault (Fig. 2.2b; Lavier and Manatschal, 2006). Necking uplifts and rotates the detachment fault to lower angles and provides a weak base for new faults to form and dismember the central block (Huismans and Beaumont, 2003). Subsequently, the initial basin is split and separated by exposed upper crust (Fig. 2.2c). By ~7 Myr, the two major border faults become inactive as the detachment fault connects to the younger, smaller faults forming in the center of the model, creating an asymmetric rift.

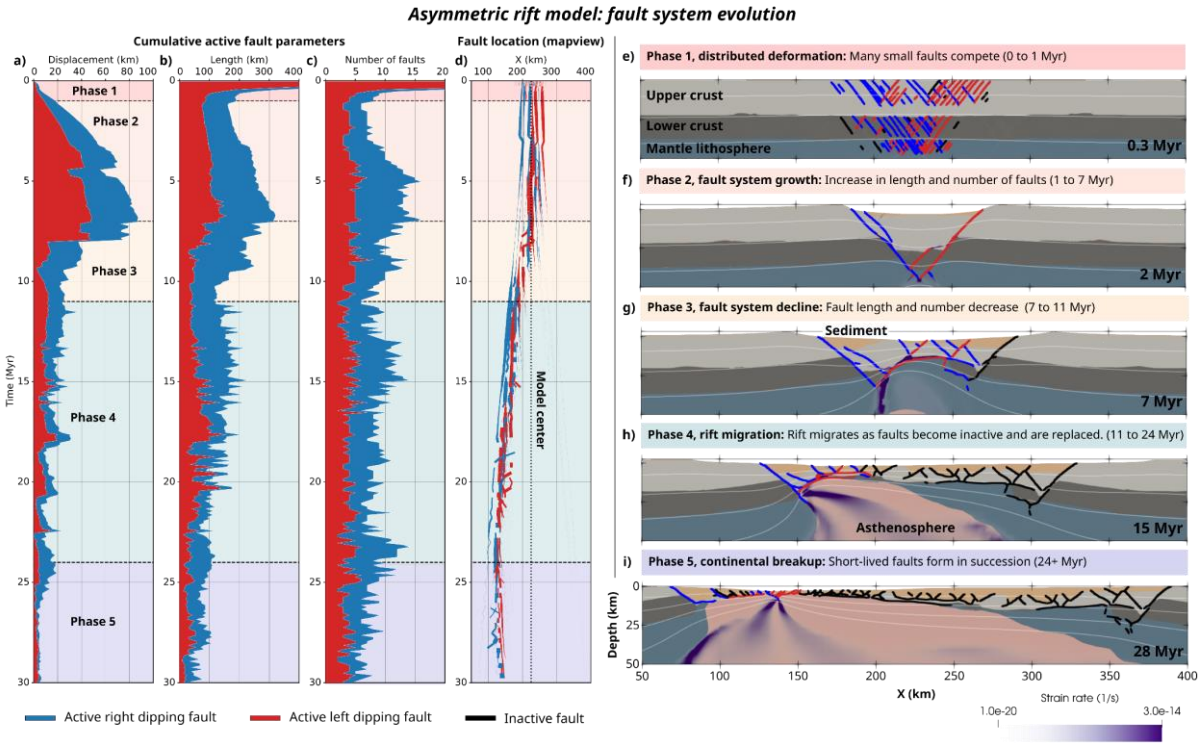

Figure 2.3 Active fault network evolution of the asymmetric rift reference model showing the five fault system deformation phases that relate to structural domains. (a-d) Graphs depict the change in cumulative active fault properties and fault location through time. Blue indicates right dipping faults and red left dipping faults. The background is colored by the deformation phases. (e-i) Snapshots of the ASPECT model during different phases. The extracted fault network is overlain on the model in black (inactive fault), blue (active right dipping fault), and red (active left dipping fault).

At ~7 Myr, the rift system migrates to the left (Brune et al., 2014). Large faults that connect from the surface to the detachment fault dissect and rotate the crust to the right of the rift, creating additional basins between the blocks (Fig. 2.2f). At ~11 Myr, there is a rightward shift in the rift as the initial detachment fault becomes inactive, and a second detachment fault forms and connects to the initial left border fault that resumes activity. To the right of the rift, the crust is thin by 12 Myr (~4 km) and faulting primarily occurs within the sedimentary infill (Fig. 2.2c). As the rift migrates, conjugate faults form in succession, with fault-bounded left-younging basins being deposited adjacent to the left half of the initial rift basin (Fig. 2.2g). Around this time, rotation of an upper crustal block leads to emergence of basement above sea-level creating an ephemeral island (Chenin et al., 2019). As migration continues, the older inactive fault-bounded basins are overlain by sediment marking multiple rift migration unconformities (Fig. 2.2h; Pérez-Gussinyé et al., 2020). Eventually, slip on the initial left border fault that bounded the initial rift basin increases, tilting the sedimentary layers and causes deposition of new sediment on top of the old rift basin (Fig 2.2i). Because of this tilting, the oldest sediment is exposed near the migrating rift, and parts of the initial rift basin are translated to the right side of the rift. At ~23 Myr, there is an ~10 km rightward shift in deformation as migration ceases and seafloor spreading begins (Fig. 2.2d), this shift in deformation causes fault-block emersion of the marine shelf. Subsequently, there is a short phase of stability (~23-25 Myr) before asymmetric sea floor spreading initiates and migrates to the right.

2.3.1.2 Asymmetric fault system evolution

We use our fault extraction toolbox (Fatbox) to examine the quantitative evolution of the rift's fault network in terms of the number, cumulative length, and displacement held on active faults in the system. Using the plastic strain, we can track the entire fault system, however of particular interest are the active faults. To this end, we consider any fault with a maximum slip rate >0.1 mm/yr as active, a value on the lower end of fault slips seen in the Great Basin (0.06 to 3 mm/yr; Depolo and Anderson, 2000). If the slip along an individual fault falls below this value, it no longer contributes to the cumulative total in length and displacement. Using this value, the active faults account for 97.8% of the total slip held on the tracked faults (Fig. A.2), illustrating the robustness of our approach.

The active faults in the system suggest that the model evolves according to five separate phases (Fig. 2.3, Video A.2):

Phase 1: Distributed deformation and coalescence (~0-1 Myr). During this phase many small faults form and compete. The phase has a large total fault system length and number of faults that quickly declines as deformation localizes on a few major faults.

Phase 2: Fault system growth (~1-7 Myr). The faults formed during phase 1 coalesce into two major border faults, marked by a reduction in the fault number and length. As extension continues, new, smaller faults form between the initial ones leading to a growth in the number, length, and displacement of the active faults. Over time slip on the inner faults increases relative to that on the border faults, until eventually the border faults become largely inactive as deformation localizes basinward.

Phase 3: Fault system decline and basinward localization (~7-11 Myr). We distinguish the start of phase 3 by one of the border faults becoming inactive. As the outer faults, particularly those opposite the direction of rift migration, become inactive, the fault system shows a decrease in the number, length, and displacement held on the active faults. Since the brittle layer thins, new faults are shorter than previous ones. Also, because older faults become inactive at this time there is a net loss in the total displacement held on the active faults.

Phase 4: Rift migration (~11-24 Myr). During rift migration, faults are shorter lived compared to the previous phases, with new faults frequently forming and replacing older faults (~1-2 Myr activity time). This shorter activity time leads to less displacement on active faults relative to phases 2 and 3. While there is some variation in the fault number and length of the system, generally this phase shows a gradual decline in, most notably, the cumulative length of the system as the brittle layer the faults form in continues to thin before breakup.

Phase 5: Continental breakup (~24 Myr to model end). We determine the breakup phase to have started when the rift jumps seaward and completes the separation of continental lithosphere. While the number of faults remains similar to phase 4, the cumulative length of the system continues to decrease as the sediment layer thins, and there is a noticeable drop in the displacement. The drop in displacement likely relates to the lifespan of faults, when faults are replaced more quickly there is less time to accumulate displacement before they become inactive.

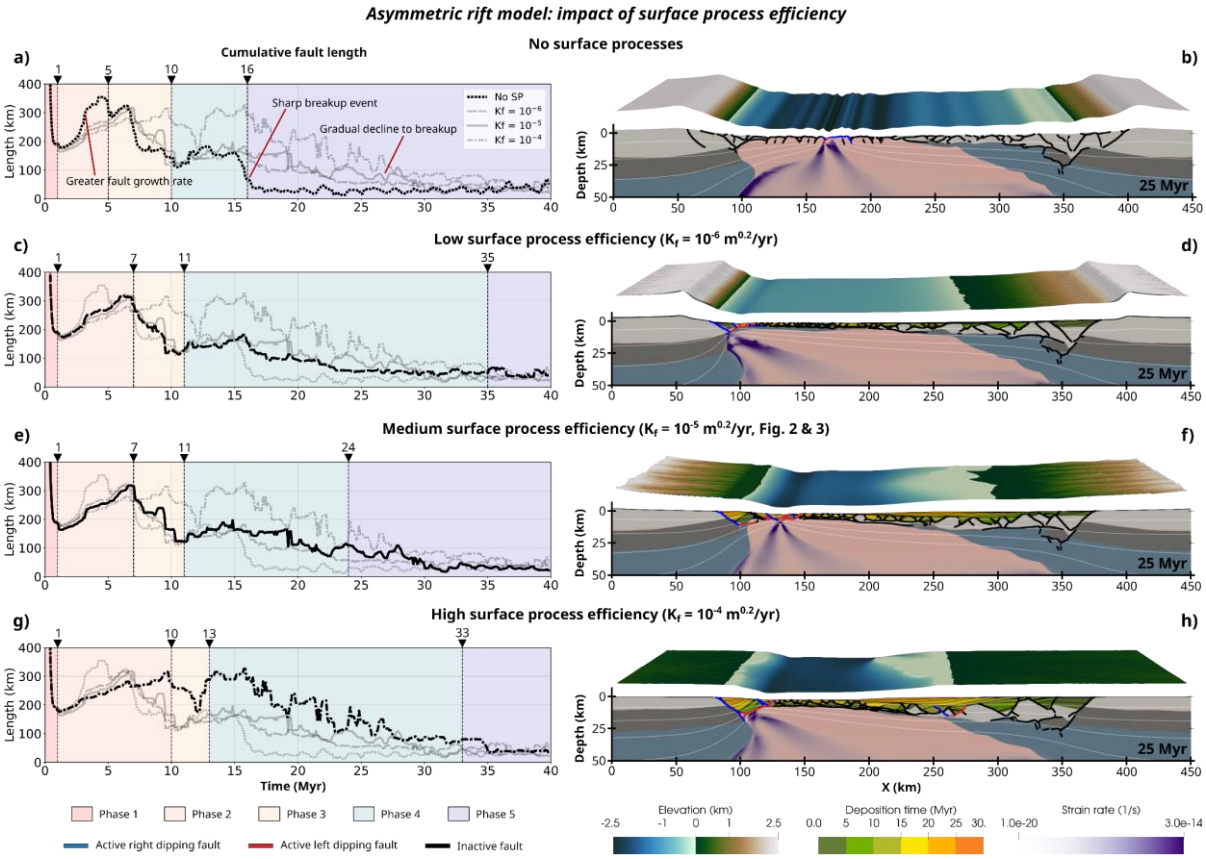

Figure 2.4 Comparison of the active fault network's cumulative length between asymmetric rift models with varying surface process efficiency, displaying the greater periods of fault system growth and rift migration with surface processes. a) Fault length graph for the model without surface processes, where the background is colored by the phase. The dark black line represents the current no surface processes model while the semi-transparent lines indicate the other models. b) Snapshot of the model without surface processes at 25 Myr. The extracted fault network is overlain on the model in black (inactive fault), blue (active right dipping fault), and red (active left dipping fault). Low (c-d), medium (e-f), and high (g-h) surface process efficiency models.

2.3.1.3 Effects of surface process efficiency on Asymmetric rift systems

To discuss how SP efficiency affects the phases of fault system evolution (Fig. 2.4), we focus on the cumulative fault length as it best distinguishes the phases. Phase 1 is similar regardless of SP and the value of bedrock erodibility. In phase 2, faults grow slower with greater SP efficiency, and the shift into fault decline (phase 3) is delayed. Phase 3 is similar in all the models, though more faults are active at a given time in the model with high SP efficiency, making it harder to distinguish the shift from phase 3 to 4 (Fig. 2.4g). Breakup (phase 5) is clearly visible in the model without SP, wherein the length of the active fault system sharply decreases at breakup (Fig. 2.4a). In models with SP, the cumulative length gradually declines during migration as the sediment layer thins leading to a less noticeable breakup event. Additionally, the sediment layer delays breakup, although the amount of sediment does not appear to influence how much breakup is delayed (i.e., breakup occurs at 16 Myr with no SP, 35 Myr with low SP efficiency, 24 Myr with medium efficiency, and 33 Myr with high efficiency; Table S3).

2.3.2 Symmetric rift system

In the same manner as the previous section, here we cover the evolution of a symmetric narrow rift. We find that the symmetric setup evolves according to 4 distinct phases similar to what is seen in the previous model, but without rift migration (phase 4).

2.3.2.1 Symmetric reference model evolution

The model starts with many faults accumulating small amounts of strain (Video A.3), which by ~1 Myr have coalesced onto two major ~50° dipping conjugate faults (Huismans and Beaumont, 2003). These major faults define the land-sea boundary, and the region between is filled with sediment forming an oceanward thinning rift basin by ~4 Myr. During the necking process, rotation of the initial major faults generates many parallel-seaward-dipping faults that breakup the central block (Nagel and Buck, 2004). This breakup results in a relatively symmetric splitting of the initial rift basin, with new faults forming between the basins and a similar inward shift of the land-sea boundary. By ~8.5 Myr, the deeper portions of the initial major faults have rotated to ~35° and become inactive. Necking continues as the remainder of the central block is broken up. New basins form in the model center as the rift flanks and the, now exposed, initial rift basin halves are eroded and deposited. At ~14 Myr seafloor spreading starts.

Initially, the nearby uplifted margins provide a large sediment flux and seafloor spreading is sediment-dominated. Primarily, seaward dipping faults form successively within the sediment creating multiple fault-bounded basins. Simultaneously, short migration events generate landward dipping faults that extend from the sediment basement into the asthenosphere, though the cumulative asymmetry of these events produces an overall symmetric system (Huismans and Beaumont, 2003). As the uplifted margins move further from the active rift zone, less sediment reaches the model center and progressively smaller faults form within the thinning sediment layer. Near the margins, sediment is deposited on top of the inactive faults marking multiple rift unconformities with the fault-bounded basins. By ~25 Myr very little sediment reaches the model center and basin formation halts as seafloor spreading becomes sediment-starved.

2.3.2.2 Symmetric fault system evolution

Using the same phase definitions as described in Section 3.1.2, we find that the fault system in the symmetric rift model evolves according to 4 phases (Fig. 2.5, video A.4).

Phase 1: Distributed deformation and coalescence (~0-1.5 Myr). Many faults compete before coalescing. In the fault system, this appears as a high number of faults and cumulative fault length that rapidly declines.

Phase 2: Fault system growth (~1-8 Myr). The major border faults remain active while new faults form and dismember the central block. This is seen as a period of increase in fault system length, number, and displacement.

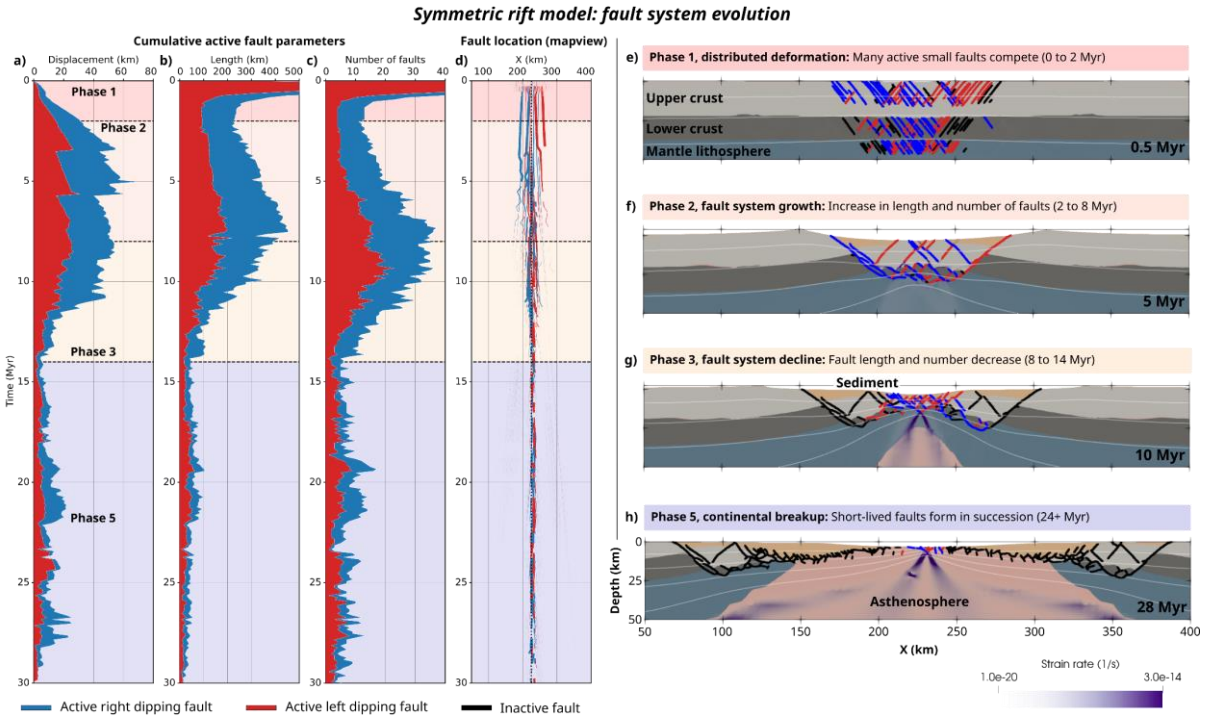

Figure 2.5 Active fault network evolution of the symmetric rift reference model, showcasing the basinward migration of deformation through the phases. Refer to figure 2.3 for explanation.

Phase 3: Fault system decline and basinward localization (~8-14 Myr). By 8 Myr, the border faults become inactive as deformation localizes in the central region. This leads to a decrease in the number of faults and the cumulative length of the system.

Phase 4: Rift migration. This phase is not expressed in this setting.

Phase 5: Continental breakup (~24 Myr to model end). In this phase, short faults form in succession in the thin sediment layer. Because faults are smaller and shorter-lived in this phase, the fault system shows a lower number of faults, fault length, and displacement compared to the previous phases.

2.3.2.3 Effects of surface process efficiency on Symmetric rift systems

Similar to section 3.1.3, we run four models with varying SP efficiency (Fig. 2.6). Phase 1 is consistent regardless of SP. Phase 2 lasts longer with increasing SP efficiency (~2 Myr difference with no SP vs. high efficiency). Additionally, less effective SP leads to more faults and a greater cumulative length. SP does not generally affect phase 3, with the exception of the high efficiency case where it lasts significantly longer. In all other models, phase 5 (breakup) is delayed proportional to SP efficiency. In the high SP efficiency case, there is a gradual decline in the fault system length and continental breakup is not clearly distinguishable in this variable.

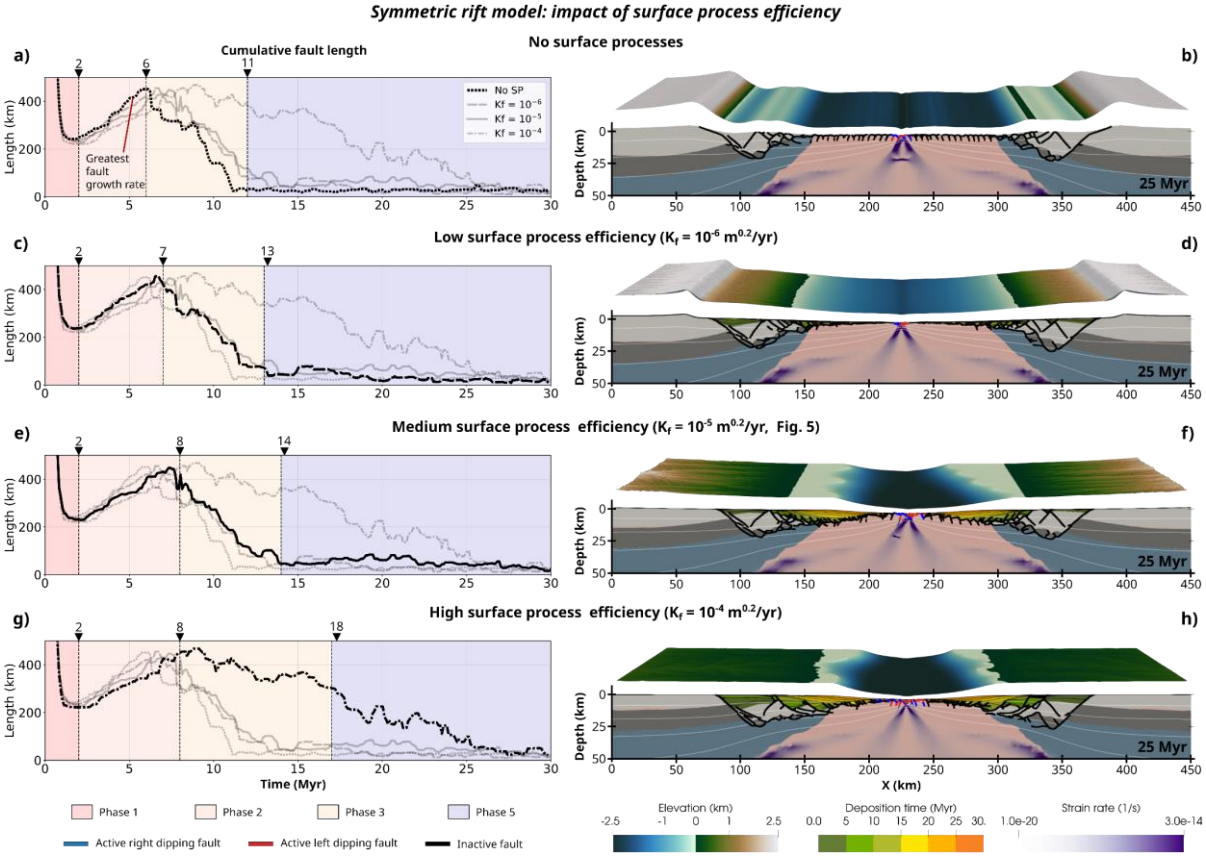

Figure 2.6 Comparison of the active fault network's cumulative length between symmetric rift models with varying surface process efficiency, depicting the delay in breakup with greater surface process efficiency. Refer to figure 2.4 for explanation.

2.3.3 Wide rift system

Here we examine the evolution of a wide rift model with varied SP efficiency and find that the fault system evolves in four phases similar to the narrow symmetric model, although the timing of phases differs.

2.3.3.1 Wide reference model evolution

During the distributed deformation phase, many faults form within the brittle portion of the upper crust (Video A.5). By ~1 Myr, these have localized on two sets of conjugate faults and one right-dipping fault ~50 km left of the model center. As the faults accumulate displacement, each becomes associated with a basin and a shallow sea or lake. During the necking process fault rotation to lower angles widens basins and faults form over a wider region. Generally, new faults dip towards the rift center forming half-graben basins (Leeder and Gawthorpe, 1987) whose strata dip away from the rift center. By 12 Myr, multiple faults have formed over a region spanning ~260 km and the multiple seas associated with each fault have merged into a single sea. At this time many small basins exist and are separated by exposed upper crustal blocks. While the outer basins dip away from the rift center, near the rift center tilting is more varied. Progressively smaller faults and basins form as necking continues and the remaining upper crust is thinned. By ~25 Myr, deformation has localized in the center where the upper crust is entirely gone, and sediment-dominated continental breakup occurs. At this time the

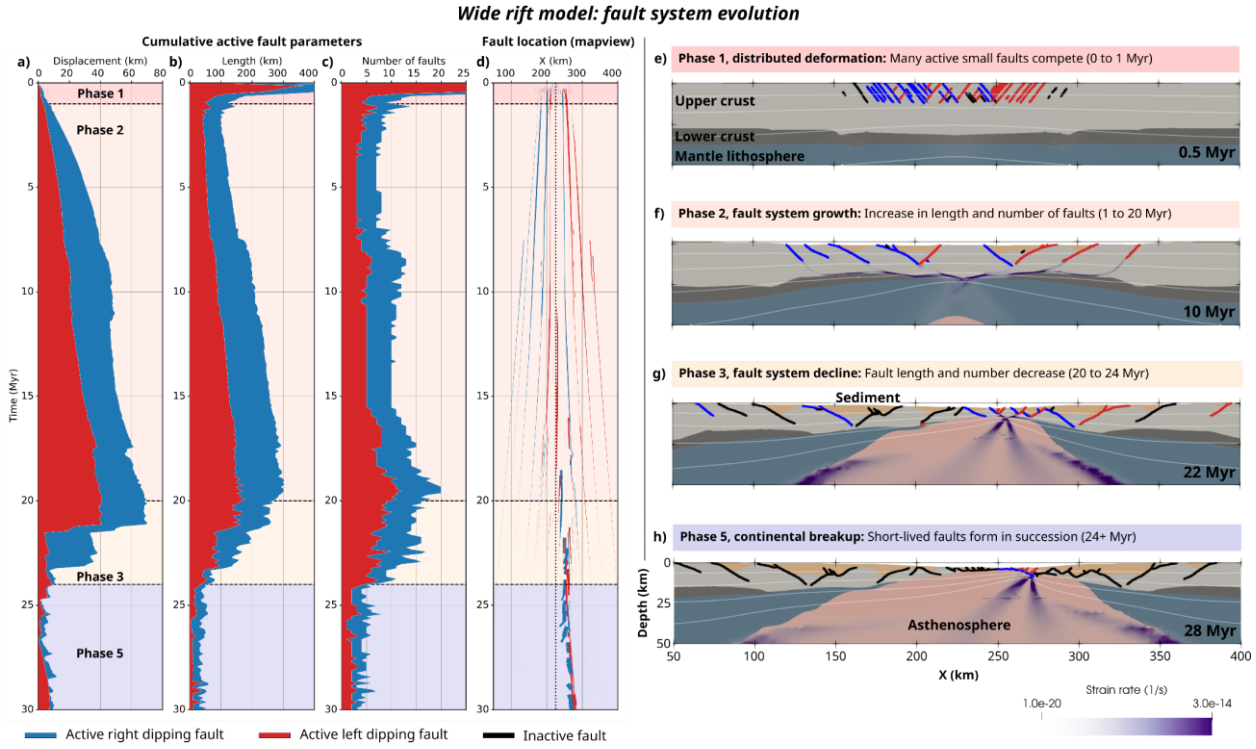

Figure 2.7 Active fault network evolution of the wide rift reference model, showcasing the greatly extended fault growth phase relative to asymmetric and symmetric models. Refer to figure 2.3 for explanation.

previously-active distal faults have been overlain with sediment marking multiple rift unconformities. From here until the end of the model the rift migrates to the right driven by the thin layer of sediment overlying the rift.

2.3.3.2 Wide fault system evolution

We evaluate the evolution of the fault system in the wide rift (Fig. 2.7, video A.6) using the previously defined phases:

Phase 1: Distributed deformation and coalescence (~0-1.5 Myr) where many faults compete and coalesce.

Phase 2: Fault system growth (~1.5-20 Myr). New faults form while the initial ones remain active. As faults form at a slower rate and are active much longer in this model than in the asymmetric or symmetric cases, this phase is greatly extended.

Phase 3: Fault system decline and basinward localization (~20-24 Myr). When only upper crust remains in the rift center deformation localizes in the region. This shift in deformation deactivates the long-lived faults leading to a drop in fault number, length, and displacement. Unlike the previous cases, fault cessation does not necessarily start with the outer faults and move inward.

Phase 4: Rift migration. This phase is not expressed in this setting.

Phase 5: Continental breakup (~24 Myr to model end). By ~24 Myr, the upper crust is separated, denoting continental breakup. In this phase, short seaward dipping faults form

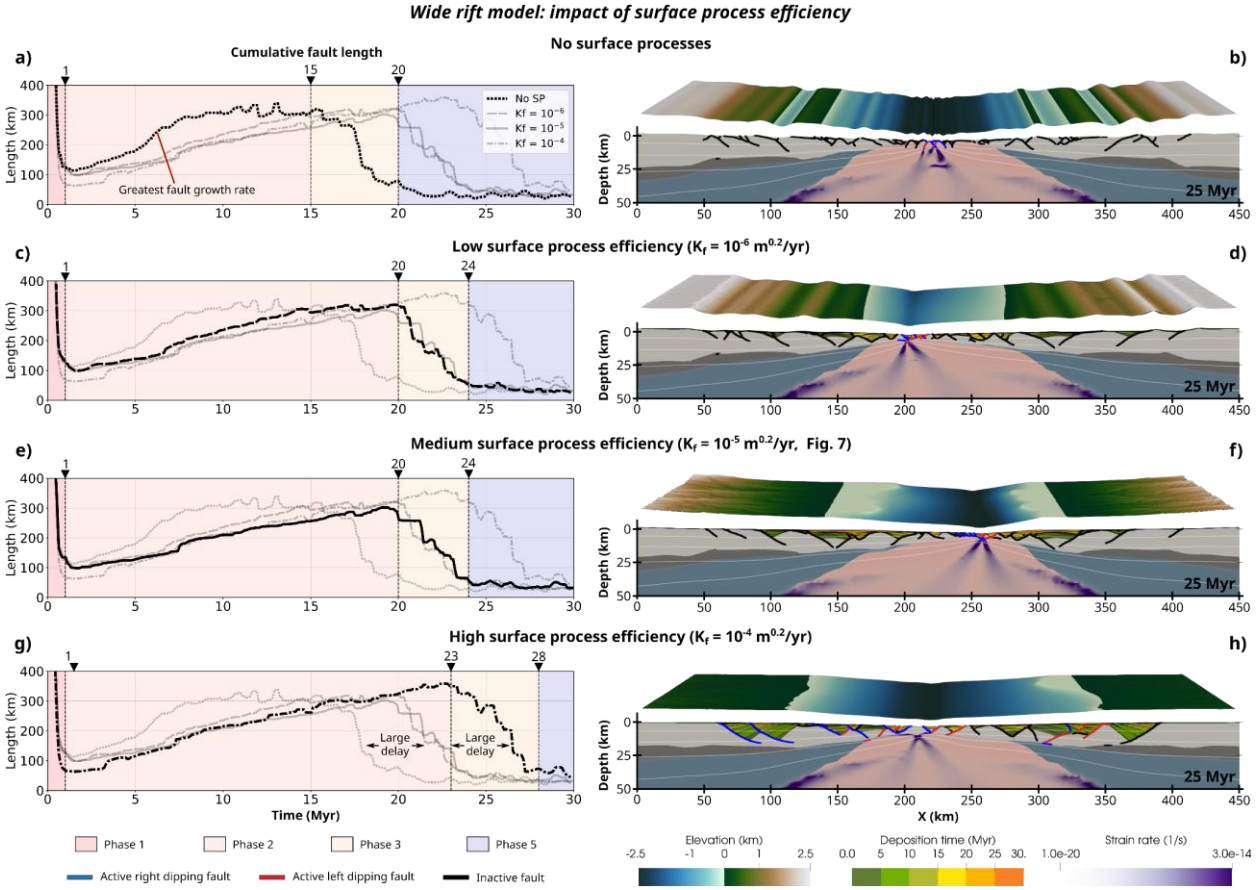

Figure 2.8 Comparison of the active fault network's cumulative length between wide rift models with varying surface process efficiency, demonstrating the greater fault growth rate and fault structure complexity in models without surface processes. Refer to figure 2.4 for explanation.

sequentially while the rift migrates. This phase shows much lower fault number, length, and displacement than phases 1-3, and the properties remain relatively constant.

2.3.3.3 Effects of surface process efficiency on Wide rift systems

By varying the efficiency of SP, we find that phase 1 is similar in all cases, except that there is a trend that higher efficiency leads to localization on a fewer number of faults (Figs. A.3 and A.4) and, thus, to a lower cumulative length of faults (Fig. 2.8). Like previous asymmetric and symmetric cases, SP extend the fault growth (phase 2) phase. While the initial inclusion of SP causes a large delay in the start of phase 3 (15 Myr without SP vs. 20 Myr with low SP efficiency), the difference between low and medium SP efficiency is negligible. However, high SP efficiency shows another large delay to the start of phase 3 (20 Myr at medium SP efficiency vs. 23 Myr at high efficiency). Additionally, in phase 2 cumulative length in the model without SP increases at a greater rate than those with SP until ~300 km. Subsequently both fault number and length remain relatively constant until phase 3. Interestingly, phase 3 in the low and medium SP efficiency models also starts when the cumulative length reaches ~300 km, although in the high efficiency model phase 3 is delayed until the system is ~350 km in length. Phase 3 is similar regardless of SP, with all models declining in cumulative fault length over ~3-5 Myr until continental breakup (phase 5). Unlike the asymmetric and symmetric cases, breakup is clearly represented in fault system length, regardless of SP efficiency.

2.4 Discussion

2.4.1 Effects of surface process efficiency on rifting

While each of the three rift types exhibits different fault structures and phase timings, surface processes (SP) had a similar effect on the models regardless of the rift type. In particular we find that SP efficiency affects the longevity of individual faults, the structure of fault systems, and the timing of rift phases. This agrees with previous studies indicating that faults localize faster and remain active for longer when sediments load the hanging wall and erosion releases the footwall (Maniatis et al., 2009; Andrés-Martínez et al., 2019; Theunissen and Huismans, 2019). As a consequence of prolonged fault activity, there is less incentive to create new faults as a greater portion of the prescribed system slip is held on the older faults. This explains why for less effective SP, a greater number of faults form during phase 2 (fault system growth) and phase 3 (fault system decline and basinward localization). This can be seen when comparing the cumulative length of active faults, where during phase 2 the cumulative length increases faster in models with less SP efficiency (e.g., Fig 2.4). The greater rate of increase in cumulative length during the early phases results in more shorter faults during the early phases for rifts with less SP efficiency (Figs. A.3, A.4, A.5, A.6) and predicts that in sediment-starved margins the architecture during early rifting is more complex with a greater number of interconnected faults.

While the general structural evolution of rifting in terms of symmetry and rift width is largely independent of erosion and sedimentation, our results show that individual rift phases are prolonged when surface processes are accounted for (cf. Buiter et al., 2008; Choi et al., 2013; Olive et al., 2014). Specifically, fault system growth (phase 2) lasts 1 to 8 Myr longer depending on the rift type and amount of erosion and sedimentation, whereas rift migration (phase 4) lasts 6 to 20 Myr longer with the addition of surface processes (Fig. 2.4). Hence, rifted margins with thick syn-rift sediment sequences require a larger amount of extension to achieve continental breakup (Clerc et al., 2018) and are more prone to the occurrence of rift migration (Buiter, 2021). This also suggests that along-strike changes in sediment supply could lead to neighboring portions of a rift system evolving at different paces, with sediment-starved rift segments reaching breakup and ocean formation sooner than sediment-rich segments.

2.4.2 Rift migration, detachment faults and serpentinization

In our models rift migration is facilitated through a combination of an exhumation channel (Brune et al., 2014) and slip along detachment faults (Fig. 2.9). Material in the exhumation channel zone undergoes large amounts of brittle and ductile deformation. At the base of the zone, a tongue of plastically yielding lower crust generates a concave downward detachment fault. Continued extension rotates the fault and adjacent ductile shear zone to sub-horizontal angles, creating a weakened channel of material. The geometry, location and kinematic history of this channel reproduces the characteristics of the prominent "S reflector" at the West Iberian margin (Hoffmann and Reston, 1992; Reston et al., 2007). A secondary concave upward detachment fault forms at the surface and connects to the concave downward fault in the weakened channel. Rooted in the second detachment fault along the weakened channel, a zone of high plastic strain generates sequential conjugate or seaward dipping normal faults.

Our models suggest that detachment faults form near a frictionally and viscously weakened exhumation channel and are rotated subhorizontally. Slip along these detachment faults is greater in the portions at higher angles, but low-angle slip occurs as the rotated exhumation channel translates material from the left to right margin. Normal faults form in a migrating fault generation zone that is rooted in a detachment fault. These normal faults are not exclusively active sequentially and often multiple faults are active simultaneously. Slip is greatest on newly formed faults and decreases with age and distance from the fault generation zone (e.g., Fig. 2.9d).

Low-angle slip in our models occurs along the rotated exhumation channel consisting of frictionally and viscously deformed material. It has been suggested that such low-angle slip requires weak hydrated rock such as serpentinite (Lymer et al., 2019). The upper temperature limit for serpentinization is not well constrained and falls between ~350-600 °C (Lavier and Manatschal, 2006; Emmanuel and Berkowitz, 2006; Pérez-Gussinyé et al., 2006; Bickert et al., 2020; Albers et al., 2021). While our models do not include the process of serpentinization, temperatures found near the detachment faults enable the generation of serpentinite in the region (Fig. 2.9b). This is in contrast to previous models (Brune et al., 2014, 2017) that did not have the required numerical resolution to resolve the thin mantle layer of sufficiently low temperatures. The addition of serpentinization could result in greater slip along the detachment fault, possibly increasing surface fault activity. It has also been suggested that serpentinization requires a thin, entirely brittle, crust (<10 km; Reston and Pérez-Gussinyé, 2007). We find that sedimentation increases the depth, temperatures, and the degree of viscous deformation within the rotated exhumation channel rendering it less prone to achieve serpentinization (Fig. 2.9cd). These factors suggest that serpentinization is more likely to occur in sediment-starved margins

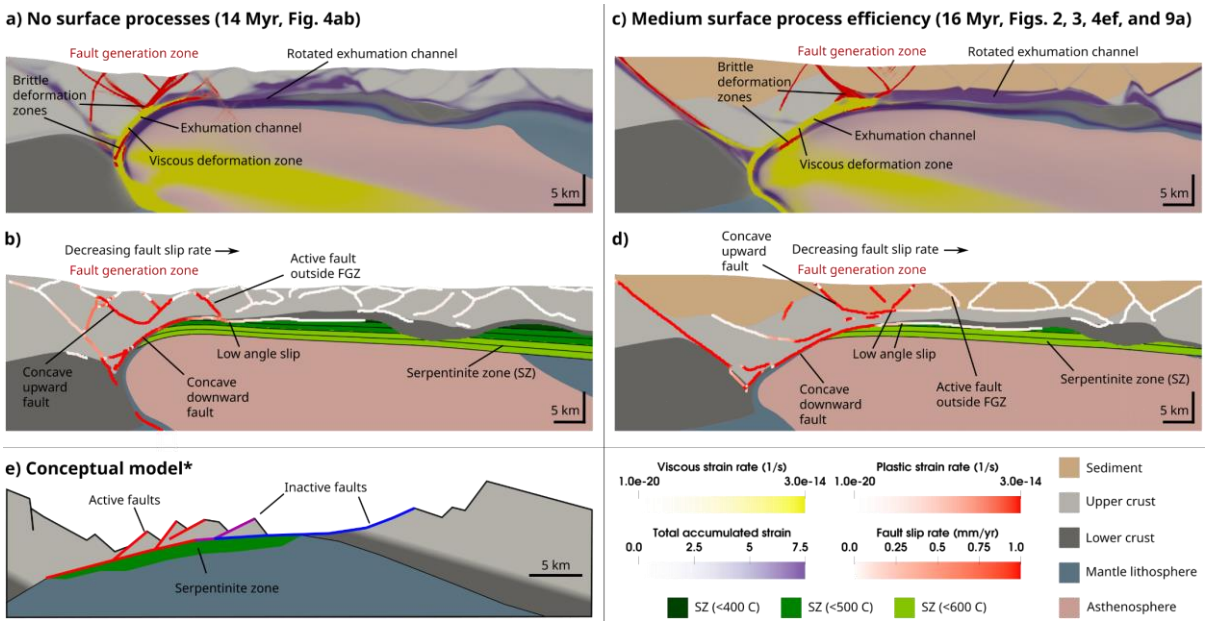

Figure 2.9 Rift migration processes, showing the brittle and viscous deformation inside the exhumation channel, and low angle slip along detachment faults relative to regions where serpentinization would be possible. a) Snapshots of the no surface processes model that showing the plastic strain rate (opaque-red), viscous strain rate (opaque-yellow), and total accumulated strain (opaque-purple). b) Identical to a) showing the fault slip rate (white-red) along the extracted fault network. Regions within temperature conditions for serpentinization are colored at 100° C intervals, with black contours denoting 50° C intervals. c) Snapshots of the medium surface process efficiency reference model like in a). d) Snapshots of the medium surface process efficiency reference model like in b). e) Modified conceptual model from Lymer et al., 2019, showing the region of serpentinization. Red indicates active faults, and purple and blue inactive faults.

like the Iberian-Newfoundland margins (Whitmarsh et al., 2001; Bayrakci et al., 2016), and in the late stages of rift migration.

2.4.3 Rift phases and rifted margin domains

At continental rifts, crust and mantle lithosphere are successively thinned until breakup is achieved. This progressive thinning constitutes an intrinsically transient behavior of rifts, that does not occur for other plate boundary types (subduction zones, mid-oceanic ridges and strike-slip faults). This transientness is the underlying reason why rift evolution can be adequately described through distinct deformation phases (Lavier and Manatschal, 2006; Corti, 2012; Peron-Pinvidic et al., 2013; Huismans and Beaumont, 2014; Brune et al., 2017; Naliboff et al., 2017). Previous phase definitions have been based on changes in layer thickness (Lavier and Manatschal, 2006; Huismans and Beaumont, 2014; Naliboff et al., 2017) and their impact on rheology (Lavier and Manatschal, 2006; Huismans and Beaumont, 2014), or the location of faults (Corti, 2012). Here, we used a novel analysis technique to characterize rift phases in terms of active fault network properties like displacement, total fault length and fault number. In this section, we first compare the rift phases we identified in this study to previous definitions before we focus on their relevance for rifted margin domains.

Phase 1 (Distributed deformation and coalescence): Phase 1 is analogous to the early "stretching phase" (Peron-Pinvidic et al., 2013; Naliboff et al., 2017; Chenin et al., 2021). The Trondelag platform in Norway provides a remnant example of this phase (Peron-Pinvidic et al., 2013).

Phase 2 (Fault system growth): Phase 2 can be associated with the "thinning phase" (Lavier and Manatschal, 2006). It is also similar to the first phase in two-phase rifting (Agostini et al., 2009; Corti, 2012), where large faults border a central graben. Many rift segments in East Africa such as the Malawi and the Central Kenya rifts constitute examples of this phase, with active border faults surrounding the central graben (Ebinger and Scholz, 2012; Williams et al., 2019; Richter et al., 2021).

Phase 3 (Fault system decline and basinward localization): Fault system decline relates to onset of the "hyperextension phase" (Peron-Pinvidic et al., 2013) and the second phase in two-phase rifting (Agostini et al., 2009; Corti, 2012). The timing of the shift from phase 2 to 3 can vary significantly depending on the rift obliquity (Agostini et al., 2009), or as we suggest in this study, rift type (e.g., wide, symmetric, asymmetric) and the efficiency of surface processes. An active example is the northern Main Ethiopian Rift, where fault activity is localizing basinward on the Wonji fault belt (Corti, 2012).

Phase 4 (Rift migration): Rift migration is part of the "hyperextension phase" (Peron-Pinvidic et al., 2013). Through continuous activity of a migrating exhumation channel (Brune et al., 2014), it generates distinct margin asymmetry (e.g., Iberian-Newfoundland conjugates or Central South Atlantic margins, Brune et al., 2017).

Phase 5 (Breakup): Phase 5 describes continental breakup and the onset of seafloor spreading. Being the end state of continental rifting, many natural examples exist around the globe (e.g., South Atlantic, Heine et al., 2013; Red Sea, Stern and Johnson, 2019).

The five phases in this study are comparable to the deformation phases (e.g., stretching phase) linked to domains in margin architecture (Lavier and Manatschal, 2006; Peron-Pinvidic et al., 2013). Rifted margin domains comprise the 1) proximal domain (*distributed deformation and*

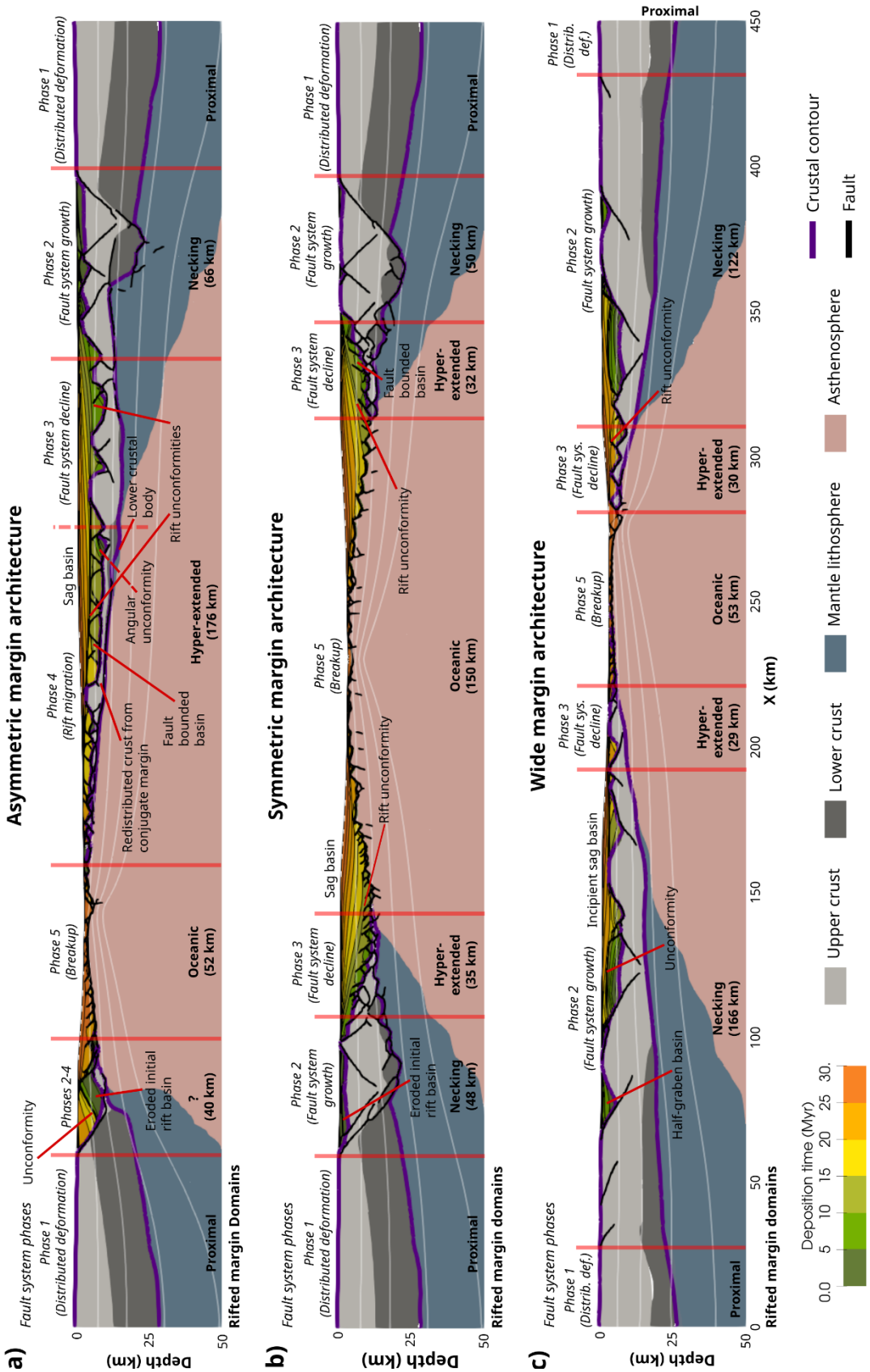

Figure 2.10 Comparison of the margins at 30 Myr to structural domains, showing the similarities between the fault system deformation phase and structural domains. a) Asymmetric margins where deformation phases are indicated in italics on top, and structural domains in bold on bottom. Colored the rheology and deposition time. Extracted fault network is shown in black, and 50 % crustal contour in purple. White temperature contours indicate 200, 400, 600, and 800 °C. b) Symmetric margin. c) Wide margin.

coalescence) to the 2) necking domain (*fault system growth*), 3) hyper-extended domain (*fault system decline and basinward localization*), 4) domain of lithospheric mantle exhumation (no comparable phase), and 5) oceanic crust domain (*continental breakup*; Chenin et al., 2021). Figure 2.10 compares the final architecture of our medium bedrock erodibility models at 30 Myr to the structural domains, where we first define anything outside of the initial border faults as the proximal domain. Second, we examine the time when a phase ends and define any part of the margin that no longer significantly deforms after that time as part of that domain.

Our results demonstrate a close correlation between the deformation phases and the rifted margin domains (Fig. 2.10). Structural domains in symmetric margins, wide margins, and the margin opposite the direction of migration (right margin) in the asymmetric model progress as expected. That we see the same phase and domain progression in all models in this study regardless of the rift type (e.g., symmetric, asymmetric, or wide) and efficiency of surface processes supports the application of deformation domains to the margins of a variety of rift configurations (e.g., Chenin et al., 2021). Additionally, that processes like rift obliquity (Agostini et al., 2009) and sediment supply can extend phases helps explain the large ranges of observed margin domain widths (e.g., 10 to 100 km for the necking domain, Chenin et al., 2017).

Though we find a broad correlation between deformation phases and rifted margin domains, there exist some interesting discrepancies. In our models there is no exposed continental mantle lithosphere (exhumation domain). Instead, hyperextension shifts directly into sediment-overlain asthenosphere exhumation (oceanic domain). In wide rifts, the fault network growth phase is greatly extended and the crust gradually thins over a large region (>122 km), as such distinguishing between the necking and hyperextension domain may be difficult. Rift migration creates a large region of hyper-extended crust that is translated from the margin in the direction of migration (left) to the opposite margin (Brune et al., 2014; Pérez-Gussinyé et al., 2020). This translation of sediment and crustal material fully overprints the remnant necking and hyperextended domains of the left margin, rendering the interpretation in terms of a single structural domain impossible.

2.5 Conclusions

We modeled the tectonic evolution of continental rifts and their interaction with surface processes to address three questions: 1) How do fault networks evolve in different rifts and rifted margins? 2) How are fault systems affected by surface process? 3) How do detachment faults and fault sequentiality evolve during rift migration?

We find that regardless of the rift type (e.g., asymmetric, symmetric, or wide) or the efficiency of surface processes, the active fault network properties such as length, displacement, and number of faults evolve according to five distinct phases that correspond to deformation domains: *phase 1: distributed deformation and coalescence* (proximal domain), *phase 2: fault growth* (necking), *phase 3: fault decline and basinward localization* (hyperextended), *phase 4: rift migration* (hyperextended, unique to asymmetric models), and *phase 5: continental breakup* (oceanic).

Our results suggest that surface processes do not drastically alter the overall rift evolution, but they do delay continental breakup. Similar to previous studies, we find that surface processes increase the lifespan of faults, which extends the fault growth phase. Deposition also enhances hyperextension and prolongs rift migration. We suggest that including surface processes has a stabilizing effect on faulting within models, resulting in less complex faulting patterns. An example of this is the reduced fault network complexity in phases 2 and 3, which suggests that sediment-starved margins exhibit greater fault network complexity in the early stages of rifting.

Our models show that rift migration is accommodated through frictional and viscous deformation in the exhumation channel, which creates a basal detachment fault that is rotated sub-horizontally, similar to the West Iberian S Reflector. Rooted in this channel, multiple normal faults form within a fault generation zone, where fault slip decreases with age and distance from this zone. The shallow parts of the exhumation channel satisfy the conditions for serpentinization, and we find that serpentinization is more likely in sediment-starved rift settings like the Iberian-Newfoundland margins, or the late stages of rift migration.

2.6 Acknowledgements

This study was conducted within the Helmholtz Young Investigators Group CRYSTALS (VH-NG-1132). We thank the Computational Infrastructure for Geodynamics (geodynamics.org), which is funded by the National Science Foundation under award EAR-0949446 and EAR-1550901, for supporting the development of ASPECT. The work was supported by the North-German Supercomputing Alliance (HLRN). Software and input files are found at https://doi.org/10.5281/zenodo.5753144. Figures were made using ParaView, colorscales from Crameri (2018) and Crameri et al., 2020, InkScape, and Python.

Chapter 3 : Formation of continental microplates through rift linkage: Numerical modelling and its application to the Flemish Cap and Sao Paulo Plateau

This study was published in:
Neuharth, D., Brune, S., Glerum, A., Heine, C., & Welford, J. K. (2021). Formation of continental microplates through rift linkage: Numerical modeling and its application to the Flemish Cap and Sao Paulo Plateau. *Geochemistry, Geophysics, Geosystems*, 22, e2020GC009615. https://doi.org/10.1029/2020GC009615

Supplementary animations can be found at: https://doi.org/10.1029/2020GC009615

Abstract
Continental microplates are enigmatic plate boundary features, which can occur in extensional and compressional regimes. Here we focus on microplate formation and their temporal evolution in continental rift settings. To this aim, we employ the geodynamic finite element software ASPECT to conduct 3D lithospheric-scale numerical models from rift inception to continental breakup. We find that depending on the strike-perpendicular offset and crustal strength, rift segments connect or interact through one of four regimes: (1) an oblique rift, (2) a transform fault, (3) a rotating continental microplate or (4) a rift jump. We highlight that rotating microplates form at offsets >200 km in weak to moderately strong crustal setups. We describe the dynamics of microplate evolution from initial rift propagation, to segment overlap, vertical-axis rotation, and eventually continental breakup. These models may explain microplate size and kinematics of the Flemish Cap, the Sao Paulo Plateau, and other continental microplates that formed during continental rifting worldwide.

3.1 Introduction

Microplates have been identified in extensional (e.g., Danakil microplate; Eagles et al., 2002) and compressional regimes (e.g., Tibet microplate; Thatcher, 2007). Contrary to the common picture of large, rigid, tectonic plates surrounded by weak and narrow plate boundaries, microplates exist at an intermediate scale: they are larger than the fault blocks that make up the narrow plate boundaries, yet smaller and rotate on a different axis than the surrounding tectonic plates (Macdonald et al., 1991; Schouten et al., 1993). While previous explanations for extensional microplates have been based on analogue models (e.g., Dubinin et al., 2018; Katz et al., 2005) or 2D concepts (Müller et al., 2001; Péron-Pinvidic & Manatschal, 2010), the impact of 3D continental rift dynamics, so far, remains unclear.

In this study, we use 3D models to test the hypothesis that extensional microplates form due to offset rift segments. Rift segments may form at an offset due to, for example, along-strike variability that can be caused by inherited weaknesses (Heine et al., 2013; de Wit et al., 2008) or along-strike changes in rheological structure (Brune et al., 2017a; Corti et al., 2019). Eventually, these variabilities may lead to offset rift propagation from opposite directions. Examples of offset rift systems exist along rifted margins, such as in the South Atlantic (Heine et al., 2013), the Jan Mayen microcontinent in the Norwegian-Greenland Sea (Gernigon et al.,

2012), and in the present-day East African and Red Sea Rift System (Calais et al., 2006; Eagles et al., 2002; Stamps et al., 2008; Stamps et al., 2021). The strike-perpendicular offset is likely an important factor in how rift segments eventually link, and the structural features that form in response (Allken et al., 2012; Gerya, 2013a). Based on present-day mid-ocean ridges, it has been shown that offset divergent segments can connect through long transform faults, or, in some cases, interacting ridges overlap and rotate a central microplate located between the two ridges (Macdonald et al., 1991).

Oceanic microplates are tectonic features that form between adjacent extensional zones (e.g., the Easter microplate located at the East Pacific Rise; Naar & Hey, 1991; the Central Lau Nanoplate located east of Fiji; Baxter et al., 2020; Conder & Wiens, 2011). When two offset spreading centers interact, they create drag forces along the edges of the rigid microplate that exists in the overlapping zone (Katz et al., 2005; Schouten et al., 1993). These drag forces rotate the microplate about a vertical axis. The microplate rotation speed increases with the extensional velocity and decreases with the size of the microplate (Schouten et al., 1993). In oceanic crust, overlapping spreading centers have small offsets (2-30 km; Macdonald et al., 1991) and form fast-rotating (~10°/Myr; Naar & Hey, 1991) short-lived (5-10 Myr; Keary et al., 2009) microplates that attach to one margin as a single spreading center becomes dominant.

Microplates can form in continental crust between overlapping offset rifts. The offset needed for microplate formation is related to the thickness of the brittle layer in the lithosphere (Vendeville & Le Calvez, 1995), which is significantly larger in incipient rifts than in proximity of mid-oceanic spreading centres. Thus continental microplates are likely larger and slower than oceanic ones. For example, in East Africa two rift branches guided by preexisting weak suture zones overlap and rotate the Victoria microplate by ~0.07°/Myr (Glerum et al., 2020). Evidence for remnant continental microplates exists along passive margins, where seismic data suggest thinned crust surrounding regions of relatively thick continental crust (e.g., the Flemish Cap; Welford et al., 2012) or magmatic crust which may contain some mixture of continental crust (e.g., Sao Paulo Plateau; Scotchman et al., 2010).

Other continental promontories that likely formed as microplates via overlapping rift segments can be found in the Atlantic Ocean: the Galicia Bank, Porcupine Bank, Rockall Bank offshore Western Europe, and the Faroes/Fugloy ridge North of Scotland (King et al., 2020; Peace et al., 2019; Scotchman et al., 2010; Yang & Welford, 2021), the NE Brazilian Sergipe Microplate that is bordered by the failed Tucano and Jatoba Rifts (Heine et al., 2013; Szatmari & Milani, 1999), as well as the Falkland Islands microcontinent (Stanca et al., 2019). A prominent example in the Indian Ocean is Sri Lanka (Gibbons et al., 2013; Premarathne et al., 2016), and a perhaps less obvious one is the Exmouth Plateau on the Australian NW Shelf which operated briefly in the late Jurassic (Heine & Müller, 2005; Longley et al., 2002). Despite ample evidence of actively rotating and remnant continental microplates, there is only scarce observational data to constrain the evolution of a continental microplate from initial fault propagation to overlapping rift arms and rotation, and eventually, to continental-breakup and seafloor spreading.

In this study, we use numerical modelling to elucidate when continental microplates form, how they evolve, and how modelled microplates compare to real world examples. We perform 3D extensional simulations where we vary key parameters such as the along-strike and strike-perpendicular offsets of the initial rift segments, the crustal strength, and the lithosphere thickness (Fig. 3.1). The models are extended for 25 Myr, often past continental breakup, and

allow us to characterize the general types of rift linkage and to assess how these connections vary through our parameter space. Finally, we compare a representative model to two possible microplates, the Flemish Cap and Sao Paulo Plateau, located in the North and South Atlantic, respectively. Our models reveal similarities in the general geometry (e.g., microplate size and crustal thickness patterns) and the mechanisms involved in its formation.

3.2 Methods

3.2.1 Governing equations

We perform numerical simulations of a 3D extensional system using the open source finite-element code ASPECT (Advanced Solver for Problems in Earth's ConvecTion, version 2.1.0; Heister et al., 2017; Kronbichler et al., 2012; Rose et al., 2017; Bangerth et al., 2019). While this software was originally developed to study global mantle convection, it has successfully been adopted to model geodynamic processes of lithosphere deformation (Heckenbach et al., 2021; Heron et al., 2019; Muluneh et al., 2020; Naliboff et al., 2020; Sandiford et al., 2021). ASPECT solves the following extended Boussinesq conservation equations assuming an infinite Prandtl number (i.e. without the inertial term),

$$-\nabla \cdot (2\eta\dot{\varepsilon}) + \nabla P = \rho \boldsymbol{g}, \tag{3.1}$$

$$\nabla \cdot (\boldsymbol{u}) = 0, \tag{3.2}$$

$$\bar{\rho} C_p \left(\frac{\partial T}{\partial t} + \boldsymbol{u} \cdot \nabla T\right) - \nabla \cdot k\nabla T = \bar{\rho} H + (2\eta\dot{\varepsilon}) : \dot{\varepsilon} + \alpha T (\boldsymbol{u} \cdot \nabla P), \tag{3.3}$$

$$\frac{\partial c_i}{\partial t} + \boldsymbol{u} \cdot \nabla c_i = q_i \tag{3.4}$$

where equation (3.1) represents the conservation of momentum, with η the effective viscosity, $\dot{\varepsilon}$ the deviator of the strain rate tensor (defined as $\frac{1}{2}(\nabla \boldsymbol{u} + (\nabla \boldsymbol{u})^{\mathrm{T}})$), $\boldsymbol{u}$ the velocity, P the pressure, ρ the density, and $\boldsymbol{g}$ gravity. Equation (3.2) describes the conservation of volume. Equation (3.3) represents the conservation of energy where $\bar{\rho}$ is the reference adiabatic density, C_p the specific heat capacity, T the temperature, k the thermal conductivity, H the radiogenic heating, and α the thermal expansivity. As right-hand-side heating terms, we include radioactive heating, frictional heating, and adiabatic heating from top to bottom, respectively. Finally, we solve the advection equation (3.4) for each compositional field c_i (e.g., upper crust, lower crust, and accumulated plastic strain) with nonzero reaction rate q_i only for the plastic strain field.

3.2.1.1 Rheology

We use a viscoplastic rheology (Glerum et al., 2018), which additionally includes plastic weakening based on accumulated plastic strain. In the viscous regime, we use a composite of diffusion and dislocation creep (Karato & Wu, 1993), formulated as:

$$\eta_{eff}^{diff|dis} = \frac{1}{2} A_{diff|dis}^{\frac{-1}{n}} d^{m} \dot{\varepsilon}_{e}^{\frac{1-n}{n}} \exp\left(\frac{\left(E_{diff|dis} + PV_{diff|dis}\right)}{nRT}\right), \quad (3.5)$$

where A is a scalar prefactor, d the grain size, $\dot{\varepsilon}_e$ the square root of second invariant of the deviatoric strain rate, E the activation energy, P the pressure, V the activation volume, R the gas constant, T the temperature, and n the stress exponent. For diffusion, $n = 1$ and the equation becomes independent of strain rate. For dislocation creep, the grain size exponent m vanishes, rendering dislocation creep independent of grain size. Values for A, E, V, and n used in our models are composition-dependent and found in supplementary Table B.1.

In the plastic regime, when viscous stresses exceed the yield stress, we use the Drucker-Prager yield criterion (Davis & Selvadurai, 2002). The effective plastic viscosity is given by

$$\eta_{eff}^{pl} = \frac{\frac{6C\cos\phi}{\sqrt{3}(3-sin\phi)} + \frac{6P\,sin\phi}{\sqrt{3}(3-sin\phi)}}{2\dot{\varepsilon}_e}, \quad (3.6)$$

where C is the cohesion and ϕ the internal angle of friction. The accumulation of plastic strain is tracked as a compositional field. This field is used to linearly weaken ϕ from an initial value of 26.56° (friction coefficient of 0.5) to a final value of 2.656° (friction coefficient of 0.05) over the accumulated plastic strain interval of 0 to 1. The time-integrated value of the strain reaction rate q_i is approximated as $\dot{\varepsilon}_e \cdot dt$ when plastic yielding occurs (with dt the timestep size).

3.2.2 Model setup

In this study we examine how the initial placement of two rift arms affects their connection. We therefore set up a 3D box model with dimensions 900x600x160 km (X, Y, and Z, where Z is depth) and 4 compositions representing a wet quartzite upper crust (Rutter & Brodie, 2004), wet anorthite lower crust (Rybacki et al., 2006), and dry olivine lithospheric mantle and asthenosphere (Hirth & Kohlstedt, 2003; Fig. 3.1). The total crustal thickness is set to 35 km, with the reference models using a ratio of 25 km upper to 10 km lower crust, a crustal configuration that is representative of typical continental interiors (Mooney, 2010; Pasyanos et

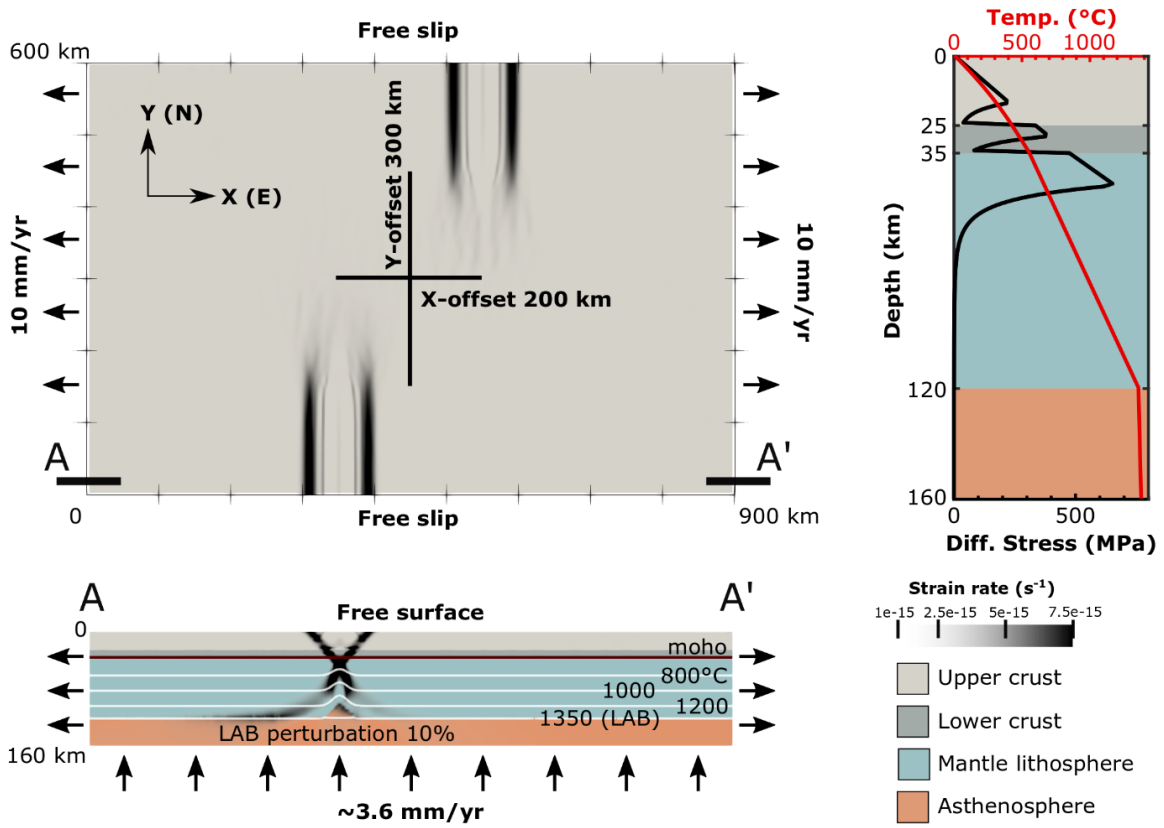

Figure 3.1 Reference model setup for a Y-offset of 300 km and an X-offset of 200 km, depicted at 0 Myr model time. A vertical slice at 0 Myr is included to show the initial strain that localizes above the thermal/compositional lithosphere-asthenosphere boundary perturbation. A strength profile shows a temperature (red) and strength (black) profile, and the unperturbed compositional depths. The yield strength profile is computed using a reference strain rate of 7.05e−16 1/s, the initial bulk strain rate. Density profile given in Figure S1.

al., 2014). This ratio is varied when testing the crustal strength. The lithospheric mantle extends between the crust and the lithosphere-asthenosphere boundary (LAB) at 120 km depth. The LAB depth represents a typical, i.e. non-cratonic, non-orogenic, intracontinental setting (Artemieva, 2006; Pasyanos et al., 2014). The remaining material beneath the LAB is considered asthenosphere.

The model mesh consists of 3 different levels of resolution based on model depth. The maximum resolution of 5 km extends from the surface to 50 km depth, where the transition from plastic to viscous yielding in the mantle lithosphere generally occurs. This allows us to resolve all plastically deforming material at the highest resolution. Lower resolved 10-km mesh cells are then used until 80 km depth, and below that the remaining lithospheric mantle and asthenosphere are resolved at 20 km.

The initial temperature above the LAB is determined by a steady-state geotherm (Turcotte & Schubert, 2013), and below by a mantle adiabat. For simplicity, the initial rift arms are seeded through a small perturbation: we raise the LAB locally by 10% of the lithospheric thickness. We fix the top boundary temperature at 0 °C, and the bottom boundary at the temperature initially determined from the mantle adiabat. All other boundaries are set to zero heat-flux.

Mechanically, the model is extended for 25 Myr at a velocity of 20 mm/yr giving a total extension of 500 km. This involves prescribed outflow of 10 mm/yr on the east and west

boundaries, with inflow through the bottom boundary to conserve volume. The north and south boundaries are set to free slip, and the top boundary is a true free surface.

Although our model captures some of the complexity involved in rift systems, we note that there are several processes which likely affect rift evolution that are not included. For instance, in the models presented here we assume deformation initially localizes above seeded LAB perturbations, however in nature this localization may instead be related to plume activity (Buiter & Torsvik, 2014; Koptev et al., 2018). Additionally, while the lithosphere thickness varies spatially (Artemieva & Mooney, 2001; Artemieva, 2006; Koptev & Ershov, 2011) and likely includes heterogeneities, our models are spatially homogeneous and we do not consider how crustal or lithospheric-scale inheritance may affect the results (e.g. mantle scarring; Heron et al., 2019). Also, we do not consider the movement and deposition of sediment through surface processes. Finally, magmatic processes such as the thermal effect of melt and its movement (e.g., diking and underplating) are not considered, which may result in less drastic weakening (Bahadori & Holt, 2019; Gerya et al, 2015).

3.3 Generic models

In this section, we investigate and discuss the connection between offset rift arms through a series of 48 numerical extension models. We vary 4 parameters to test their effect on rift connection: (1) the offset of pre-defined rift arms perpendicular to the rift trend, i.e. in the X-direction (Fig. 3.2 to 3.5); (2) their offset along-strike, i.e. in the Y-direction (Fig. 3.6); (3) the crustal strength (Fig. 3.7); and (4) the lithosphere thickness (supplementary Fig. B.3). Offset in the X-direction is varied from a small initial offset of 100 km up to 400 km, where offset rifts no longer interact (Le Pourhiet et al., 2017). The Y-offset is similarly varied between 100 km and 400 km, always including some positive offset (underlap) to let overlap develop naturally while testing whether the time-dependency of along-strike rift offset directly affects the resulting connection. We vary the crustal strength by changing the crustal ratio of upper to lower crust from 35:0 to 10:25 km to span the range of possible crustal configurations (Mooney, 2010). Finally, the lithosphere thickness is varied between 80 and 140 km.

3.3.1 X-offset results

We run four model simulations with X-offsets of 100, 200, 300, and 400 km. The Y-offset is kept at 300 km and the ratio of upper to lower crust at 25:10 km. In these cases, each change in the X-offset results in a different type of connection, or lack thereof, between the rift arms, and we distinguish 4 different kinematic regimes: *Regime 1*: connection through an oblique rift (Fig. 3.2); *Regime 2*: connection through a transform fault (Fig. 3.3); *Regime 3*: formation of a

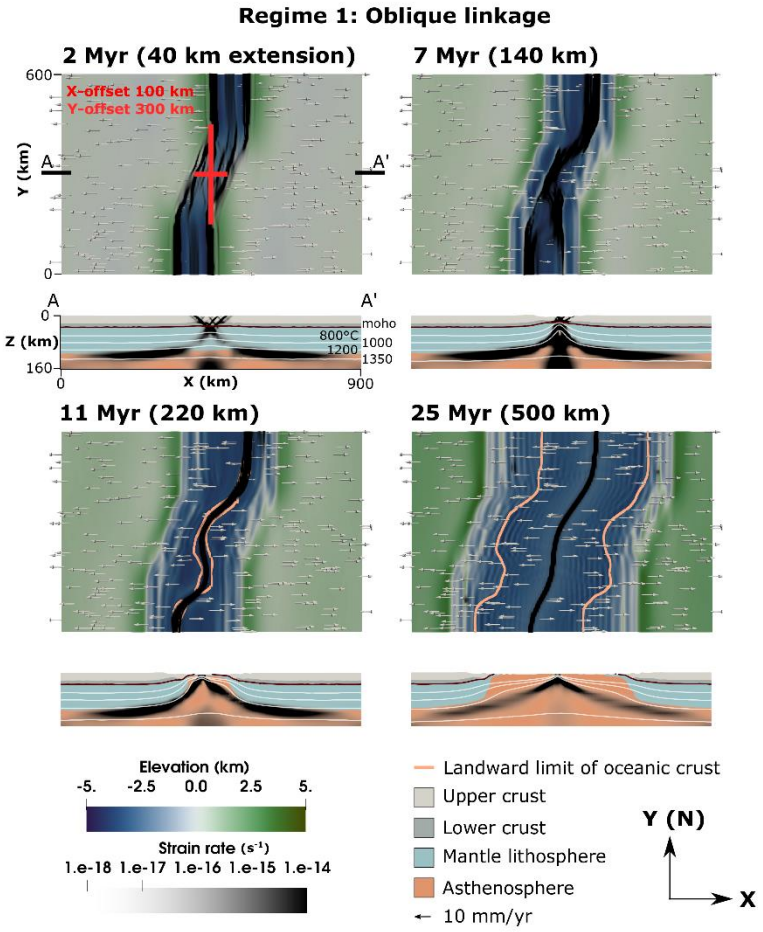

Figure 3.2 Evolution of the oblique linkage in Regime 1. The top down view shows the elevation (green to blue), the strain rate (transparent to black), and the landward limit of oceanic crust (>70% mantle material, orange line). Velocity arrows indicating the horizontal velocity are scaled with the velocity magnitude. Slices show the profile from A to A′ in the *X*-direction (Movie S1). Dark red line shows a contour of the Moho, and white lines temperature contours.

continental microplate followed by an eventual rift jump (Fig. 3.4); and *Regime 4*: rift jump with no interaction between the rifts (Fig. 3.5).

3.3.1.1 *Regime 1*: oblique linkage

Two rift arms are emplaced 100 km apart in the X-direction and strain localizes on two initial faults at a dip angle of ~45° above the perturbation (see Fig. 3.2 and supplementary video B.1). By 2 Myr, a ~3.7 km deep rift valley forms between the initial faults on both sides and strain begins to localize in the center of these valleys. Simultaneously, rift tips propagate into the undeformed crust establishing multiple oblique (azimuth angle of ~25°) faults which bridge the two deeper rift valleys through a ~2 km deep depression (Heidbach et al., 2007) in the center. Deformation transfers from these oblique faults into the center of the rift valley, and by 4.5 Myr the two arms fully connect across the model domain. At this time, a single ~22°-striking oblique fault becomes dominant in the center, while in the north and south deformation continues on two faults which remain orthogonal to extension. As extension continues, rift migration begins and small differences from numerical noise lead to along-strike changes in the migration direction for the central and southern rift segments (Fig. 3.2, 7 Myr). This migration phase ends earlier in the central segment, causing the onset of crustal breakup. By 11 Myr the faults have stabilized and form a continuous fault zone with a general obliquity of ~20° as seafloor spreading begins.

3.3.1.2 *Regime 2*: transform linkage

The initial distance between the rift arms is increased to 200 km in the X-direction, and strain initiates two faults (Fig. 3.3, supplementary video B.2) similar to the previous model. By 2 Myr, the rift tips propagate into the undeformed crust, curving inward toward the opposite rift arm at an ~24° azimuth angle. At 4 Myr, strain localizes in the rift valley of each rift arm, and the initial faults cease to be active. At 6 Myr these new faults link through the topographically high center by a ~75°-striking oblique fault that forms within an oblique necking zone between the offset rift arms. The northern and southern rift arms migrate towards the east and west model boundaries, respectively, until 13.5 Myr, when migration stops and seafloor spreading begins. Like in Le Pourhiet et al. (2017), our models reproduce the process of steady-state rift migration and the generation of wide stretches of hyperextended crust (Brune et al., 2014, 2017b; Pérez-Gussinyé et al., 2020; Svartman Dias et al., 2015; Tetreault & Buiter, 2018). As strain further localizes, a short ~100 km transform fault forms, through continental crust, within the highly oblique fault that connects the two rift arms.

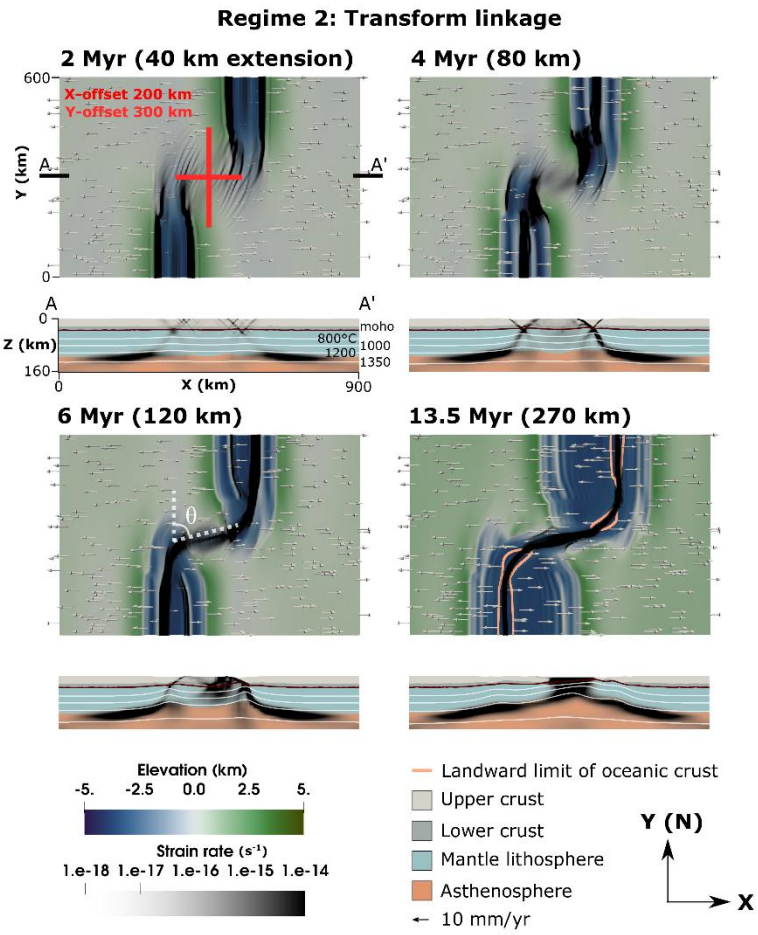

Figure 3.3 Evolution of the transform fault connecting the rifts in Regime 2 (Movie S2), where θ represents the linkage angle. Refer to Figure 2 for explanation.

3.3.1.3 *Regime 3*: microplate formation

The X-offset of the rift arms is further increased to 300 km, and the rift tips initially propagate forward into the undeformed crust (Fig. 3.4, supplementary video B.3). At 2 Myr the tips overlap ~230 km and curve inward at a 20° azimuth angle. Deformation in both rifts localizes in the rift valley forming a center fault. By 7 Myr, the center faults remain generally orthogonal to extension, except the tips which curve inward. As extension continues, the rifts migrate outward to the east and west. Overlap between the rift arms increases as the rift tips, unable to connect through the topographically high center block, propagate forward developing into two

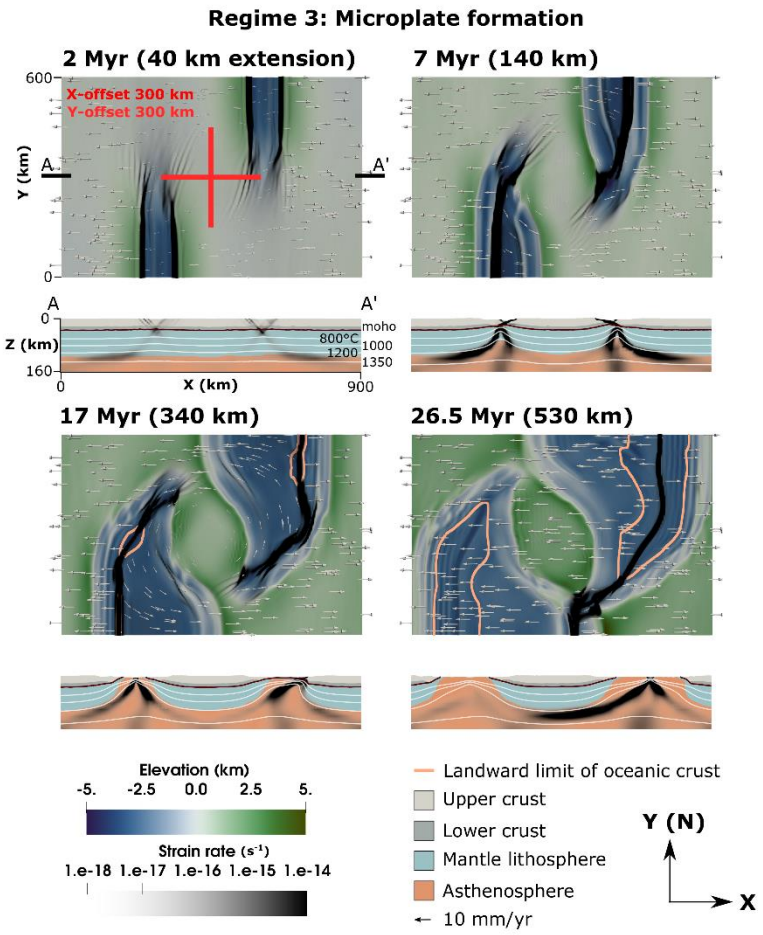

Figure 3.4 Evolution showing the formation and rotation of the microplate seen in Regime 3 (Movie S3). Refer to Figure 2 for explanation.

sections: an orthogonal section near the model north and south boundaries and 50°-striking (east) and 35°-striking (west) oblique sections where the rift arms overlap. Simultaneously, extension causes uplift and counterclockwise rotation of the relatively undeformed center between the overlapping, right-stepping rifts, thus creating a rigid, independently rotating, continental microplate. By 17 Myr, seafloor spreading has begun on both rift arms. Microplate rotation continues as the rifts migrate east-west and propagate north-south, until ~25 Myr when the eastern rift arm reaches the southern boundary, attaching the microplate to the western side. Subsequently, the western rift delocalizes and then fully dies out by 26.5 Myr, leaving a ~240 km wide-uplifted microplate core (measured in the X-direction along the center).

3.3.1.4 *Regime 4*: rift jump to dominant rift

Rift arms are initially emplaced 400 km apart in the X-direction (Fig. 3.5, supplementary video B.4). Initial faults diffusely propagate forward into undeformed crust in the Y-direction, before secondary border faults form, slightly inward, but parallel to the initial ones. At 3.5 Myr, strain begins to localize in the rift valley between the initial faults, establishing a center fault. Simultaneously, the secondary faults continue to propagate through the crust in the Y-direction. By 6 Myr the initial faults are inactive, and the center fault links to one of the secondary faults, which in the case of the eastern rift extend to the southern boundary. In the eastern rift, the center fault propagates along the western secondary border fault localizing in the rift valley created by the two secondary faults. At 9 Myr, the western rift has completely died out while the eastern rift's center fault has crossed the entire model domain. The eastern rift migrates eastward until 15 Myr. At this time, rift migration ceases as seafloor spreading begins.

3.3.1.5 X-offset interpretation

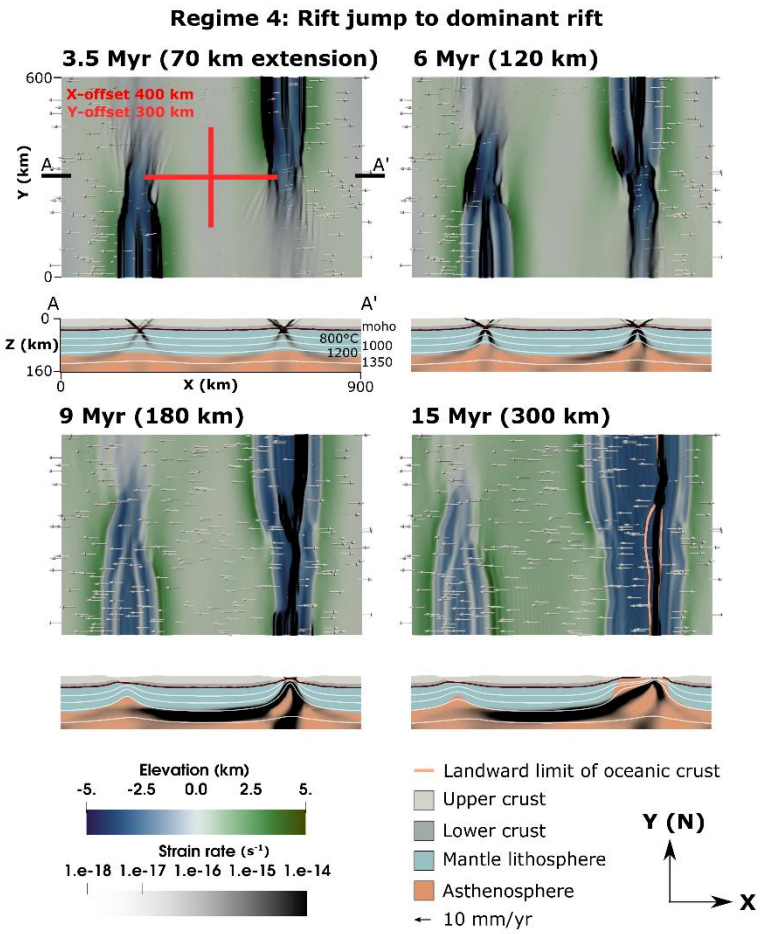

Figure 3.5 Evolution of the rift jump seen in Regime 4 (Movie S4). Refer to Figure 2 for explanation.

The changes in regime with increasing X-offset suggest that X-offset exerts a major control on rift linkage dynamics. Small offsets allow rifts to easily interact and connect through an oblique fault (*Regime 1*). By increasing the offset, the rifts propagate farther forward before connecting. This suggests that, as offset increases, the connecting rift will become more oblique (i.e. higher linkage angle, see θ in Fig. 3.3) until obliquity is high enough to connect the rifts through a transform fault (*Regime 2*). As the offset is further increased (>200 km), the rifts interact but cannot link through the strong continental block between the two rift arms. This leads to further overlap and center block rotation as the faults co-exist, forming a microplate that rotates until an eventual rift jump to the dominant rift. Further increasing the X-offset likely decreases the interaction between the two rifts, lowering the amount of microplate rotation. Eventually, at 400 km, the rifts are too far apart to interact before reaching the opposite model boundary. While in nature at some X-offset rifts should no longer interact, analogue models suggest that the formation of overlapping spreading centers becomes more likely as rift segment length increases relative to the offset (Acocella, 2008). Thus, it is likely that in our models regime 4 is affected by our boundary conditions. To test this, we ran an additional simulation where the length of the model in the Y-direction was increased to 900 km. Indeed, in this case, the rifts interact and a comparably large microplate forms (supplementary Fig. B.2) suggesting that there is no upper limit for the size of a microplate in our model setup.

3.3.2 Y-offset results

In nature, the along-strike offset of two rift arms is a function of time; rifts that propagate along-strike will initially have a large Y-offset that gradually shrinks. Therefore, we expect that the initial Y-offset does not have a large impact on the type of connection. To test this, we perform a series

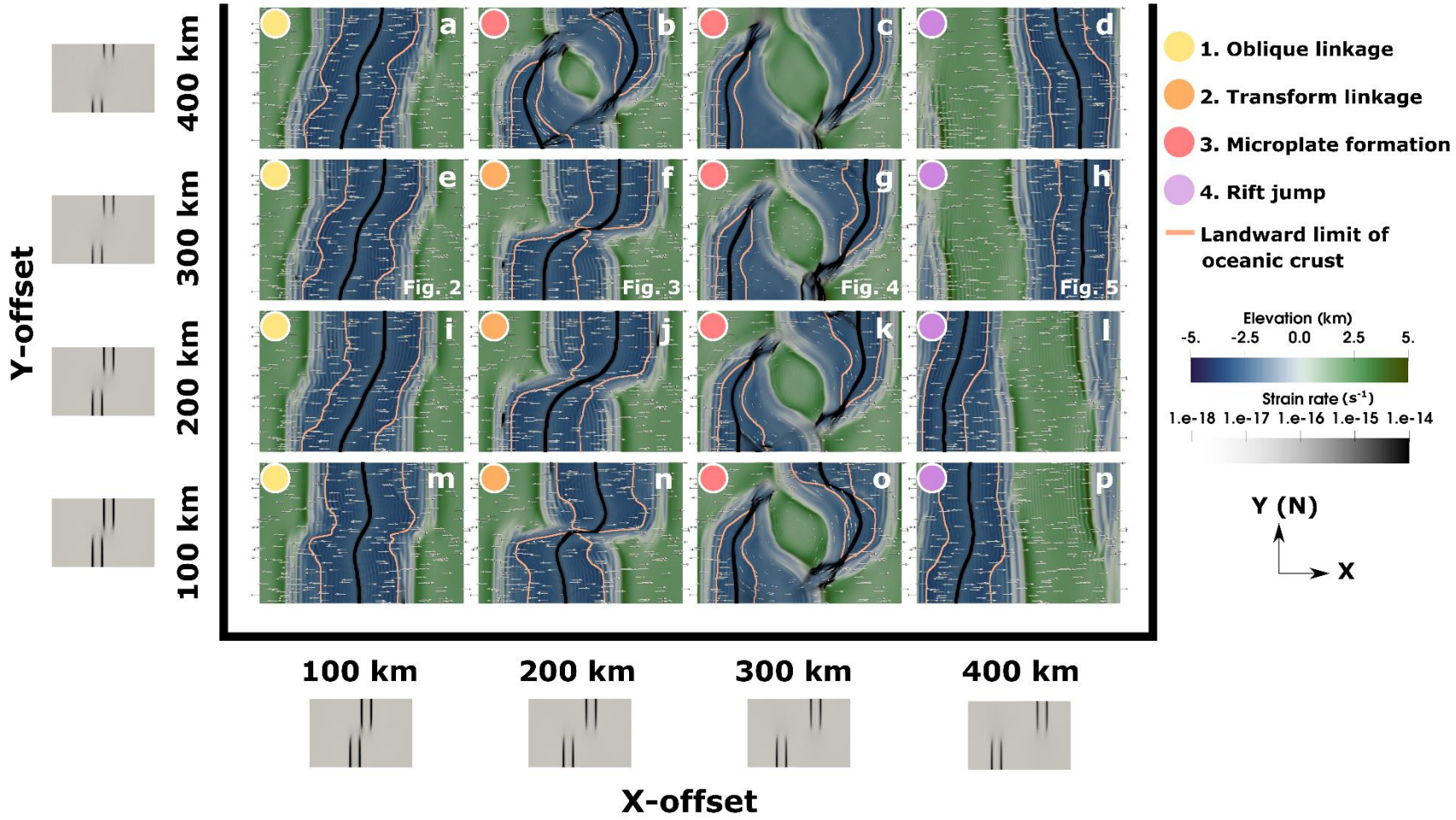

Figure 3.6 Regime diagram showing the types of rift connections seen when varying the initial X- and Y-offset. Models are shown from a top down view at 25 Myr, and are colored by elevation and the strain rate, with the orange line representing the landward limit of oceanic crust (>70% asthenosphere material). Models are divided into regimes shown with colored dots in the top-left corners of the model images.

of models varying the Y-offsets from 100 km to 400 km for each of the previously employed X-offsets, the results of which are shown in Fig. 3.6. Indeed, in almost all cases, the Y-offset did not impact the connection type. This suggests that the time-dependency of the Y-offset does not lead to a certain regime dominating, but rather the rift's X-offset when they are close enough to interact controls the subsequent connection. There is some variation in the connection at X-offsets of 200 km. This may relate to a 200-km X-offset being a transitional length between *Regimes 2* and *3*.

3.3.3 Crustal strength results

To investigate the role crustal strength plays in the connection of offset rifts, we varied the ratios of upper to lower crust between 35:0 (weak), 25:10, 20:15, 15:20, and 10:25 km (strong, see Fig. 7). Otherwise the model setups remain identical to the reference models (Fig. 3.2 to 3.5). Figure 3.7 suggests that crustal strength is an important factor in determining how offset rifts link. In this model setup, a higher crustal strength relates to a higher ratio of plastic to viscous deforming material, which results in greater plastic strain localization. As strain becomes more localized, faults connect rather than diffusely propagating forward, resulting in less overlap as crustal strength increases. Thus, at higher crustal strength, larger initial offsets are needed to form transform faults, and microplates do not form as faults connect instead of overlap.

3.3.4 Lithosphere thickness results

To assess the impact of initial lithosphere thickness on rift linkage, we varied the lithosphere thickness from 80 to 140 km (supplementary Fig. B.3). The setup of these models is similar to those shown in Fig. 3.6e-h, with a crustal ratio of 25:10, Y-offset of 300 km, and variable X-offset between 100 and 400 km, although with a larger Z-extent of 280 km. The resulting regime diagram after 25 Myr is very similar to the model suite where we varied crustal strength (Fig. 3.7), with thicker, colder lithosphere leading to enhanced plastic strain localization similar to having a thicker layer of strong lower crust. Again, the distribution of regimes is largely determined by the X-offset. In contrast to our previous results however, the deformation does not localize in distinct rift segments if the initial lithosphere thickness is smaller than 80 km. In these cases, lithospheric strength is so low that the initial, 10 km thick LAB perturbation that seeds the rift segments is not sufficient in driving rift localization.

3.3.5 Discussion and comparison to previous work

Our study suggests that offset rifts link through four different regimes, which are dependent on the X-offset of the rift arms and the crustal strength. Our results and connection types are similar to what is seen in earlier analogue and numerical experiments, where models connect through transfer zones leading to oblique (like *Regime 1*) or transform fault (*Regime 2*) connections, or by accommodation zones where overlapping spreading centers, which can be considered precursors to microplate development, form (*Regime 3*, Acocella, 2008; Allken et al., 2011, 2012; Gerya, 2013b; Le Pourhiet et al., 2017; Tentler, 2003; Tentler & Acocella, 2010; Zwaan & Schreurs, 2020). Similarly, at large offsets, no rift connection occurs (*Regime 4*, Allken et al., 2011, 2012; Le Calvez & Vendeville, 2002; Le Pourhiet et al., 2017). However,

in many of these previous models smaller initial X-offsets were used (~50-120 km), and in contrast to our study differences were seen when varying the Y-offset (e.g., Tentler & Acocella, 2010).

An important factor in the mode of rift linkage is the linkage angle (with 90° being strike-perpendicular, see θ in Fig. 3.3). In previous analogue modelling studies, the linkage angle was found to be a function of the Y-offset, with the angle increasing as Y-offset was reduced (Tentler & Acocella, 2010). Mechanically, most aforementioned analogue setups involve a brittle layer overlying a viscous material. This setup strongly resembles our models with a crustal ratio of 10:25 km (Fig. 3.7q-t) where nearly the entire crustal region acts as a single brittle block. While we varied the Y-offset in a weaker crustal setup, we found that Y-offset has little effect on overall connection type, which is instead dependent on the X-offset. Similarly, in our reference setup we find that linkage angles increase with the X-offset and not the Y-offset. In addition, Le Pourhiet et al., (2017) suggest that the linkage angle is also a function of crustal strength, and that linkage angles decrease in strong crust. Our findings agree with this (Fig. 3.7, see also supplementary animations), and additionally suggest that the control of the X-offset on rift linkage angles becomes less obvious in strong rheologies. We suggest that due to greater plastic strain localization in stronger crust rift linkage becomes more efficient, thus rifts are likely to link at larger Y-offsets than in weak crust leading to lower linkage angles.

Although we find that overall crustal strength contributes to the style of rift linkage, our models corroborate earlier findings that the integrated brittle strength plays an even more important role. Using crustal-scale models with a brittle upper crust overlying a ductile lower crust, Allken et al. (2011, 2012) suggest that less cohesion and plastic strain weakening favors diffuse rift propagation and overlap. Similarly, we show that models less susceptible to plastic strain weakening (i.e., a lower ratio of brittle to ductile deforming material) have more diffuse rift propagation. In addition, we find that in models with greater integrated brittle strength, rifts are more susceptible to plastic weakening. This generates focused rifts that are likely to connect earlier at lower linkage angles and thus less likely to overlap. If however the integrated brittle strength is lower and localization less effective, rifts propagate more diffusely allowing higher linkage angles and increasing the likelihood of overlap and continental microplate formation. These results suggest that overall crustal strength is less important to the style of rift linkage than the integrated brittle strength. This finding is similar to that of Naliboff and Buiter (2015), who suggested that integrated brittle strength exerts key control on rift reactivation.

An additional factor governing linkage kinematics is rift propagation speed (Jourdon et al., 2020; Le Pourhiet et al., 2018). When propagation is slow, deformation becomes more diffuse. Shortening parallel to the rift propagation direction reduces the rift propagation speed resulting in diffuse V-shaped rift propagation (Le Pourhiet et al., 2018). In our models, where rifts overlap rotation occurs in the overlapping region, and this rotation applies a shortening component to the rift tips (Fig. 3.4, 17 Myr), slowing rift propagation. For *Regime 2*, the overlapping region is small and deformation quickly localizes into strike-slip motion. However, for *Regime 3*, where the rifts

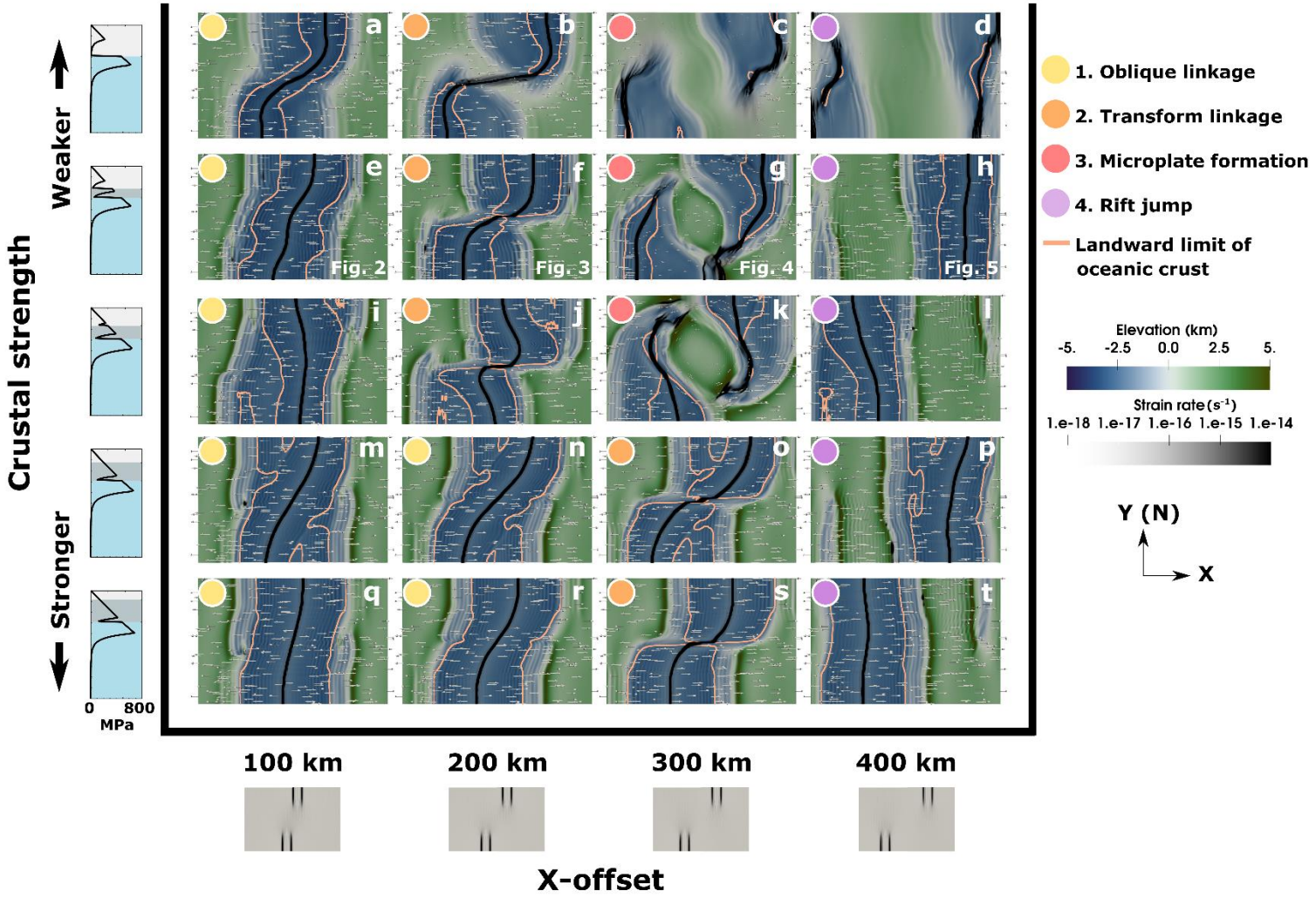

Figure 3.7 Regime diagram showing the types of rift connections when varying the ratio of upper to lower crust, and the initial X-offset. Models are shown from a top down view at 25 Myr, and are colored by elevation and the strain rate, with the orange line representing the landward limit of oceanic crust (>70% asthenosphere material). On the left, strength envelopes are shown, with the compositions of upper (light gray) and lower (dark gray) crust, and mantle lithosphere (blue). Models are divided into regimes shown with colored dots in the top-left corners of the model images.

cannot easily link, rotation continues to apply shortening to the rift tips prolonging microplate rotation and leading to V-shaped propagation on both sides of the microplate. Figure 3.7 suggests that microplates form in a small crustal strength range. In this range strain localization is not so efficient that rifts can not overlap, but not so diffuse that they hardly interact at all.

The thickness of the brittle layer is speculated to determine the maximum X-offset for rift linkage (Allken et al., 2012; Vendeville & Le Calvez, 1995). In accordance with this, analogue experiments have had similar types of rift linkage at much smaller X-offsets than used in this study (Acocella, 2008; Tentler, 2003; Tentler & Acocella, 2010). However, recent lithosphere-scale studies with thermal effects found that rifts can interact at offsets much larger than the brittle layer thickness (<400 km; Le Pourhiet et al., 2017). Our study finds that the 400 km limit is related to boundary conditions (supplementary Fig. B.2), and that in larger domains rifts can still interact and form microplates with a 400 km X-offset. While we investigated the effects of lithosphere thickness on rift linkage, our models are too small to fully explore whether the brittle layer thickness affects the maximum X-offset for rift interaction in lithosphere-scale studies. Additionally, while we vary the lithosphere thickness we do not change our total crustal thickness. Different combinations of crustal setup and lithosphere thicknesses may result in different X-offset ranges for the regimes mentioned in this study.

In this study, transform faults are <200 km, which agrees with earlier studies (Allken et al., 2012; Taras Gerya, 2010, 2012, 2013a, 2013b; Püthe & Gerya, 2014), but in nature transform faults can range from <100 km to >1000 km (Boettcher & Jordan, 2004). Ammann et al. (2017) found that for transform faults >200 km to form, oblique extension is vital. Additionally, in large domains with low extensional velocity they find that overlap and microplate formation are favored over transform faults. This agrees with analogue models, which suggest that a larger total length of rift segments helps rift overlap (Acocella, 2008), while in some cases higher extensional obliquity may promote rift linkage (Zwaan et al., 2016; Zwaan & Schreurs, 2017). Thus, in large domains where microplate formation is more likely, a temporal change in extensional direction to a more oblique orientation, such as during the rifting of the South Atlantic (Heine et al., 2013), may help facilitate a rift jump and lead to a transform fault linking the rift segments attaching the microplate to one side.

While transform faults are an important factor in seafloor spreading, whether they form only during seafloor spreading (Eagles et al., 2015; Nguyen et al., 2016), or can initiate earlier in late-stage continental rifting, is still unclear. Illsley-Kemp et al. (2018) suggest that early proto-transform fault segments can rotate, forming pure strike-slip motion prior to seafloor spreading in magmatically active rift systems. Our results agree with their findings, as prior to seafloor spreading we observe the formation of short nearly pure strike-slip motion transform faults within the highly oblique proto-transform segment connecting some offset rifts (e.g., Fig. 3.3). Additionally, our results suggest that the inclusion of magmatic processes is not required to form such transform faults, and that transform faults can initiate within amagmatic continental rift systems.

3.4 Comparison of numerical models to two natural microplate settings

In this section we discuss how our models compare to two regions where evidence suggests there is a continental microplate, namely the Flemish Cap (Welford et al., 2012) and the Sao

Paulo Plateau (Scotchman et al., 2010). We first compare the reference microplate model evolution to the Flemish Cap, formed during the rifting of the North Atlantic. Second, we focus on the formation of the Sao Paulo Plateau in the Santos Basin, which formed during the rifting of the South Atlantic.

3.4.1 The Flemish Cap geologic setting

The Flemish Cap is a 20-30 km thick continental block (continental ribbon) tethered to the rifted continental margin of offshore Newfoundland, eastern Canada (Funck, 2003; Gerlings et al., 2011; Keen & de Voogd, 1988) (Fig. 3.8b). The broader continental shelf offshore Newfoundland comprises the Grand Banks, the Bonavista Platform, and the Flemish Cap. It consists of basement rocks of the Avalon terrane, a Gondwanan terrane that was accreted to Laurentia (North America) during the Palaeozoic closing of the Iapetus Ocean as part of the Appalachian Orogeny (Haworth & Keen, 1979; Williams, 1984, 1995). During the Mesozoic breakup of the supercontinent Pangaea, rifting and opening of the modern North Atlantic Ocean occurred within the Avalon terrane.

The Flemish Cap lies to the southeast of the deepwater Orphan Basin, out of which it is proposed to have originated (Le Pichon et al., 1977; Sibuet et al., 2004; Srivastava & Verhoef, 1992), with Sibuet et al. (2007) arguing for 43° of clockwise rotation from the Late Triassic to the Early Cretaceous and a further translation of 200-300 km southeastward, relative to North America, from the Late Jurassic to the early Aptian. The Orphan Basin is itself underlain by extended continental crust, with zones of hyperextension resolved using seismic refraction, reflection, and potential field methods (Chian et al., 2001; Gouiza et al., 2017; Lau et al., 2015; Watremez et al., 2015; Welford et al., 2012, 2020). One particularly striking feature of the Orphan Basin is the alignment of zones of hyperextended continental crust (highlighted by peach dashed lines in Fig. 3.8b) that have been interpreted as failed rifts (Chian et al., 2001; Welford et al., 2012, 2020). While the independent rotation of the Flemish Cap relative to North America has been successfully modelled by recent plate reconstructions, both rigid (Nirrengarten et al., 2018) and deformable (Peace et al., 2019), the precise mechanisms that led to the rotation of the Flemish Cap and the failure of rifts within the Orphan Basin are yet to be elucidated.

3.4.2 Flemish Cap comparison and discussion

We compare the first-order crustal architecture of the Flemish Cap to a mirrored version of the reference microplate model (300 km X-offset, 300 km Y-offset, 25:10 crustal ratio, 120 km lithosphere) at 30 Myr model time (Fig. 3.8c). This allows us to examine how rifting would evolve if initial rift placement had a different polarity of rift arm offset. In the model, a 240 km wide microplate core was rotated ~50° and 280 km off the western margin (measured in the X-direction along the center). A small region of oceanic crust formed from the obsolete western rift, and on the eastern side oceanic crust formed along most of the rift. The model had an eastern rift jump that attached the clockwise-rotating microplate to the western margin.

From the comparison of present-day crustal thicknesses across the Newfoundland margin (Fig. 3.8b) and the mirrored microplate modelling results (Fig. 3.8c), the microplate model successfully replicates the scale of the Flemish Cap rotating block, the approximate areal extent

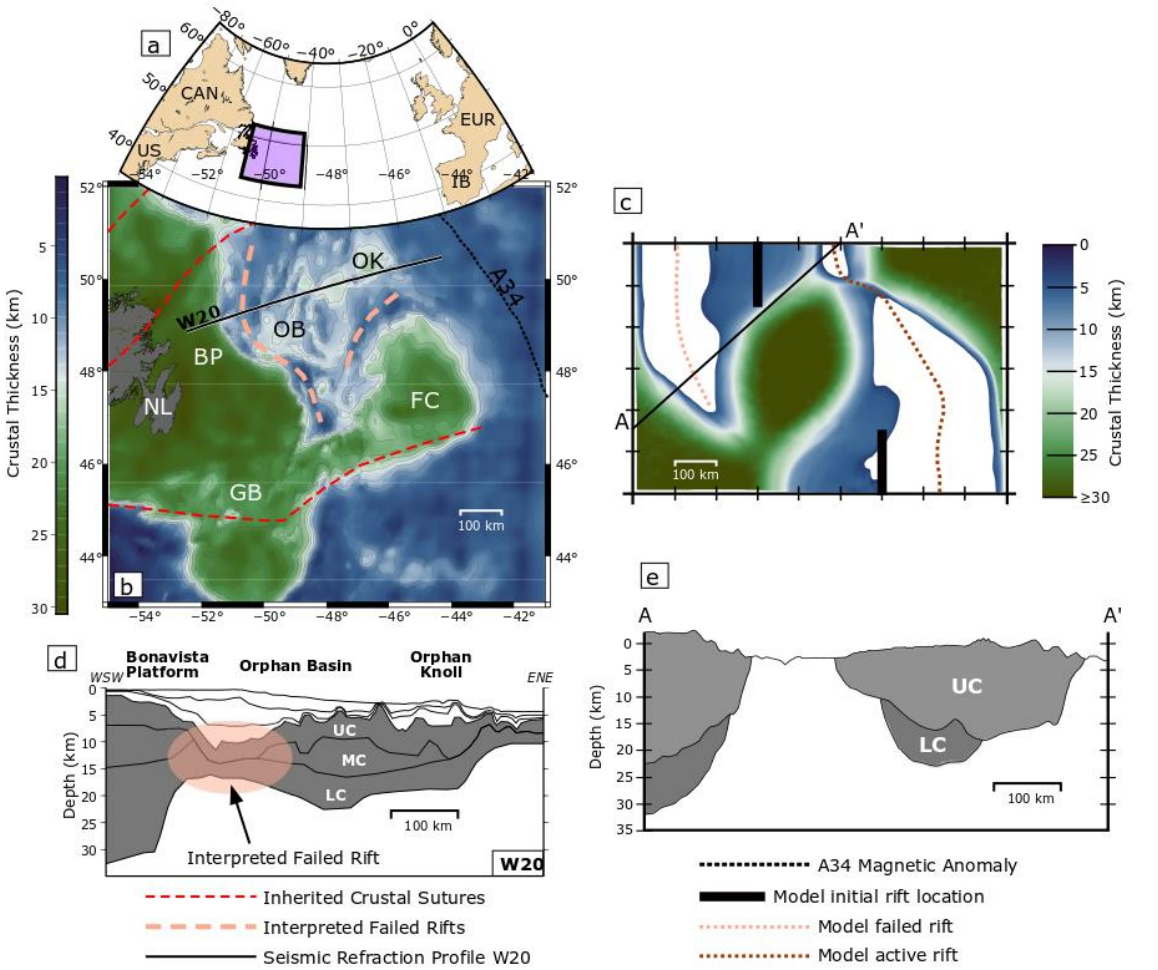

Figure 3.8 (a) Map of the North Atlantic with the extent of map (b) shown in purple; (b) crustal thickness of the offshore Newfoundland margin derived from constrained 3-D gravity inversion (using methodology of Welford et al. [2012]); (c) simulated rift connections for a mirrored microplate model with clockwise rotation; (d) simplified crustal model from Welford et al. (2020) highlighting the interpreted failed rift in the western Orphan Basin. Magnetic anomaly A34 obtained from Srivastava et al. (1990); (e) Cross-section A–A′ through the modeled microplate. Abbreviations: BP, Bonavista Platform; FC, Flemish Cap; GB, Grand Banks; NL, Newfoundland; OB, Orphan Basin; OK, Orphan Knoll; UC, Upper Crust; MC, Middle Crust; LC, Lower Crust.

of rifting in the Orphan Basin, and the eastward rift jump outboard of Flemish Cap leading to the failure of the rifts in the Orphan Basin. The only major discrepancy could be argued to involve the extent of predicted oceanic crust generated in the failed rift branch. To date, no oceanic crust has been interpreted to underlie the Orphan Basin, although crustal velocities within the failed rift along profile W20 in Fig. 3.8d (Welford et al., 2020) do not definitively preclude the presence of oceanic crust.

The modelling results (Fig. 3.8c) reveal that the evolution from initial rift branch interaction, through microplate formation and rotation (~50°), to eventual rift branch failure, can be achieved in less than 35 Myr. This time window is significantly narrower than the Late Triassic to Early Cretaceous time scale proposed by Sibuet et al. (2007) for the Flemish Cap, which is due to the fact that the modelled constant extension velocity of 20 mm/yr (full rate) exceeds divergence velocities of the initial, slow rift phase in this region (Barnett-Moore et al., 2018; Brune et al., 2016; Peace et al., 2019). Nevertheless, careful seismic interpretation of reflection

data within the Orphan Basin is still needed to better constrain the exact timing of the Flemish Cap rotation.

Constrained 3D gravity inversions performed on the conjugate Flemish Cap/Orphan Basin and Irish Atlantic continental margins (Welford et al., 2012) have resolved significantly different rifting styles and compartmentalization. Specifically, on the Irish margin, hyperextended crust beneath sedimentary basins like the Porcupine Basin is abruptly juxtaposed against unstretched crustal blocks like the Porcupine Bank. By contrast, the crust beneath the Orphan Basin appears to have been stretched more uniformly. Based on geodynamic modelling results from Huismans & Beaumont (2011), Welford et al. (2012) argue that fundamental rheological differences controlled the different rifting styles across the conjugate pair and that a weak crustal layer underlies the Orphan Basin. This conclusion is consistent with the results displayed in Figure 3.7 where microplate formation and rotation is predicted for the models involving weaker crust.

3.4.3 Sao Paulo Plateau geologic setting

The Sao Paulo Plateau (SPP) is a marginal plateau (Kumar & Gambôa, 1979; Mohriak et al., 2010) occupying large parts of the Santos Basin on the Brazilian Atlantic margin. It is delimited landward by the wide continental shelf of the Santos Basin, by the Cabo Frio Transfer zone/Rio de Janeiro Fracture Zone to the north, the oceanic crust in the east (approximately coinciding with the Jean Charcot seamounts) and the Sao Paulo escarpment/Florianopolis Fracture zone to the south. Water depths on the SPP range between 2000 m and more than 3000 m (Fig. 3.9b).

The Santos Basin and the SPP were formed during the early Cretaceous as part of the South Atlantic rift system (Chang et al.,1992; Heine et al., 2013; Meisling et al., 2001) and are situated just south of a major rift segment boundary between the central (conjugate Kwanza-Campos Basins) and the southern South Atlantic rift segment (conjugate Santos/Namibe Basins; Guiraud et al., 2010; Meisling et al., 2001). Here, the rift axis is offset to the east by about 300 km along the Cabo Frio-Benguela transform system. Continental extension between Africa and South America commenced in the early Cretaceous, rifting lithosphere composed of reworked Archean inliers, Neoproterozoic magmatic arcs and orogenic belts of the Brasiliano orogenic cycle, with a tectono-thermal age of the lithosphere of approximately Cambrian age (around 550-500 Ma; Neves et al., 2014). Approximately 10 Myrs into rifting, the Tristan da Cunha (TC) plume impinged on the South American plate, creating the Parana-Etendenka Large Igneous Province (Krob et al., 2020 and references therein; Heine et al., 2013), with the conjugate Walvis/Florianopolis ridges being one eruption center in the southern part of the Santos Basin. This magmatic episode with extensive extrusive basalt forms the present-day economic basement (Chang et al., 1992; Moreira et al., 2007). At the time of emplacement, the rift had been extended by approximately 100 km (Heine et al., 2013). Continued extension and waning magmatic budget resulted in a complex rift architecture obscured by a thick layer of Aptian-aged evaporites covering large parts of the basin. Several giant hydrocarbon discoveries in the pre-salt sequences are hosted in shallow water carbonate facies. Subsequent infill of the basin largely consists of mixed carbonate and clastic sediments, affected by complex salt tectonics (Moreira et al., 2007).

The nature of the crust underlying the SPP is debated. Nearly all hydrocarbon wells terminating in the pre-salt sequences throughout the Santos Basin have terminated in basaltic extrusives.

Regional analyses using seismic reflection, refraction and potential field methods (e.g., Borges & Gambôa, 2015; Evain et al., 2015; Klingelhoefer et al., 2014; Meisling et al., 2001; Scotchman et al., 2010; Zalán et al., 2011) conclude that large parts of the Santos Basin and Sao Paulo Plateau are underlain by thin crust of 13-25 km of mixed continental to magmatic crustal type (”heterogenous crust”), thermal buoyancy induced by the Tristan plume has likely resulted in dynamic uplift causing shallow water conditions on the SPP, despite relatively thin crustal thicknesses observed across the plateau (e.g. Evain et al., 2015).

Despite the disagreements on crustal type underlying the SPP and the Santos Basin, the area shows characteristics of microplate formation (Heine et al., 2013; Moulin et al., 2013). In the SW part of the Santos Basin, an aborted oceanic spreading ridge propagator, the Abimael Ridge (sometimes referred to as Avedis ridge), has been identified (e.g., Chang et al., 1992; Meisling et al., 2001; Scotchman et al., 2010). Along the proximal margin of the Santos Basin, potential field data indicate a zone of en echelon Moho uplifts (Meisling et al., 2001) and crustal thinning, along with extensive seaward-dipping reflector sequences (SDRs) indicating accommodation space formation related to crustal extension during a magma-rich rift phase. A faulted base salt surface in the inner, western part of the Santos Basin and isolated graben structures such as the Merluza Graben area in the northern part of the basin (Magee et al., 2021), indicate that the Avedis ridge has been active at least until deposition of the extensive early Aptian-aged evaporite layer in the central South Atlantic. Towards the NE basin margin, this zone merges with the Cabo Frio-Benguela transform (Guiraud et al., 2010; Mohriak et al., 1995), which laterally offsets the rift axis by about 500 km eastwards into the northerly adjoining Campos-Kwanza/Benguela rift segment. Crustal thickness observations and inverse models show that the eastern, distal part of the Santos Basin, east of the Sao Paulo Ridge/High is characterized by a second necking zone (Norton et al., 2016), which further thins the crust and eventually continues into steady-state oceanic crust (Mohriak et al., 2010).

Presently, plate kinematic reconstructions model an initial northward propagation of the southern South Atlantic oceanic spreading ridge into the Abimael Ridge region (Heine et al., 2013; Meisling et al., 2001; Moulin et al., 2013), of the western Santos Basin in pre-salt deposition times (i.e. pre late Albian), being laterally accommodated and offset by the Cabo Frio transform. The deformation focus/spreading ridge of the central South Atlantic is attempting to propagate southward, offset along the Angolan Benguela margin (Guiraud et al., 2010) and eventually overlapping with the Abimael Ridge for a limited amount of time until the Abimael Ridge becomes extinct and deformation is localised along the eastern margin of the Sao Paulo Plateau, forming a continuous spreading ridge connecting the central and south Atlantic rift segments (Heine et al., 2013; Moulin et al., 2013).

3.4.4 Sao Paulo Plateau comparison and discussion

In this section we compare the Sao Paulo Plateau to the reference microplate model at 30 Myr (300 km X-offset, 300 km Y-offset, 25:10 crustal ratio, 120 km lithosphere). The SPP represents a region of thickened crust that formed in a complex system influenced by the impingement of the TC plume, leading to the emplacement of large amounts of magmatic crust. Despite the plume’s influence, the overall geometry of the plateau and western failed rift is comparable to the microplate modelled in this study. In both cases, a region of relatively thick

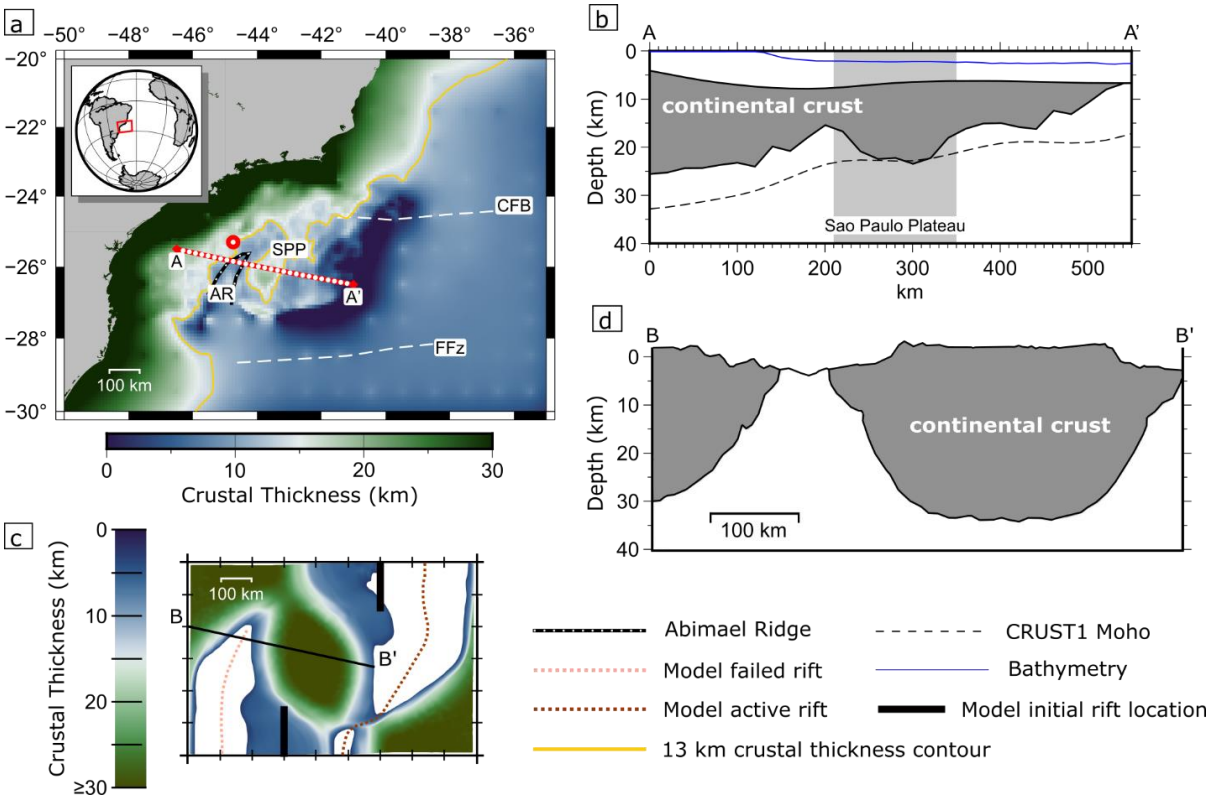

Figure 3.9 (a) Map view of the Santos Basin region colored by continental crustal thickness (Shell proprietary data merged with resampled CRUST1 at 10 km resolution) showing the locations of the Sao Paulo Plateau (SPP) and the aborted Abimael Ridge spreading propagator (AR), red dot indicates approximate position of Merluza Graben. Profile location indicated by red line, with markers spaced in 20 km intervals. Yellow contours show a crustal thickness of 13 km. CFB: Cabo Frio-Benguela Fracture zone, FFz: Florianopolis Fracture zone. (b) Cross-section along the A–A′ profile: Top basement is extracted from resampled CRUST1 data (Bottom of lower sediments layer), lower solid black line is base of crust, computed by adding our crustal thickness estimate to resampled CRUST1 base of lower sediments. Water depth shown as thin in blue line (SRTM15 + V2.1 at 10 km resolution). Gray box highlights the extent of the SPP microplate along the profile. (c) Simulated rift connections for the reference microplate model (Figure 4). (d) Cross-section B–B′ through the modeled microplate.

crust (SPP) is encompassed by thinned crust from a failed western rift (Abimael Ridge region) to the west, and a dominant ocean-forming rift to the east.

Discrepancies between our models and the SPP arise in the size of the microplate and features in the surrounding region. The SPP crustal thickness ranges between 13-25 km and the core is ~140 km wide. This is both smaller and thinner than the microplate modelled in this study. The region is bounded by the Florianapolis fracture zone to the south. Analogue modelling suggests that hard rift linkage is sometimes facilitated with oblique rifting (Zwaan et al., 2016; Zwaan & Schruers, 2017), thus it is possible that the region's directional change in extension may have favored the formation of transform faults to connect the overlapping rift segments.

One limitation in our model is that we do not include melt processes, which may be especially important in the SPP region with the arrival of the TC plume (Beniest et al., 2017; Lavecchia et al., 2017). Even though we do not include melting, we partially address this through an additional supplementary model (supplementary videos B.5 and B.6) where we include the arrival of a thermal mantle plume in two stages to represent the plume head and stem (similar to Bredow et al., 2017; Gassmöller et al., 2016; Koptev et al., 2015; Steinberger et al., 2019).

Because the TC plume did not impinge on the region until ~10 Myr after rifting began, we prescribe the plume arrival in the model at 10 Myr and find that at this stage and without melt processes the plume does not drastically affect model evolution, but plume placement can influence the rift jump direction.

3.5 Conclusions

In this study we show that rift branches that are offset along (Y) or perpendicular (X) to strike connect in 4 ways: *Regime 1*) through an oblique rift, *Regime 2*) through a transform fault, *Regime 3*) by microplate formation with a rift jump to the dominant rift, or *Regime 4*) through a rift jump to the dominant rift without rift interaction. We find that the X-offset is the primary factor determining the connection type. The secondary factor is the effectiveness of plastic strain localization, which in this case relates to the crustal strength or lithosphere thickness. In weaker crust, the integrated brittle strength is lower and the models are less susceptible to plastic weakening, which leads to more diffuse rift propagation. This diffuse propagation promotes rift overlap, which slows rift propagation, causing rotation and microplate formation. In stronger crust with higher integrated brittle strength, plastic strain is more localized and rift connection becomes more efficient; in these cases microplates do not form and oblique and transform fault connections occur at larger X-offsets.

The microplates modelled in this study exhibit a core of poorly thinned continental crust that has been rotated (counter-clockwise for right-stepping rift segments, clockwise for left-stepping ones). Pronounced thinning occurred on both sides of the microplate from two coexisting rifts, with an oceanward rift jump rendering the landward rift obsolete. Early rift geometries and interactions in the microplate models resemble the East African Rift System and show that overlapping rifts with a rotating microplate can form without the guidance of lithospheric strength heterogeneities (e.g., mobile belts; Glerum et al., 2020). Additionally, the reference model elucidates many features of the Flemish Cap and Sao Paulo Plateau, two extensional microplates that formed during the rifting of the North and South Atlantic, respectively. In both regions there exists thinning to both sides of a relatively thick core that has been rotated oceanward off the margin. Both areas are also associated with a landward failed rift and a likely rift jump to the dominant ocean-forming rift. Beyond these two examples, our modelled evolution of microplate kinematics could be a template to understand the formation of other continental promontories at rifted margins across a range of scales worldwide, such as the Galicia, Porcupine, and Rockall Banks, the Faroes/Fugloy ridge, Jan Mayen, the NE Brazil Borborema Province/Sergpipe Block, the Falkland Islands microcontinent, the Exmouth Plateau on the Australian NW Shelf, and Sri Lanka.

3.6 Acknowledgements

This study was conducted within the Helmholtz Young Investigators Group CRYSTALS (VH-NG-1132). The authors thank the Computational Infrastructure for Geodynamics (geodynamics.org), which is funded by the National Science Foundation under award EAR-0949446 and EAR-1550901, for supporting the development of ASPECT. The work was supported by the North-German Supercomputing Alliance (HLRN). Figures in this paper were made with ParaView, the Generic Mapping Tools (Wessel et al., 2019), and InkScape, and color scales are from Crameri (2018). The authors thank Shell Global Solutions International

B.V. for the permission to publish the higher resolution crustal thickness data for the Santos Basin which was kindly provided by Lorcan Kennan. The authors would like to thank the reviewers Laetitia Le Pourhiet, Alexander Koptev, and Michael Nirrengarten for their detailed and constructive feedback on this manuscript.

Chapter 4 : Flexural strike-slip basins

This study was published in:
Neuharth, D., Brune, S., Glerum, A., Yuan, X. P., & Braun J. (2021). Flexural strike-slip basins. *Geology*, https://doi.org/10.1130/G49351.1

Supplementary animations can be found at: https://doi.org/10.1130/G49351.1

Abstract

Strike-slip faults are classically associated with pull-apart basins where continental crust is thinned between two laterally offset fault segments. We propose a subsidence mechanism to explain the formation of a new type of basin where no substantial segment offset or syn-strike-slip thinning is observed. Such "flexural strike-slip basins" form due to a sediment load creating accommodation space by bending the lithosphere. We use a two-way coupling between the geodynamic code ASPECT and surface-processes code FastScape to show that flexural strike-slip basins emerge if sediment is deposited on thin lithosphere close to a strike-slip fault. These conditions were met at the Andaman Basin Central fault (Andaman Sea, Indian Ocean), where seismic reflection data provide evidence of a laterally extensive flexural basin with a depocenter located parallel to the strike-slip fault trace.

4.1 Motivation

Near plate boundaries, accommodation space for sedimentary basins is created by (1) lithospheric stretching or cooling, which controls rift-basin formation at divergent boundaries, and (2) lithospheric flexure such as in foreland basins in convergent settings and cratonic sag basins in continental interiors (Allen and Allen, 2013). Pull-apart basins at transform plate boundaries are thought to be related to the first process.

Pull-apart basins form between laterally offset strike-slip fault segments (Mann et al., 1983; Gürbüz, 2010). During strike-slip motion, the area between the offset faults is extended and basement subsidence occurs in this area due to crustal thinning (van Wijk et al., 2017). Pull-apart basins lengthen over time and form as long thin basins with a depocenter that is bounded by the strike- or oblique-slip segments (Seeber et al., 2004). While there are many pull-apart basin examples (e.g., the Dead Sea Basin: Garfunkel and Ben-Avraham, 1996; Death Valley Basin: Serpa et al., 1988), there has not been much discussion on other types of strike-slip basins.

Flexural basins form when an overlying load deflects the lithosphere, e.g., during mountain building, where an orogenic load creates accommodation space for sediment infill. However, under conditions without an orogenic load, basement subsidence may be a consequence of lower-crustal flow triggered by enhanced sedimentation in deep basins (Morley and Westaway, 2006; Clift et al., 2015), e.g., the fans of the Red River (Clift and Sun, 2006) and Pearl River (Dong et al., 2020; both examples are located at the northern continental margin of the South China Sea).

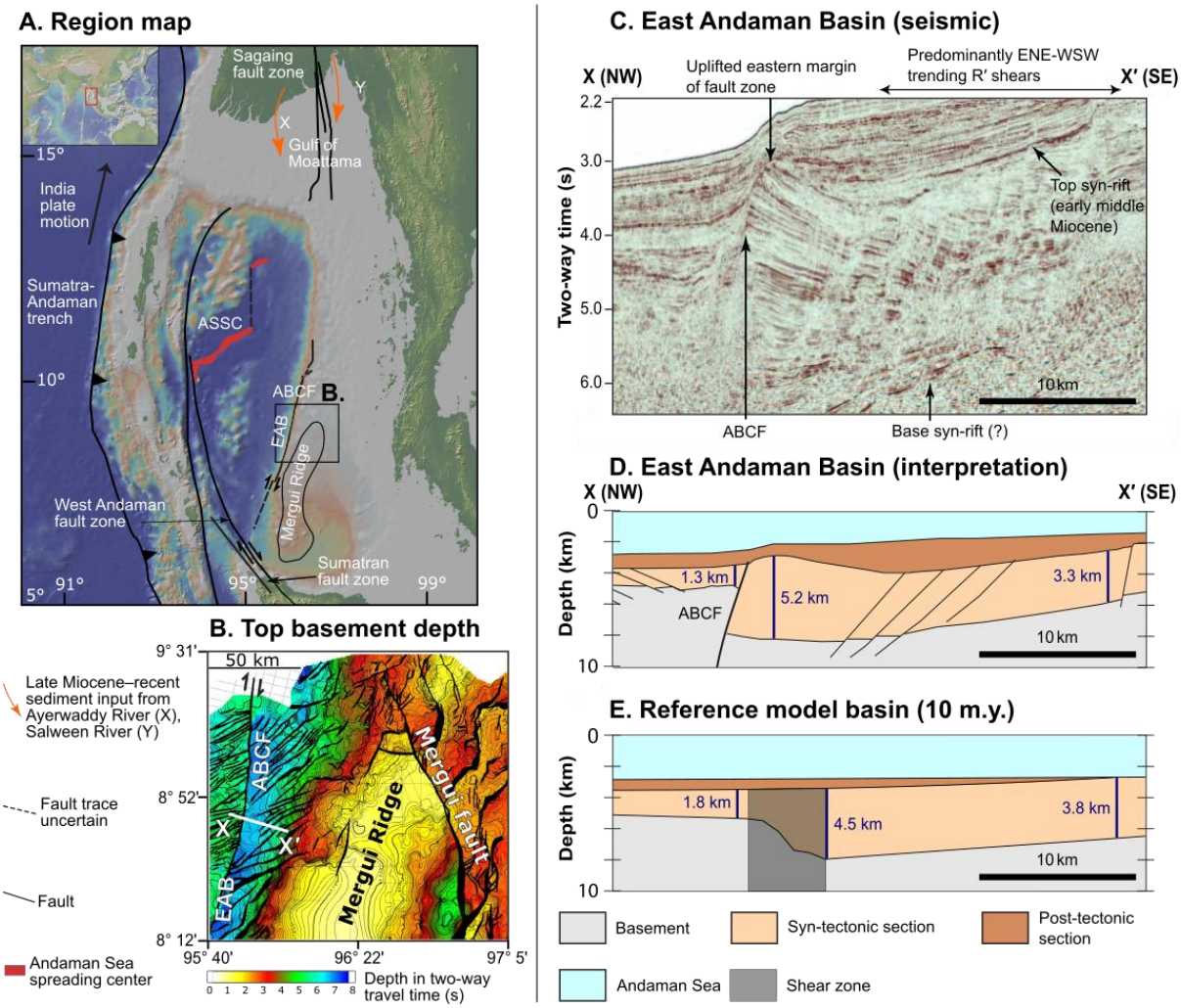

Figure 4.1 (A) Andaman Sea map. ASSC—Andaman Sea spreading center; ABCF—Andaman Basin Central fault; EAB—East Andaman Basin. (B) Depth to the top of the basement in two-way travel time. (C) Seismic data of the EAB. See B for profile location. (D) Depth interpretation of C. (E) Modeled basin. Post-tectonic sediment is computed by adding basement subsidence from 5 to 10 m.y. to the topography at 5 m.y.

We infer that the creation of sedimentation-induced accommodation space requires and is enhanced by (1) an easily deformable tectonic environment, and (2) focused sedimentation. Both can occur in regions of prior tectonic subsidence. Furthermore, because strike-slip faults may represent highly weakened plate boundaries (Zoback et al., 1987; Provost and Houston, 2003) and transform continental margins commonly follow a phase of thinning (Jourdon et al., 2021), we formulate the key hypothesis of this study: regions near strike-slip faults can represent a combination of factors whereby significant basement subsidence is driven by sedimentary loading. The positive feedback between focused sedimentation and flexural subsidence leads to the creation of a previously unrecognized type of basin that we term "flexural strike-slip basin". We test our hypothesis by (1) numerical forward modeling of a strike-slip system subjected to asymmetric sedimentation, and (2) seismic reflection interpretation from the East Andaman Basin (EAB) in the Andaman Sea (Indian Ocean).

4.2 Geological setting of the Andaman Sea

During the Cenozoic, the Andaman Sea formed a transtensional backarc basin when India coupled with western Myanmar (Curray, 2005). Multiple strike-slip faults exist in the region, including the active, dextral, Sagaing fault (Fig. 4.1; 18 mm/yr: Vigny et al., 2003; Maurin et al., 2010) in the northeast of the Andaman Sea that connects southwestward to the Andaman spreading center (Curray, 2005). South of the Sagaing fault is the inactive Andaman Basin Central (strike-slip) fault (ABCF; Morley, 2016, 2017; Mahattanachai et al., 2021).

The Andaman Sea's transtensional motion led to subsidence and a submarine environment, causing the area to act as a sediment trap. Fault trends suggest the region near the ABCF experienced WNW-ESE extension in the Oligocene that shifted to NNW-SSE transtensional strike-slip motion during the early to mid-Miocene (lasting ∼5 m.y.; Morley, 2017). The ABCF follows a previous necking zone of hyperextended continental crust (7–10 km thick; Morley, 2017; Mahattanachai et al., 2021). During strike-slip motion, the easterly Mergui Ridge was partially subaerial and, along with peninsular Thailand, acted as an asymmetric clastic sediment source for the EAB located along the ABCF (Mahattanachai et al., 2021).

The geometry of the EAB in relation to the ABCF is described in detail by Mahattanachai et al. (2021), who concluded that the long (>200 km), deep (>4 km), westward-thickening basin on the east side of the sub-vertical fault did not fit classic extensional or pull-apart basin characteristics.

4.3 Model setup and evolution

We reproduce the key aspects of the ABCF region, namely that of a submarine environment, thin lithosphere, and asymmetric sedimentation, using a viscoplastic 100 × 8 × 120 km (*X*, *Y*, *Z*) three-dimensional box model via a two-way coupling of the tectonic code ASPECT (https://aspect.geodynamics.org, version 2.3.0-pre, commit 886749d) (Figs. 4.2B and 4.2C; Kronbichler et al., 2012; Heister et al., 2017; Glerum et al., 2018; Bangerth et al., 2019; Text C.1 in the Supplemental Material) and the surface-processes code FastScape (https://fastscape.org) (Braun and Willett, 2013; Yuan et al., 2019b, 2019a; Text C.2). We assume that a previous extensional event left the region submarine with thinned, 40-km-thick lithosphere. The model is initialized with 4 km of upper crust, 4 km of lower crust, 32 km of mantle lithosphere, and 80 km of asthenosphere (Fig. 4.2B; Fig. C.1 in the Supplemental Material). The eastern boundary (right edge in Fig. 4.2B) has no slip in any direction, the western boundary (left edge in Fig. 4.2B) has no slip in the *Z* direction, 20 mm/yr in the *Y* direction to induce strike-slip motion, and is given a small (0.2 mm/yr) extensional component in the *X* direction that helps avoid bending-induced compression but does not affect the presented results (Fig. C.2). To simulate an infinitely long strike-slip fault with minimal along-strike variation, the northern and southern boundaries are periodic, in that any material advected out of the northern boundary will flow into the model from the southern boundary, or vice-versa. The initial lithostatic pressure at a reference location is prescribed on the bottom boundary to allow for outflow in response to sedimentation. The strike-slip fault forms self-consistently above an initial perturbation of the lithosphere-asthenosphere boundary (10% reduction of lithosphere thickness) in the center of the model that acts as a weak zone for

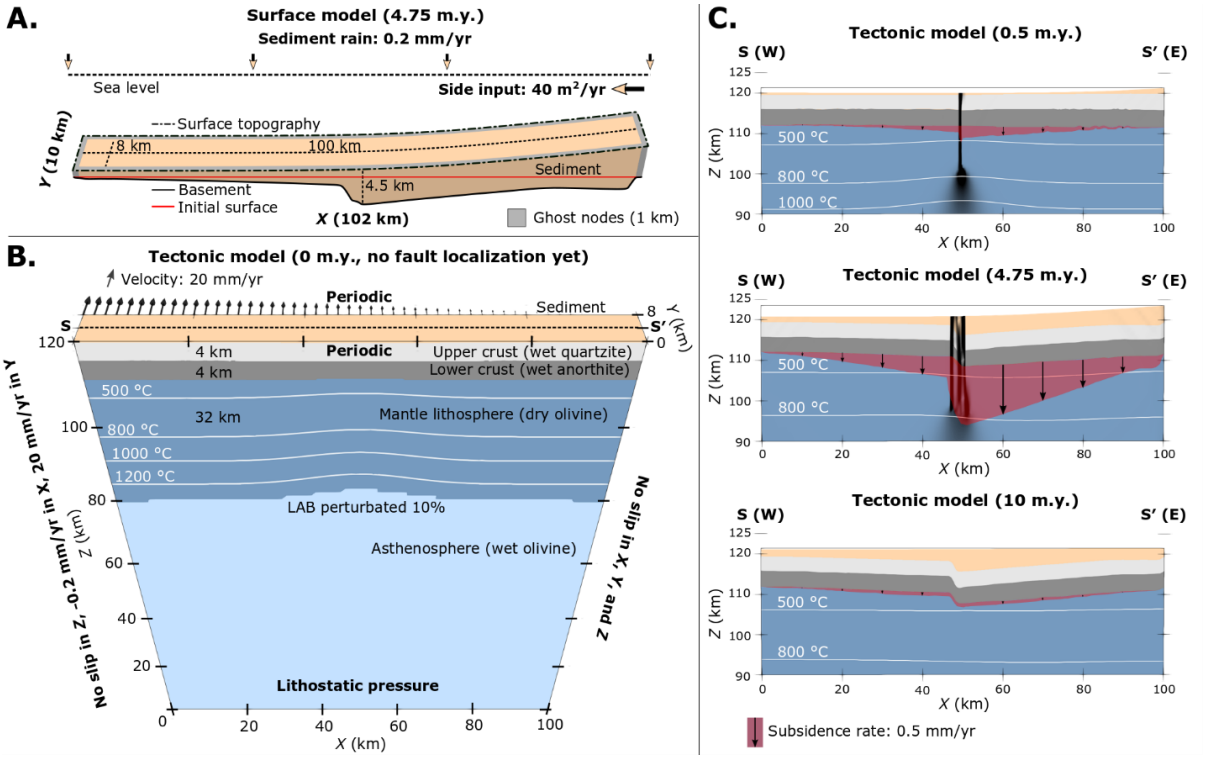

Figure 4.2 (A) Surface-processes model at 4.75 m.y. and 2× vertical exaggeration. Sediment (beige) is the area between topography (dash-dot line) and basement (solid black line). Ghost nodes (gray) are a single cell-size (1 km in *X* and *Y*) layer surrounding the surface processes model implemented for periodic advection along the *Y* direction and to control sedimentary side input, surround the surface model and do not interact with the tectonic model. (B) Initial tectonic setup. Colors represent composition; white isotherms represent temperature distribution. Arrows indicate total velocity magnitude. The northern and southern boundaries are periodic, indicating that material flow out one boundary will become inflow on the opposing boundary. LAB—lithosphere-asthenosphere boundary. (C) Cross sections of the top 30 km of the tectonic model along S-S′ in B showcase the formation of a flexural strike-slip basin in response to sedimentation. Subsidence rate at the Moho is indicated in red. See Movies C.1 and C.2 in the Supplemental Material.

deformation to localize. Accumulated plastic strain over an interval of 0–1 weakens the angle of friction from an initial value of 30° to a final value of 7.5°, promoting brittle localization.

The surface-processes code FastScape is coupled to the top of the tectonic model (Text C.3). The model is submarine and sediment is transported via diffusion with a coefficient of 500 m^2/yr, consistent with open-marine environments in previous modeling studies (Rouby et al., 2013). Sediment is supplied to the domain in two ways: (1) the entire surface experiences 0.2 mm/yr of pelagic and/or hemipelagic "sediment rain" sedimentation; and (2) ghost nodes (Fig. 4.2A) at the eastern boundary are uplifted each time step to prescribe a constant sediment flux of 40 m^2/yr, mimicking an off-model sediment source similar to the Mergui Ridge for the EAB.

The models are run for 10 m.y., where the first 5 m.y. represent the syn-tectonic stage with strike-slip motion and sedimentation to mimic the ~5 m.y. during which the ABCF was active. The final 5 m.y. constitute the post-tectonic stage with no prescribed motion or sediment supply, although sediment transport continues (for setup details, see Text C.4).

4.4 Reference model results

In the reference model, strain localizes on a vertical fault near the model center (at ~0.5 m.y.; Fig. 4.2C). Both sides of the fault subside due to the influx of sediment, with the eastern side

sinking faster (1.0 versus 0.4 mm/yr at 4.75 m.y.). By 5 m.y., the eastern side has subsided more than the western side (3.6 versus 1.0 km), rotating the strike-slip fault to subvertical. After strike-slip motion and sedimentation have ceased, the subsidence rate declines to 0.08 mm/yr as the sediment hill at the eastern boundary is distributed across the surface. By 10 m.y., both sides have subsided another 0.4 km, showing a synformal thickening geometry along the fault.

The model indicates that a flexural strike-slip basin emerges due to sedimentation above thin lithosphere close to a strike-slip fault, wherein the fault acts as a weak zone where subsidence focuses. In contrast to classical half-graben or pull-apart geometries, these basins form without a significant extensional component (i.e., without crustal thinning as seen in pull-apart basins).

4.5 Controls on flexural strike-slip basin formation

To test controls on flexural strike-slip basin formation, we ran a series of models varying in sedimentation rate, lithospheric thickness, and fault strength. Sedimentation rate was changed by altering the eastern-side influx from 0 (i.e., only sediment rain) to 60 m^2/yr (Figs. 4.3A–D). With no lateral input, both sides subsided evenly, forming a synformal basin that is thickest at the fault (Fig. 4.3A). This suggests that reference-model basin asymmetry is affected primarily by sedimentation and not by the initial perturbation. At higher lateral input, the eastern side subsided more, from a maximum basement deflection of 0.9 km with no input to 5.7 km for 60 m^2/yr of input (Fig. 4.3D). The western side shows a less-pronounced deflection with higher sediment input (0.8–1.6 km), suggesting either that the sides are not fully decoupled or that more sediment reached the western side.

The effects of varying the lithospheric thickness from 60 to 30 km (Figs. 4.3E–H) reduce the basement flexural deflection on the eastern side of the fault from 4.6 km at 30 km to 1.4 km at 60 km, suggesting that deep flexural basins are unlikely to form in regions with thick lithosphere.

The final key variable is friction-angle weakening (Figs. 4.3I–L). This shows that fault strength affects flexural subsidence (4.2 versus 3.3 km deflection at 99% and 25% weakening, respectively), suggesting that regions with no weakening or without strike-slip motion (Fig. C.3) would experience much less subsidence. Further, weak faults promote lithospheric decoupling and basin asymmetry related to asymmetric sedimentation.

4.6 Flexural strike-slip basins in the Andaman Sea

Seismic data suggest that the EAB is an asymmetric basin that spans both sides of the ABCF (Mahattanachai et al., 2021). On the western side, basin thickness is fairly uniform (1–2 km; Fig. 4.1D). Along the fault on the eastern side, the basin is substantially thicker (~5 km) and thins eastward toward the sediment source areas of the Mergui Ridge and peninsular Thailand.

The Gulf of Moattama Basin formed along the active Sagaing fault and is a more ambiguous example where a deep (>10 km) depocenter formed in the past ~6 m.y., although strike-slip fault activity in the area probably dates to the Oligocene (Morley and Arboit, 2019). Although a gentle releasing-bend geometry is present in the offshore fault trace, the basin did not undergo dramatic subsidence until the latest Miocene–Pliocene, when a major transgression followed structural uplift and inversion of basins onshore (e.g., Morley and Alvey, 2015). We suggest

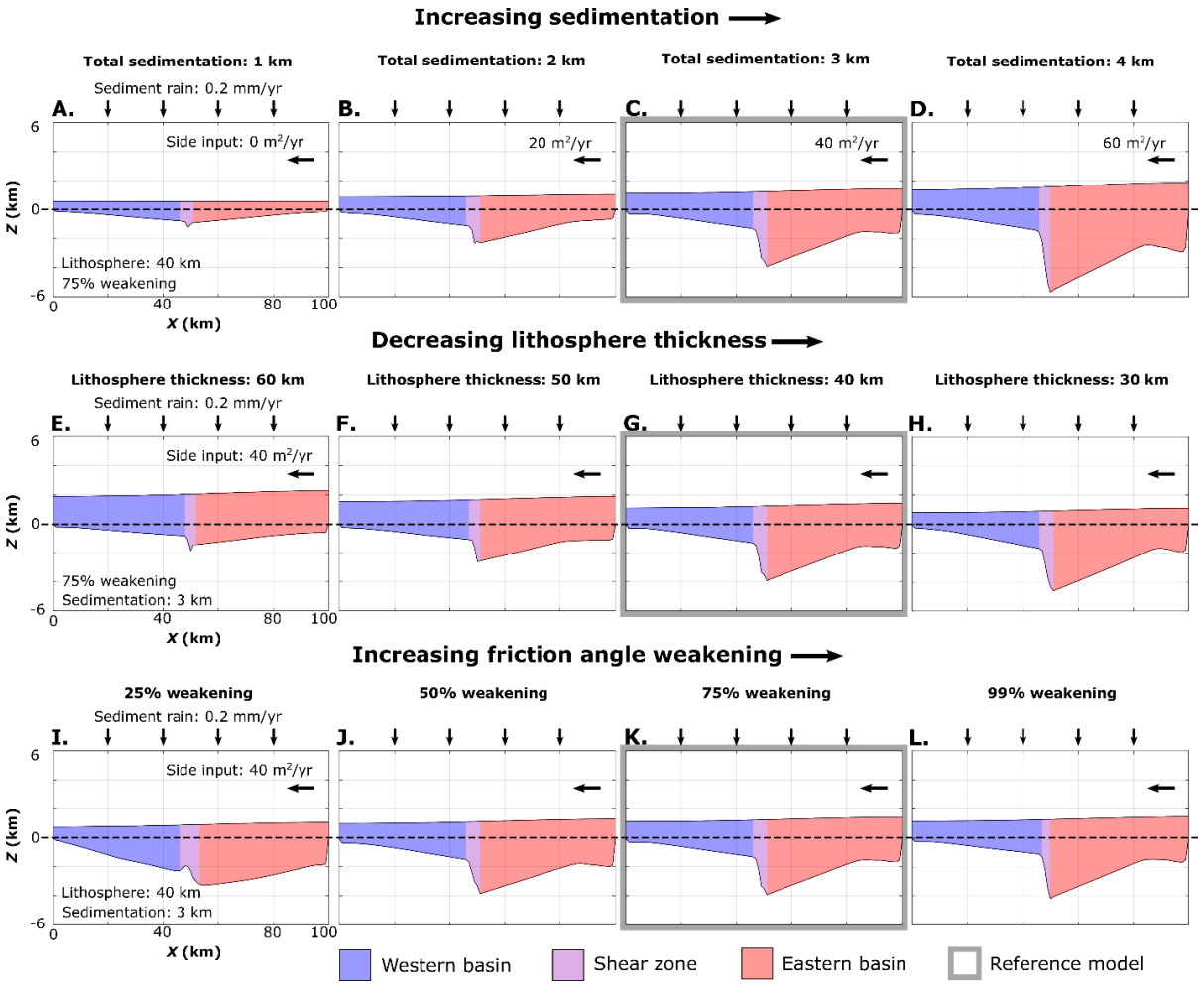

Figure 4.3 Modeled basin formation when subject to variable sediment input (A–D), lithosphere thickness (E–H), and fault weakening (I–L). Dashed lines along *Z* = 0 show initial model elevation. Total sedimentation is sediment thickness assuming an even distribution across the model.

the axial sediment influx along the Gulf of Moattama Basin resulted in the flexural strike-slip mechanism enhancing the effects of the fault geometry.

The primary requirement for flexural strike-slip basin formation is weak or thin lithosphere and high sedimentation rates. There are two basin types, controlled by the sedimentation pattern: (1) symmetric, where both sides receive a similar sediment load (Fig. 4.3A); and (2) asymmetric, where the two distinct basin sides subside at different rates dependent on the sediment load they receive (Fig. 4.3C). In both types, the maximum flexure and basin depocenter occur along the fault trace and the basin thins strike-perpendicularly.

The Andaman Sea provides likely examples for each flexural strike-slip basin type:

(1) The Gulf of Moattama Basin, where northern axial sedimentation provided even sedimentation to each side of the fault and formed a *symmetric flexural basin*. While sedimentation was not purely uniform, a synformal geometry developed centered along the fault zone, as in Figure 4.3A.

(2) The EAB (Fig. 4.1D), where perpendicular sedimentation from the east forced greater flexure on the eastern side of the fault, forming an *asymmetric flexural basin*. The EAB and reference model basin both have a change in sediment thickness across the fault and basin thinning toward the sediment source. Furthermore, basin thicknesses (excluding post-tectonic

sediment) along the fault's eastern side (4.5 versus 5.2 km in the model and EAB, respectively) and western side (1.8 versus 1.3 km) are comparable between the model and the basin.

Despite the similarities, there are discrepancies between the modeled basin and the EAB. Eastward thinning of the sediment layer is less pronounced in the model. Given that the basement slope is affected by the lithosphere thickness and sediment load, three possible explanations are:

(1) The ABCF is capped by a regional unconformity with the post-tectonic sediments (Srisuriyon and Morley, 2014; Morley, 2017), and the fault may have received more sediment while active than expected from the seismic data.

(2) Given that the fault formed within a necking zone and the lithosphere thickness is not well constrained, the lithosphere may have varied spatially (rheologically or in thickness) and been thinner than the 40 km value used here.

(3) A more significant syn-strike-slip extensional component would have further deepened the basin along the fault (Sobolev et al., 2005).

Also, our models do not consider basin translation with strike-slip motion. This is justified by comparison with the EAB, where the thicker eastern basin is located on the same side as the Mergui Ridge and is not affected by the translation. For the western basin, the ~350-km-long Mergui Ridge is longer than the total dextral strike-slip translation of ~90 km from the early to mid-Miocene.

We focused on the Andaman Sea, but the key requirements for flexural strike-slip basins—thin lithosphere, focused sedimentation, and a weak fault—are possibly also met in the New Guinea Basin in the Bismarck Sea (southwestern Pacific Ocean; Fig. C.4; Martinez and Taylor, 1996) and the Yinggehai Basin in the South China Sea (Fig. C.5; Clift and Sun, 2006), although new seismic data are needed to test this. Another candidate is the Navassa Basin in the Jamaica Passage (Caribbean Sea; Fig. C.6; Corbeau et al., 2016), an asymmetric strike-slip basin that is not located between offset segments. The basin likely formed during strike-slip motion and does not contain older sedimentary units found in nearby basins along the fault.

4.7 Conclusion

Our study suggests a new class of flexural basins that form along strike-slip faults. These basins are characterized by a fault-parallel depocenter and sediment that thins strike-perpendicularly. The basins can be classified in two types, which are both represented in the Andaman Sea: (1) *symmetric flexural basins*, where axial sedimentation causes a synformal shape, as seen in the Gulf of Moattama Basin; and (2) *asymmetric flexural basins*, where asymmetric sedimentation forces one basin side to subside more than the other, as seen in the EAB.

Flexural strike-slip basins form due to a strike-slip fault that acts as a weak zone facilitating differential subsidence due to sediment loading. The fault decouples the lithosphere sides, allowing them to respond independently to the sediment load they receive, determining basin symmetry. For a flexural strike-slip basin to form, two criteria must be met: the strike-slip fault must (1) cut through thin lithosphere, and (2) be subjected to a sufficient tectonic load.

4.8 Acknowledgments

This study was conducted within the Helmholtz Young Investigators Group CRYSTALS (grant VH-NG-1132). We thank the Computational Infrastructure for Geodynamics (https://geodynamics.org/), which is funded by the U.S. National Science Foundation under awards EAR-0949446 and EAR-1550901, for supporting the development of ASPECT code. The work was supported by the North-German Supercomputing Alliance (HLRN, https://www.hlrn.de/). Software and input files are found at http://doi.org/10.5281/zenodo.4893421. Figures were made using ParaView, InkScape, and GeoMapApp. We also thank Anthony Jourdon, Zhen Sun, and an anonymous reviewer for their helpful reviews.

Chapter 5 : Discussion

This thesis explores the evolution of plate boundaries with a focus on three topics: 1) The temporal evolution of rift fault networks in response to varying levels of surface processes efficiency, 2) the linkage of offset rift zones and the formation of continental microplates, and 3) the formation of a new type of flexural strike-slip basin due to surface processes along active strike-slip faults. The following sections connect these studies and discuss how spatio-temporal changes in the efficiency of may affect plate boundaries and their geological features on a large three-dimensional scale.

5.1 Rifts and surface processes

Chapter 2 investigates rift evolution in response to surface processes by quantitatively tracking faults and their properties through time. From this, three primary conclusions can be drawn:

1) The rift fault system evolves according to five distinct temporal phases (e,g, Fig. 2.3) that correlate to structural domains observed along rifted margins (Fig 2.10). These phases occur regardless of numerous factors such as the rift type (e.g., whether the rift is wide or narrow) and the efficiency of surface processes, supporting the hypothesis that structural domains can be widely applied to rifted margins (e.g., Chenin et al., 2021).

2) The formation of asymmetric rifted margins through rift migration occurs due to an exhumation zone (Brune et al., 2014) that includes low-angle slip along detachment faults (Fig. 2.9). Surface processes promote and extend this migration by enhancing crust hyperextension (Buiter, 2021).

3) The efficiency of surface processes in 2D rift models affects phase transitions (e.g., serpentinization is unlikely to occur with high surface processes efficiency), fault networks (e.g., low surface processes efficiency results in more complex faulting), and the timing of tectonic phases (e.g., continental breakup is delayed with greater surface processes efficiency) without changing the general evolution of the rift.

The third chapter looks into the broader evolution of rifts in 3D, investigating how offset rift segments connect and under what conditions structural features known as a continental microplates form. I find that rift linkage can be broadly attributed to four separated regimes: 1) oblique connection, 2) strike-slip connection, 3) microplate formation, and 4) no linkage (Fig 3.6). The linkage type for offset rift segments is influenced by the initial strike-perpendicular offset of the segments and the crustal strength (see also, Tentler and Acocella, 2010; Allken et al., 2012; Le Pourhiet et al., 2017), such that rifts connect by regime 1 at low offsets (<100 km) and don't connect (regime 4) with large offsets. The crustal strength influences how effectively faults accommodate extension, where stronger crusts result in more focused rifting and promote oblique or transform connections. From this, I find that intermediate offsets (>300 km) in weaker crustal setups promote rift overlap and the formation of continental microplates like the Flemish Cap (Fig. 3.8) and Sao Paulo Plateau (Fig. 3.9) seen along rifted margins.

Although *Chapter 3* does not include surface processes, I can use the findings from *Chapter 2* to speculate on potential effects of surface processes on rifting in 3D. In *Chapter 2* I find that

the erosional efficiency of surface processes increases the lifespan of individual faults which in turn reduces the fault network complexity, increases the likelihood of serpentinization, and delays continental breakup. Two main questions arise when trying to understand how a 3D system may respond to surface process: 1) How would loading and temperature changes related to erosion and the deposition of sediment impact an evolving offset 3D rift system? 2) How might spatial variability in the erosional efficiency along-strike of a rift influence the system?

For the first question, erosion and the deposition of sediment may promote or impede rift propagation and linkage. In *Chapter 3* I suggest that one of the key parameters in determining how offset rift segments link is the crustal strength because stronger crust helps to focus rift deformation (Fig 3.7). Loading of a fault's hanging wall promotes fault localization (Maniatis et al., 2009), suggesting that generally sedimentation should help focus deformation and increase the likelihood of oblique or transform rift linkage. However, changes to the geotherm from sediment deposition may also play a temporally changing role on the effective strength. Initially, the deposition of cold sediment will strengthen the crust and promote hard linkage. Over time sediment blanketing (Allen and Allen, 2013) will warm and weaken the crust promoting rift overlap. Because of these factors, not only the amount of sediment may influence 3D rift evolution, but also the sediment deposition time.

On the second question, the effects of surface processes on rift systems related to changes to the efficiency may become more important in 3D. *Chapter 2* varies the surface processes efficiency between models but assumes the efficiency and the resulting sediment load, and to a lesser extent the topographies, are homogeneous along-strike. As such, these models don't account for how a rift evolves along-strike if different portions of the rift receive different sediment loads. One of the primary influences of surface processes are that they delay continental breakup with increasing efficiency. Given variability along-strike of a rift, different portions of a rift may reach breakup significantly quicker than others. Additionally, the models in *Chapter 2* do not include the process of serpentinization but suggest it would occur in sediment-starved margins. As serpentinization may increase low-angle slip during rift migration (Reston and Pérez-Gussinyé, 2007; Lymer et al., 2019), this could further exaggerate the differences in rift evolution between regions with high or low surface processes efficiency. For 3D rift systems this change in rift migration mechanics and to the continental breakup timing along-strike of a rift because of surface processes may be important in how the overall system evolves.

An important factor to consider when speculating on the effects of surface processes in a 3D system is what may cause along-strike variations in the efficiency of surface processes, and how likely they are at the spatial scales used to investigate 3D rift systems and rift linkage. *Chapter 2* describes surface processes efficiency through the bedrock erodibility (K_f) which encompasses multiple different factors like the rock lithology and the climate (Whipple and Tucker, 1999). Rock lithology can vary at scales smaller or similar to those used to model 3D rift systems (e.g., features like batholiths or geologic provinces). Regional climates depend on nearby topographic features such as mountain ranges and bodies of water and can vary through time and spatially at scales of hundreds of kilometers (Beck et al., 2006), similar to those used to investigate rift linkage. Thus, it is possible that due to changes in the climate and rock lithology along-strike of a rift, different portions may be subjected to different efficiencies of erosion and deposition. Regions subjected to low efficiency will reach breakup significantly

quicker than those with greater efficiency, possibly altering the geometries of evolving rifts and linking rift segments.

The results of *Chapter 2* and *Chapter 3* suggest that while surface processes do not drastically change the overall rift evolution in 2D systems, their influence may become more significant in a three-dimensional context. Sediment loading and the related changes to the geotherm may initially promote rift linkage, but over time may instead promote rift overlap. Differences in the efficiency of surface processes because of changes to the rock lithology or climate along-strike of an evolving rift may change when certain segments of a rift reach continental breakup, possibly influencing how rifts propagate, evolve, and link. In the future it will be vital to explore fully three-dimensional model including surface processes and climate variability to investigate the spatial and temporal effects of surface processes on an evolving three-dimensional rift system.

5.2 Strike-slip plate boundaries and surface processes

Chapter 4 investigates how an active strike-slip fault responds to a sediment load from varying levels of sedimentation. The results suggest that a strike-slip fault acts as a weak zone that allows flexural subsidence given a sufficient tectonic load, and that sediments alone can generate enough force for flexure. The generated accommodation space promotes sediment deposition in the region, intensifying the effects and forming a flexural strike-slip basin. I find that the size and whether a basin forms depends on three factors: 1) the lithosphere thickness, 2) the sediment load, and 3) the weakness of the fault (Fig 4.3).

The Andaman Sea off-coast of Thailand provides likely examples of two flexural strike-slip basins: a basin that is symmetric across (strike-perpendicular) the strike-slip fault (Gulf of Moattama; Morley and Alvey, 2015; Morley and Arboit, 2019) and a basin that is asymmetric across the fault (East Andaman Basin, Fig 4.1; Mahattanachai et al., 2021). Observations suggest that the reason for the two types of basins relate to the orientation of the sediment supply relative to the strike-slip fault, with the Gulf of Moattama Basin primarily receiving sediments parallel to the fault, and the East Andaman Basin receiving sediments perpendicularly from the eastern side of the fault (Mahattanachai et al., 2021). The models here agree with this interpretation and suggest that a strike-slip fault allows each side of lithosphere to respond relatively independently based on the sediment load it receives.

The study presented in *Chapter 4* investigates strike-slip basin formation with an emphasis on variability in the orientation and size of the sediment supply, but another important factor to consider is strike-perpendicular variability in the lithospheric thickness. The East Andaman Basin is thought to have formed within a former rift necking zone (see Fig. 1.2a; Morley, 2017; Mahattanachai et al., 2021), which would suggest that the fault likely formed within the thinnest portion of the lithosphere, and the lithosphere thickens away from the fault. In *Chapter 4* I show that thinner lithosphere results in more subsidence from the same sediment load and a larger basin. However, given variable lithosphere thickness it may be important to determine whether the average thickness of the lithosphere, or the thickness near the fault is more important, as this may influence the resulting basin geometry.

Additionally, in the later stages of the models with large sediment loads, subsidence and faulting occurs near the model boundaries. If the lithosphere becomes thicker and stronger near

the domain borders, it may become less likely for faulting and subsidence to occur in these areas and may focus even greater subsidence near the strike-slip fault. Thus, depending on how strike-perpendicular variation in lithosphere thickness affect strike-slip flexure, it has the potential to either inhibit or promote flexural strike-slip basin formation and needs to be further investigated.

The models presented in *Chapter 4* are three-dimensional but thin enough (8 km) that along-strike variations do not develop. In nature, strike-slip faults vary along-strike and can consist of multiple offset segments. While the East Andaman Basin is a laterally extensive feature (Mahattanachai et al., 2021), suggesting that the results should apply in larger model domains that include such variations, I do not include or investigate how additional structures commonly associated with strike-slip boundaries respond to variations in surface processes. Two common geological structures that would be interesting to investigate in a context with surface processes are 1) compressional flower structures that form at restraining bends between offset segments (McClay and Bonora, 2001), and 2) extensional pull-apart structures that form at releasing bends between offset segments (Mann et al., 1983). As we find that faults in rift zones and interacting segments are influenced by the crustal strength, which in turn is affected by erosion and sediment deposition, the inclusion of surface processes in large strike-slip models may affect segment interaction and the resulting geological structures. For example, greater crustal strength is shown to promote the connection of rift segments (*Chapter 3)*. If this occurs similarly in strike-slip segments, offset segments may connect earlier with greater surface processes efficiency, which could effectively end a pull-apart basin (van Wijk et al., 2017). Further investigating how strike-slip faults respond to erosion and deposition, and how this affects the larger scale interaction between offset strike-slip segments and their features will be important in understanding how strike-slip boundaries evolve through time.

Chapter 6 : Conclusions

In this thesis I aimed to explore two primary questions: 1) How do divergent and strike-slip plate boundaries evolve? 2) How is this evolution affected by erosion and deposition?

1a) In two-dimensional models, the fault system of a rift evolves according to five separate phases: phase 1) distributed deformation and coalescence, phase 2) fault system growth, phase 3) fault system decline and basinward localization, phase 4) rift migration, and phase 5) continental breakup (Fig 2.3). These phases are seen regardless of the rift type (e.g., wide, symmetric, or asymmetric) and efficiency of surface processes, and correlate well to structural domains (Fig 2.10) seen in seismic data along rifted margins (e.g., Lymer et al., 2019).

1b) In large three-dimensional models, rift zones at divergent boundaries interact and connect depending on two primary factors: the strike-perpendicular offset and the crustal strength. The segments propagate forward and connect through either regime 1) an oblique segment, 2) a strike-slip segment, 3) by overlapping and rotating the central region between the segments before an eventual rift jump connects them, or 4) no linkage occurs (Fig 3.6). By increasing the strike-perpendicular offset, the rifts propagate farther forward before interacting enough to connect, causing them to link at higher angles until eventually the rifts are far enough apart that they overlap before connecting. As such, by increasing the strike-perpendicular offset the connection type switches from regime 1) to 4). The crustal strength influences how well deformation localizes in the rifts; stronger crust promotes this localization and causes rift segments to interact more strongly at a given offset. Conversely, weak crust reduces rift segment interaction and promotes forward propagation, increasing the angle of the linking segment given the same strike-perpendicular offset. In essence, crustal strength affects the offset range at which each rift linkage type occurs, where with weak crust smaller offsets are needed for rift overlap.

The type of rift connection affects the structural features seen along rifted margins. An oblique segment would leave an oblique margin, a strike-slip segment may form large fracture zones like those seen in the Atlantic (e.g., Florianopolis Fracture Zone; Fromm et al., 2015). When the rift segments overlap and rotate the central region, they create an active continental microplate similar to the Victoria Microplate in the East African Rift System (Glerum et al., 2020). Eventually, through the connection of the segments, the microplate stops rotating and becomes attached to one side of the rift margin, leaving behind features like the Flemish Cap (Fig. 3.8; Welford et al., 2012) or Sao Paulo Plateau (Fig. 3.9; Scotchman et al., 2010).

1c) Along strike-slip boundaries, a large sediment load can force flexure and subsidence forming a new type of feature as seen in the Andaman Sea (East Andaman Basin; Mahattanachai et al., 2021): the flexural strike-slip basin (Fig 4.1). The geometry and size of this basin depends on the orientation of sedimentation, amount of sediment, lithosphere thickness, and weakness of the strike-slip fault. A weak strike-slip fault is needed to act as a weak zone for tectonic related subsidence to focus, and the weaker the fault the greater the amount of subsidence. The lithosphere thickness and sediment load impact the total basin thickness, where a larger sediment load promotes subsidence, and a thicker lithosphere impedes subsidence such that a relatively thin lithosphere is needed for a basin to form. The orientation of sedimentation influences basin symmetry. A sediment supply parallel to the fault will

relatively uniformly distribute sediment on both sides of the fault causing symmetric subsidence across the fault. On the other hand, if sediment input is dominantly from one side like in the East Andaman Basin, the fault works to decouple the two sides of lithosphere and each subsides based on the sediment it receives. This asymmetry is more pronounced given a weaker fault.

2a) Based on the 2D divergent models in *Chapter 2*, erosion and deposition influence fault properties and lengthen the different phases a rift progresses through (Fig. 2.4). Generally, greater surface processes efficiency increases the lifespan of a fault (e.g., Andrés-Martínez et al., 2019). This results in less frequent fault formation, and affects the number, length, and displacement of active faults in the fault network. During the evolution of a rift, the fault network progresses through the five phases described previously in point 1a). The addition of surface processes causes both phases 2 and 4 to last longer, as such the overall effect of increasing surface processes efficiency on rift evolution is to delay continental breakup.

2b) The efficiency of surface processes is impacted by rock lithology and the climate (Whipple and Tucker, 1999), both of which vary on scales relevant to an evolving 3D rift system. This could lead to along-strike variability in the sediment supply, which may temporally influence how well deformation localizes in a rift impacting how rifts propagate and link. Changes to the surface processes efficiency along-strike would also affect the rate at which different portions of a rift progress through the five fault-system phases towards continental breakup, possibly influencing the overall geometry of the rifted margin.

2c) Surface processes also influence the structures that form at plate boundaries. At divergent boundaries, greater surface processes efficiency results in fewer faults and less complex margin architecture. The particular mechanisms active during rifting are also affected by surface processes, for example the process of serpentinization during rift migration is only likely to occur in sediment-starved margins (Fig. 2.9). By coupling tectonic models to surface processes, models can generate sedimentary basins and unconformities to compare to geological structures such as rift and sag basins, rift unconformities, and angular unconformities along divergent boundaries (Fig 2.2), and flexural strike-slip basins along strike-slip boundaries (Fig 4.1).

A. Supplementary material for Chapter 2

Summary

In this supplementary material, we provide 3 tables detailing the parameters for setting up the ASPECT model (Table A.1), FastScape model (Table A.2), and for the different phase timings (Table A.3). We include 7 figures that compare the x-extension held on the tracked fault system along a depth contour to the extension prescribed as a boundary condition (Fig. A.1), the amount of fault slip held on active faults vs. the entire fault system, as well as information on how the graphs were processed (Fig. A.2), and comparisons on the number of faults in the system over time for different models (Fig. A.3, A.4, A.5, and A.7).

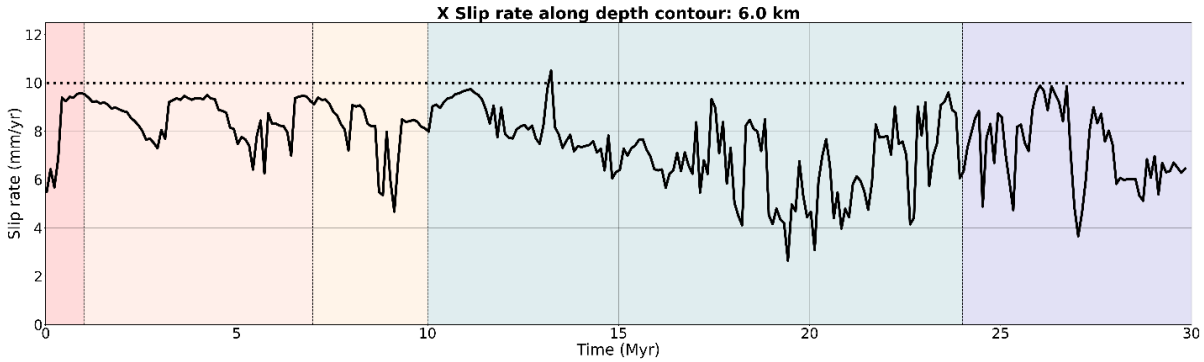

Figure A.1 Figure comparing extension held on the tracked fault system vs. the amount of extension prescribed by the boundary conditions. The dashed line at 10 mm/yr represents the extension prescribed at the model boundaries. The solid black line shows the cumulative extension (X slip rate) of all faults along the 6 km depth contour. In an idealized model where all deformation is accommodated by major faults, both lines should coincide. Practically, however, there is a varying degree of deformation that is accommodated within fault blocks and in small faults that are not accounted for by the analysis. This comparison illustrates that deformation is localized on major faults during phase 2 and 3, while the other phases involve a larger degree of off-fault deformation.

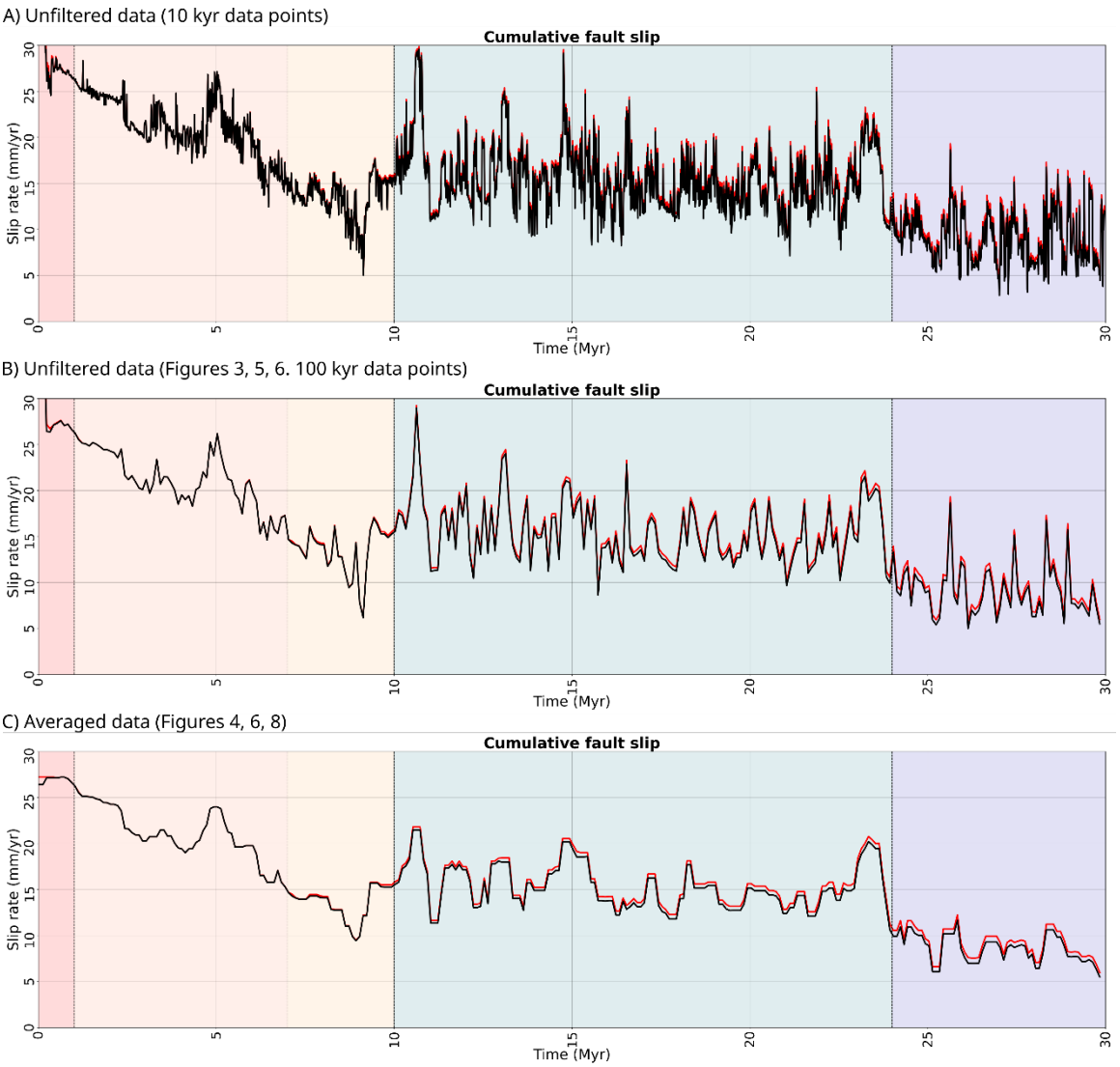

Figure A.2 Comparison between the cumulative total slip held by all tracked faults (red) vs. the cumulative total slip held by the active faults (black). When plotting the fault property evolution in a time series the values may change rapidly because of our approach to employ thresholds on fault size and plastic strain. To reduce the noise and increase graph readability, the graphs are post-processed in a way that does not affect the presented results. First, all graphs are plotted at 100 kyr intervals. Second, when plotting active fault properties, for a fault to be considered active it had to be active the previous timestep (10 kyr earlier) as well as the current timestep. To showcase how our processing affects the results: A) Plotting every 10 kyr data point available. B) Plotting data every 100 kyr, such as in figures 2.3, 2.5, 2.7, and A.1. C) Averaging the 100 kyr points from B over 5 points (500 kyr), such as in figures 2.4, 2.6, 2.8, A.3, A.4, A.5, and A.6.

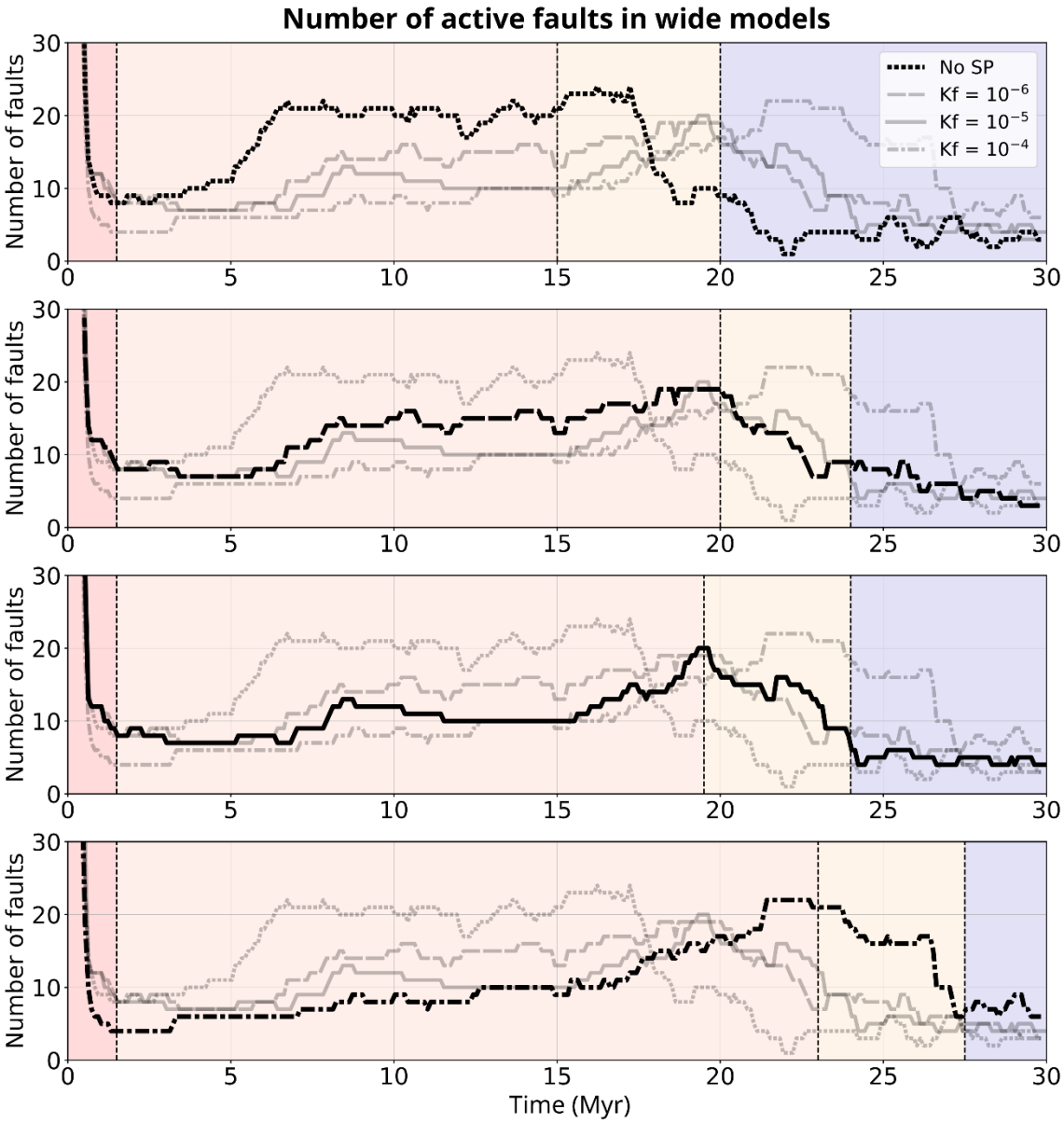

Figure A.3 Number of active faults in wide rift models with varying levels of sedimentation. Phases are indicated by colors, with phase 1 (red), phase 2 (orange), phase 3 (yellow), and phase 5 (purple).

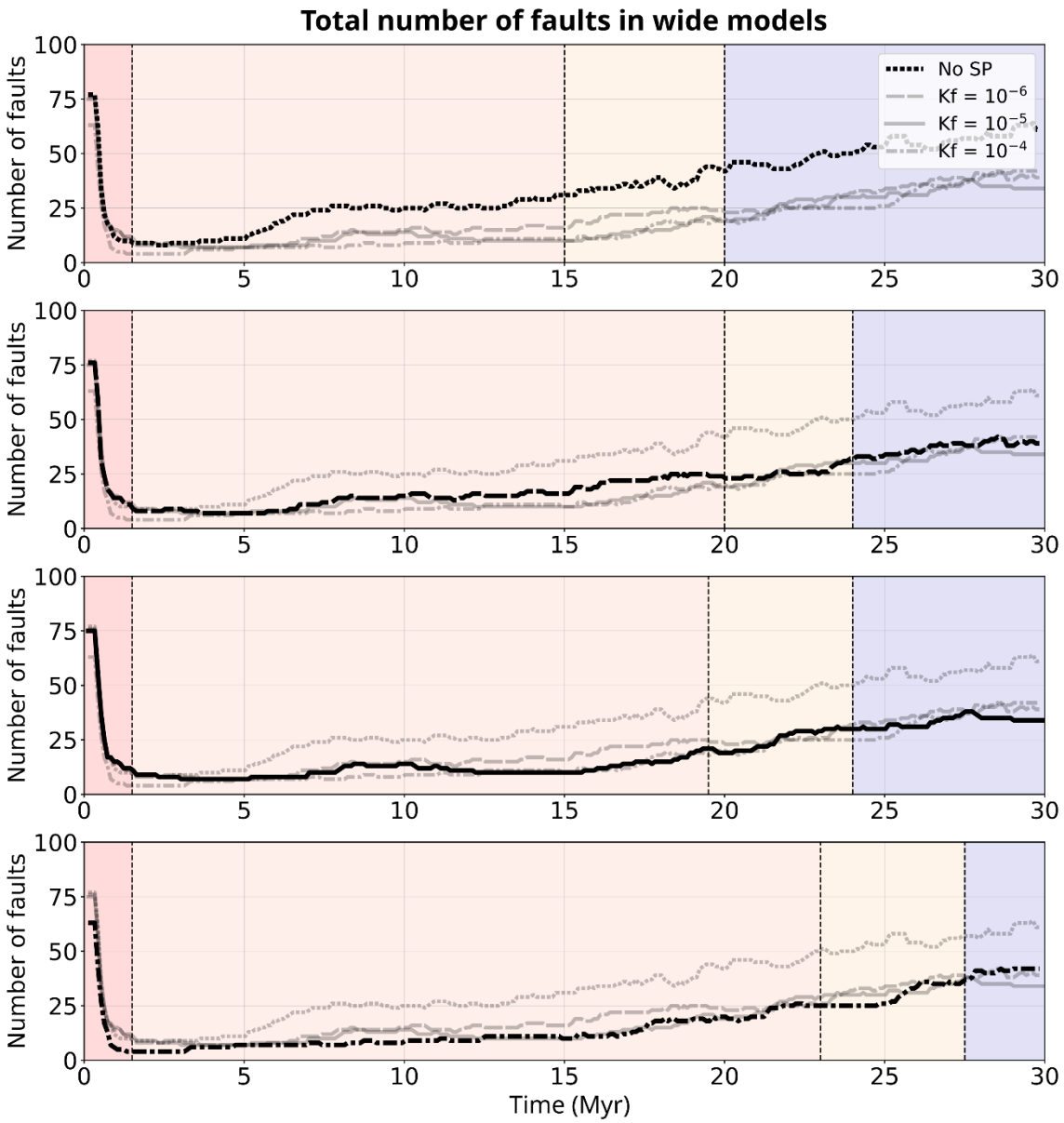

Figure A.4 Total number of faults in wide rift models with varying levels of sedimentation. Includes active and inactive faults. Phases are indicated by colors, with phase 1 (red), phase 2 (orange), phase 3 (yellow), and phase 5 (purple).

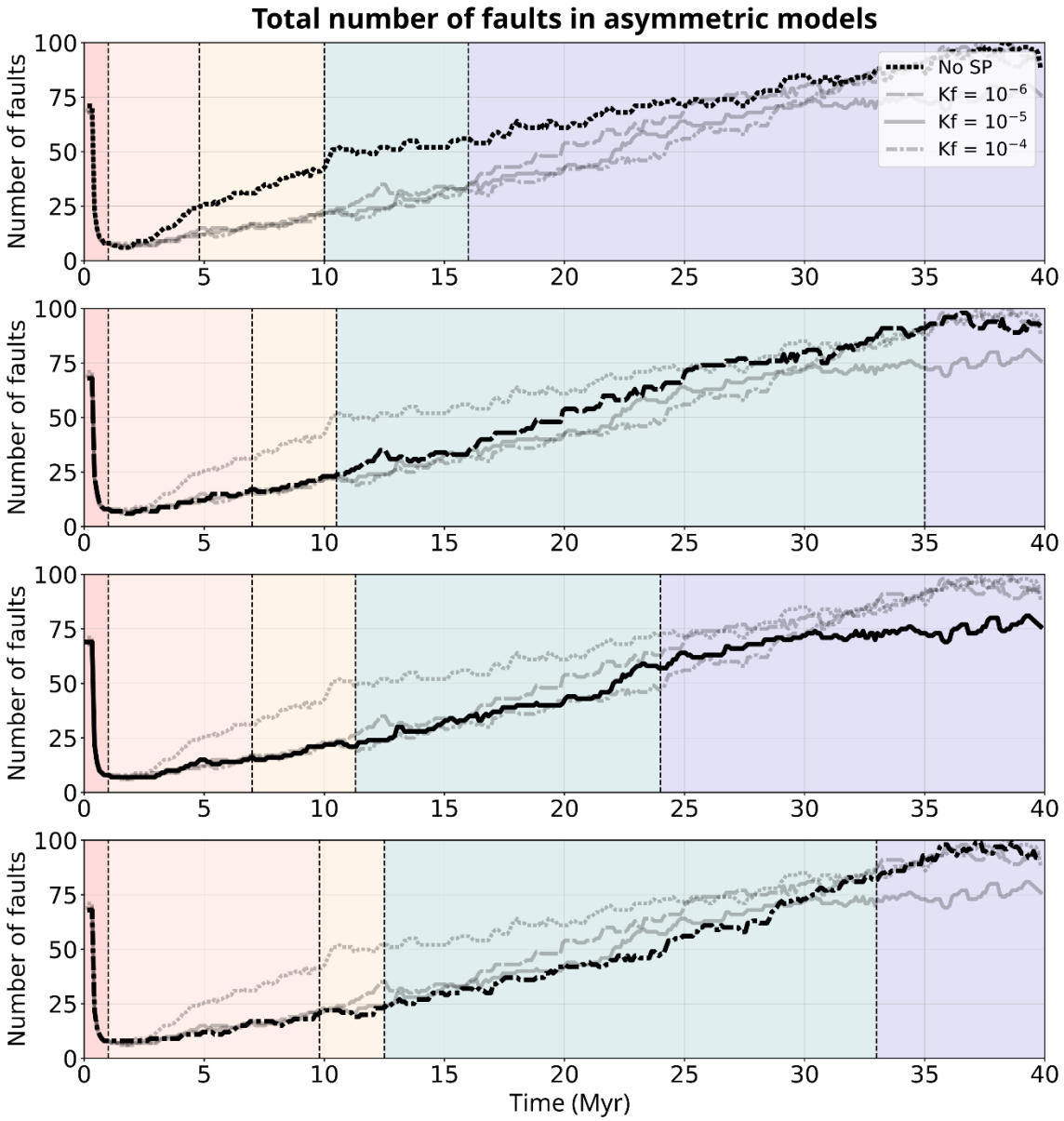

Figure A.5 Total number of faults in asymmetric rift models with varying levels of sedimentation. Includes active and inactive faults. Phases are indicated by colors, with phase 1 (red), phase 2 (orange), phase 3 (yellow), and phase 5 (purple).

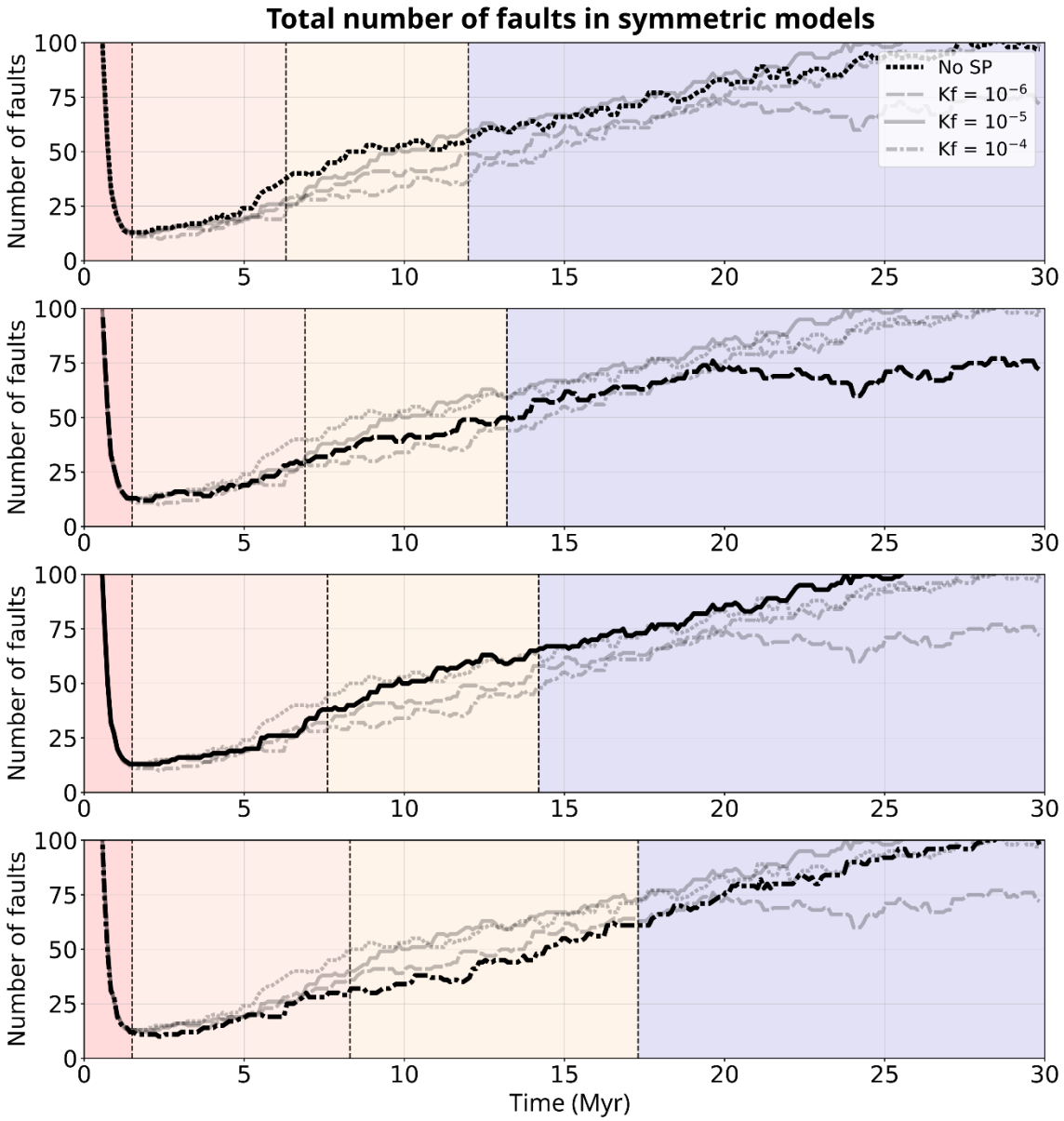

Figure A.6 Total number of faults in symmetric rift models with varying levels of sedimentation. Includes active and inactive faults. Phases are indicated by colors, with phase 1 (red), phase 2 (orange), phase 3 (yellow), phase 4 (green) and phase 5 (purple).

Parameter	Symbol	Units	Sediment	Upper crust	Lower crust	Lithospheric mantle	Asthenosphere
Reference surface density*	ρ_0	kgm^{-3}	2520	2700	2850	3280	3300
Thermal expansivity	α	K^{-1}	$3.7 \cdot 10^{-5}$	$2.7 \cdot 10^{-5}$	$2.7 \cdot 10^{-5}$	$3.0 \cdot 10^{-5}$	$3.0 \cdot 10^{-5}$
Thermal diffusivity	κ	$m^2 s^{-1}$	$7.28 \cdot 10^{-7}$	$7.72 \cdot 10^{-7}$	$7.31 \cdot 10^{-7}$	$8.38 \cdot 10^{-7}$	$8.33 \cdot 10^{-7}$
Heat capacity	C_p	$J\ kg^{-1}\ K^{-1}$	1200	1200	1200	1200	1200
Heat production	H	$W\ m^{-3}$	$1.2 \cdot 10^{-6}$	$1.0 \cdot 10^{-6}$	$0.1 \cdot 10^{-6}$	0	0
Cohesion	C	Pa	$5 \cdot 10^6$	$5 \cdot 10^6$	$5 \cdot 10^6$	$5 \cdot 10^6$	$5 \cdot 10^6$
Internal friction angle (unweakened)	ϕ	◦	26.56	26.56	26.56	26.56	26.56
Plastic strain weakening interval	-	-	[0,1]	[0,1]	[0,1]	[0,1]	[0,1]
Plastic strain weakening factor	ϕ_{wf}	-	0.25	0.25	0.25	0.25	0.25
Viscous strain weakening interval	-	-	[0,1]	[0,1]	[0,1]	[0,1]	[0,1]
Viscous strain weakening factor	-	-	0.25	0.25	0.25	0.25	1.0
Creep properties			*Wet quartzite*	*Wet quartzite*	*Wet anorthite*	*Dry olivine*	*Wet olivine*
Stress exponent (dis)	n	-	4.0	4.0	3.0	3.5	3.5
Constant prefactor (dis)	A_{dis}	$Pa^{-n}s^{-1}$	$8.57 \cdot 10^{-28}$	$8.57 \cdot 10^{-28}$	$7.13 \cdot 10^{-18}$	$6.52 \cdot 10^{-16}$	$2.12 \cdot 10^{-15}$
Activation energy (dis)	E_{dis}	$Jmol^{-1}$	$223 \cdot 10^3$	$223 \cdot 10^3$	$345 \cdot 10^3$	$530 \cdot 10^3$	$480 \cdot 10^3$
Activation volume (dis)	V_{dis}	$m^3\ mol^{-1}$	0	0	$38 \cdot 10^{-6}$	$18 \cdot 10^{-6}$	$11 \cdot 10^{-6}$
Constant prefactor (diff)	A_{diff}	$Pa^{-1}s^{-1}$	$5.79 \cdot 10^{-19}$	$5.79 \cdot 10^{-19}$	$2.99 \cdot 10^{-25}$	$2.25 \cdot 10^{-9}$	$1.5 \cdot 10^{-9}$
Activation energy (diff)	E_{diff}	$Jmol^{-1}$	$223 \cdot 10^3$	$223 \cdot 10^3$	$159 \cdot 10^3$	$375 \cdot 10^3$	$335 \cdot 10^3$
Activation volume (diff)	V_{diff}	$m^3\ mol^{-1}$	0	0	$38 \cdot 10^{-6}$	$6 \cdot 10^{-6}$	$4 \cdot 10^{-6}$
Grain size (diff)	d	m	0.001	0.001	0.001	0.001	0.001
Grain size exponent (diff)	m	-	2.0	2.0	3.0	0	0

Table A.1 Reference parameter values. dis – dislocation creep. diff – diffusion creep. *Model input densities are scaled so that at surface temperatures (273 K) these values are reached.

Parameter	Symbol	Unit	Value		
Drainage area exponent	m	-	0.4		
Slope exponent	n	-	1		
Bedrock/sediment diffusivity	K_c	m^2/yr	$5 \cdot 10^{-3}$		
Bedrock/sediment erodibility	K_f	$m^{0.2}/yr$	$1 \cdot 10^{-4}$, $1 \cdot 10^{-5}$, or $1 \cdot 10^{-6}$		
Bedrock/sediment deposition coefficient	G	-	1		
Marine diffusivity	K_m	m^2/yr	200		
Sand/shale ratio	F	-	1		
Sand/shale porosity	φ	-	0		
Sand/shale e-folding depth	z	m	0		
Depth averaging thickness	L	m	100		
Sediment rain	-	m/yr	<10 Myr	<20 Myr	Until model end
			$1 \cdot 10^{-4}$	$5 \cdot 10^{-5}$	0

Table A.2 Landscape evolution model parameters.

Model type	**Kf ($m^{0.2} yr^{-1}$)**	**Phase 1**	**Phase 2**		**Phase 3**		**Phase 4**		**Phase 5**
		start	start	duration (myr)	start	duration (myr)	start	duration (myr)	start
Asymmetric	0	0	<1	4	5	5	10	6	16
Asymmetric	1e-6	0	<1	6	7	4	11	24	35
Asymmetric	1e-5	0	<1	6	7	4	11	13	24
Asymmetric	1e-4	0	<1	9	10	3	13	20	33
Symmetric	0	0	<2	4	6	5	n/a		11
Symmetric	1e-6	0	<2	5	7	6	n/a		13
Symmetric	1e-5	0	<2	6	8	6	n/a		14
Symmetric	1e-4	0	<2	6	8	10	n/a		18
Wide	0	0	<1	13	15	5	n/a		20
Wide	1e-6	0	<1	18	20	4	n/a		24
Wide	1e-5	0	<1	18	20	4	n/a		24
Wide	1e-4	0	<1	22	23	8	n/a		28

Table A.3 Table showing the phase timings for all models. The start subcolumn indicates the model time that a phase started at.

B. Supplementary material for Chapter 3

Summary

In this supplementary material, we provide a table detailing model parameters, as well as animations showcasing the evolution of the 1) oblique linkage (*Regime 1*, movie B.1), 2) transform linkage (*Regime 2*, movie B.2), 3) microplate formation (*Regime 3*, movie B.3), and rift jump without microplate (*Regime 4*, movie B.4) reference model evolutions discussed in the paper. We include 4 additional figures including an initial density profile (Fig. B.1), a larger model domain (900x900 km, Fig. B.2), and a regime diagram for varied lithosphere thickness and X-offset (Fig. B.3). Additionally, we include two models with a mantle plume where we vary the plume placement from the left to right side of the model. In the text we describe the model setup shown in Fig. B.4 and briefly cover the evolution of these models. Two additional animations showcase the evolution of these models (movies S5 and S6). All models were run using dealii version 9.1.1, and the ASPECT version with all model parameter files is found here: https://doi.org/10.5281/zenodo.4601188.

Text B.1.

To test the effects the arrival of a mantle plume has on microplate development, we setup a model similar to the reference microplate setup with an X- and Y- offset of 300 km, and a crustal strength ratio of 25 km upper crust to 10 km lower crust. The model depth is extended to 360 km and we place the plume center at 600 km in the X-direction and 300 km in the Y-direction. The plume is prescribed as a Gaussian function on the bottom boundary, where a maximum velocity (0.4 m/yr), temperature anomaly (300 K), and radius (200 km) determine the size, inflow, and temperature of the plume (Figure B.1). The plume arrives in two phases: from 10-15 Myr plume inflow uses the above-mentioned parameters (plume head phase), with a volume flux of ~350 m^3/s. From 15 Myr until the end of the model run, the maximum velocity, temperature anomaly, and radius are halved to mimic the plume stem, which in this case has a volume flux of 43 m^3/s. The remainder of the bottom boundary is prescribed an inflow or outflow to conserve mass. To determine this value, we integrate the total inflow from the plume and subtract from this the outflow related to the side boundaries. Everywhere outside of the plume is given a velocity to balance the left-over flow.

In the first 10 Myr, both rift arms propagate into undeformed crust and curve inward where overlap occurs (supplementary video B.5). This is followed by localization into the center of the rift valleys, leading to both rift arms having a ~225 km long orthogonal fault section with no overlap between the rifts, and ~170 km oblique sections with overlap. The plume head starts to rise through the model at 10 Myr and by 10.5 Myr has impinged on the lithosphere underneath the eastern rift arm. Plume material spreads to both sides, reaching the model boundary on the eastern side, and forming a channel of warm material flowing to the western rift on the other side. Both rifts migrate towards the boundaries. However, while the western rift has relatively symmetric spreading, the eastern rift migrates asymmetrically at a faster rate, leaving a thinned continental margin attached to the microplate. By 15 Myr, seafloor spreading has started at the northern boundary on the eastern rift. As asymmetric rift migration continues, the obliquity of the eastern rift's overlapping segment increases from ~45°at 15 Myr to ~60°

at 21 Myr. Simultaneously, the center of rotation of the microplate migrates to the southwest until 21 Myr, at which time the eastern rift attaches to the southern boundary, and the western rift subsequently dies out.

To test the effect of plume position on model evolution, we ran a separate simulation initially placing the plume on the western side at 300 km in the X- and 300 km in the Y-direction (supplementary video B.6). The model evolves similarly to the one with the eastern plume location, with the plume impinging and beginning to spread underneath the lithosphere by 10.5 Myr. In this case, plume material is more localized in the western rift, and extension occurs at a faster rate compared to the eastern rift. As extension continues, the western rift propagates across the model domain faster, but remains relatively orthogonal while the eastern rift increases in obliquity. The center of rotation migrates to the northeast until ~23.5 Myr, when the western rift attaches to the northern model boundary, causing the microplate to attach to the eastern side. The eastern rift completely dies out by 24.5 Myr. Although the evolution remains similar, model plume placement is therefore an important factor in determining which rift takes over, and the side the microplate attaches to.

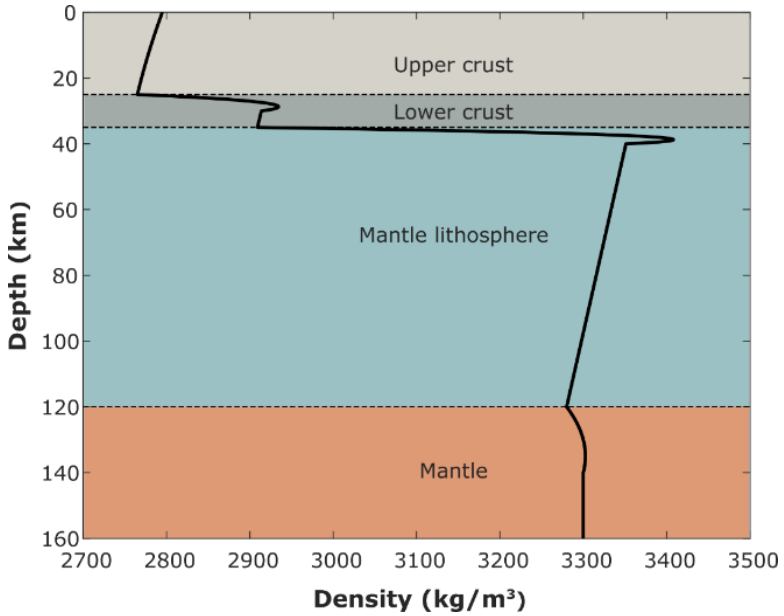

Figure B.1 Initial density profile where colors indicate composition.

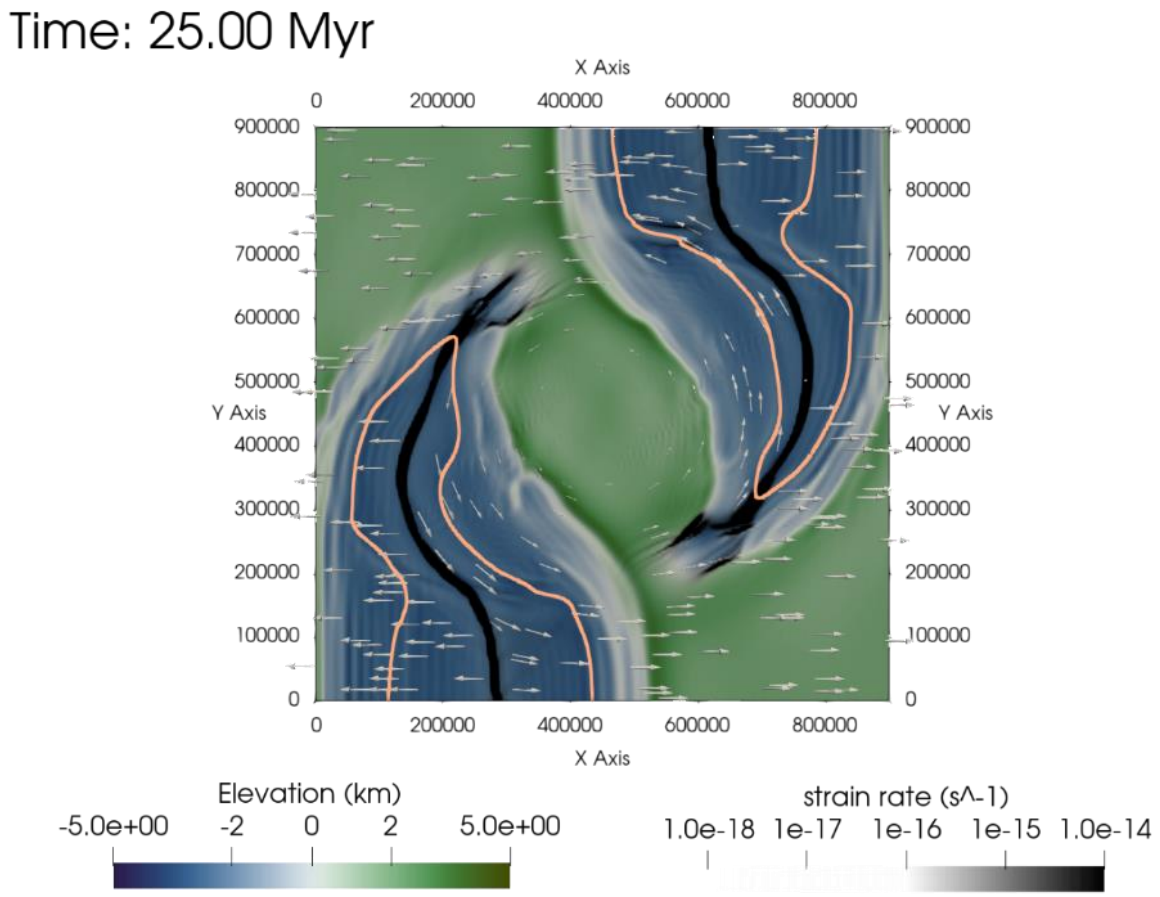

Figure B.2 Example of larger 900x900 (X and Y) microplate model which was given an initial X-offset of 400 km, Y-offset of 300 km, crustal ratio of 25:10, and lithosphere thickness of 120 km (i.e. similar to models of Fig. 3.5 and 3.6h, but in a larger model domain). Orange line indicates the landward limit of oceanic crust.

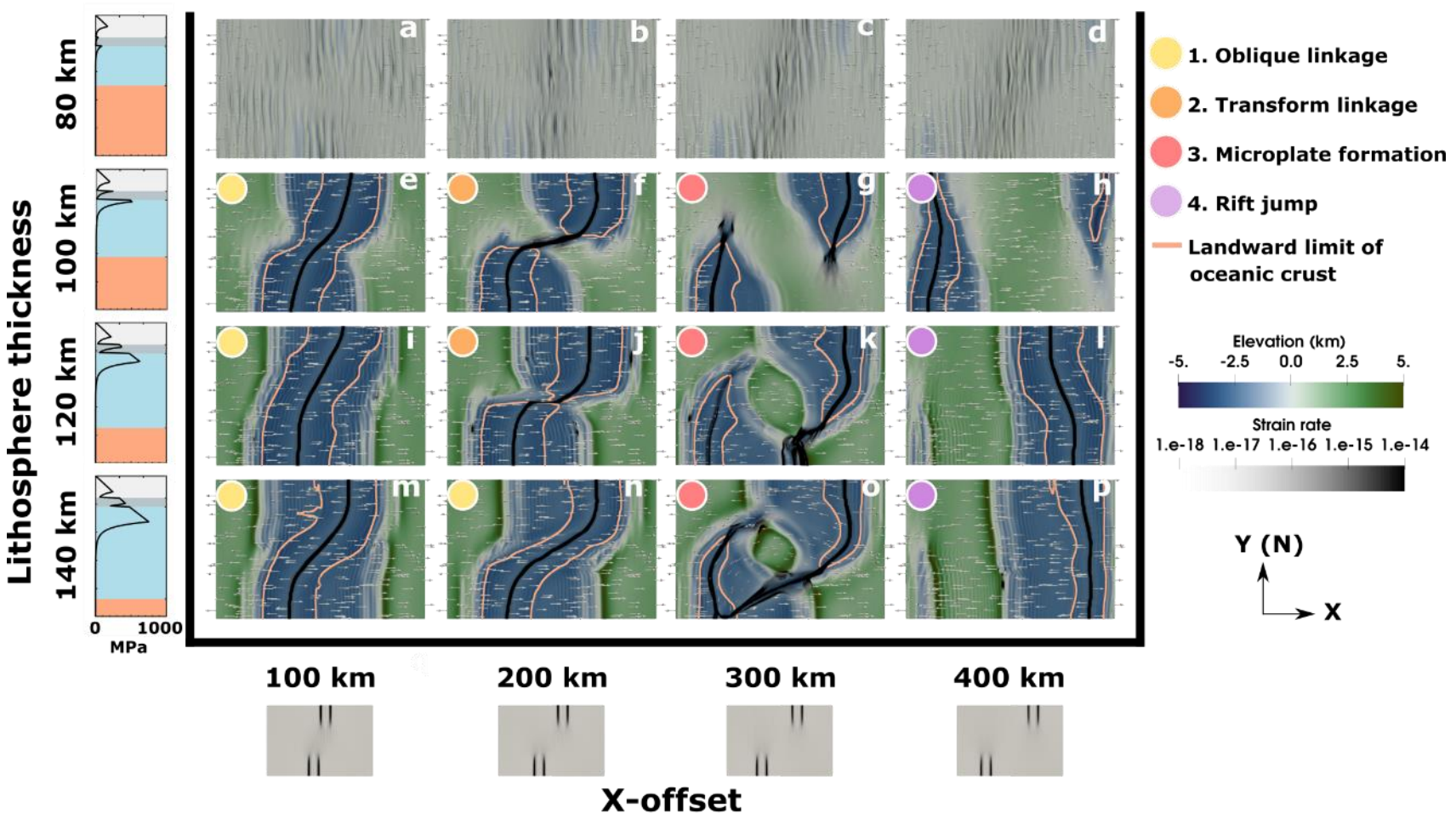

Figure B.3 Regime diagram showing the types of rift connections when varying the lithosphere thickness, and the initial x- offset. Models are shown from a top down view at 25 Myr, and are colored by elevation and the strain rate, with the orange line representing the landward limit of oceanic crust (>70% asthenosphere material). On the left, strength envelopes are shown, with the compositions of upper (light gray) and lower (dark gray) crust, mantle lithosphere (blue), and mantle (orange). Models are divided into regimes shown with colored dots in the top-left corners of the model images.

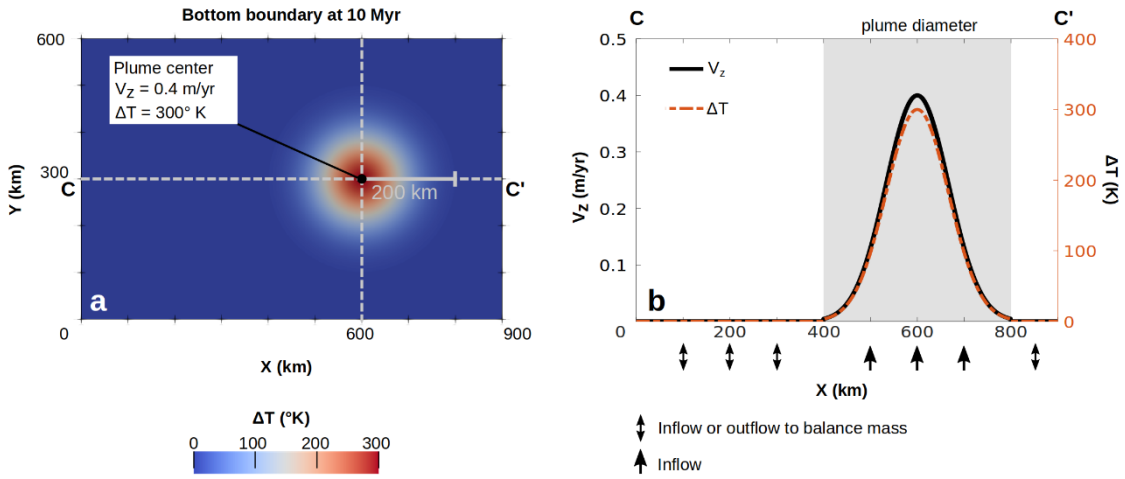

Figure B.4 Setup for the rift model including a mantle plume. The setup shows the initial state of the plume head phase, which runs from 10 to 15 My. a) Top view of bottom boundary excess temperature ΔT at 10 Myr when the plume is initially emplaced. b) Plume excess temperature ΔT (dashed red line) and the Z component of velocity V_z(black line) along the transect CC' in a. The gray box shades the area within the plume radius.

Parameter	Symbol	Units	Upper crust	Lower crust	Lithospheric mantle	Asthenosphere
Reference density	ρ_0	kg m^{-3}	2700	2850	3280	3300
Thermal expansivity	α	K^{-1}	$2.7\cdot10^{-5}$	$2.7\cdot10^{-5}$	$3.0\cdot10^{-5}$	$3.0\cdot10^{-5}$
Thermal diffusivity	κ	m^2 s^{-1}	$7.72\cdot10^{-7}$	$7.31\cdot10^{-7}$	$8.38\cdot10^{-7}$	$8.33\cdot10^{-7}$
Heat capacity	C_p	J kg^{-1} K^{-1}	1200	1200	1200	1200
Heat production	H	W m^{-3}	$0.7\cdot10^{-6}$	$0.2\cdot10^{-6}$	0	0
Cohesion	C	Pa	$5\cdot10^6$	$5\cdot10^6$	$5\cdot10^6$	$5\cdot10^6$
Internal friction angle (unweakened)	ϕ	◦	26.56	26.56	26.56	26.56
Strain weakening interval	-	-	[0,1]	[0,1]	[0,1]	[0,1]
Strain weakening factor	ϕ_{wf}	-	0.1	0.1	0.1	0.1
Creep properties			***Wet quartzite***	***Wet anorthite***	***Dry olivine***	***Dry olivine***
Stress exponent (dis)	n	-	4.0	3.0	3.5	3.5
Constant prefactor (dis)	A_{dis}	Pa^{-n} s^{-1}	$8.57\cdot10^{-28}$	$7.13\cdot10^{-18}$	$6.52\cdot10^{-16}$	$6.52\cdot10^{-16}$
Activation energy (dis)	E_{dis}	J mol^{-1}	$223\cdot10^3$	$345\cdot10^3$	$530\cdot10^3$	$530\cdot10^3$
Activation volume (dis)	V_{dis}	m^3 mol^{-1}	0	$38\cdot10^{-6}$	$18\cdot10^{-6}$	$18\cdot10^{-6}$
Constant prefactor (diff)	A_{diff}	Pa^{-1} s^{-1}	$5.79\cdot10^{-19}$	$2.99\cdot10^{-25}$	$2.25\cdot10^{-9}$	$2.25\cdot10^{-9}$
Activation energy (diff)	E_{diff}	J mol^{-1}	$223\cdot10^3$	$159\cdot10^3$	$375\cdot10^3$	$375\cdot10^3$
Activation volume (diff)	V_{diff}	m^3 mol^{-1}	0	$38\cdot10^{-6}$	$6\cdot10^{-6}$	$6\cdot10^{-6}$
Grain size (diff)	d	m	0.001	0.001	0.001	0.001
Grain size exponent (diff)	m	-	2.0	3.0	0	0

Table B.1 Reference parameter values. dis – dislocation creep. diff – diffusion creep.

C.Supplementary material for Chapter 4

Text C.1: ASPECT Methods

C.1.1 Governing equations

We perform numerical simulations of a 3D strike-slip system using the open source finite-element code ASPECT (Advanced Solver for Problems in Earth's ConvecTion, version 2.3.0-pre, commit 886749d; Heister et al., 2017; Kronbichler et al., 2012; Rose et al., 2017; Bangerth et al., 2019). ASPECT solves the following incompressible conservation equations assuming an infinite Prandtl number (i.e., without the inertial term),

$$-\nabla \cdot (2\eta\dot{\varepsilon}) + \nabla P = \rho \mathbf{g}\,, \tag{C.1}$$

$$\nabla \cdot (\mathbf{u}) = 0\,, \tag{C.2}$$

$$\bar{\rho} C_p \left(\frac{\partial T}{\partial t} + \mathbf{u} \cdot \nabla T\right) - \nabla \cdot k\nabla T = \bar{\rho} H + \alpha T (\mathbf{u} \cdot \nabla P)\,, \tag{C.3}$$

$$\frac{\partial c_i}{\partial t} + \mathbf{u} \cdot \nabla c_i = q_i\,, \tag{C.4}$$

where equation (C.1) represents the conservation of momentum, with η the effective viscosity, $\dot{\varepsilon}$ the deviator of the strain rate tensor (defined as $\frac{1}{2}(\nabla\mathbf{u} + (\nabla\mathbf{u})^T)$), $\mathbf{u}$ the velocity, P the pressure, ρ the density, and $\mathbf{g}$ gravity. Equation (C.2) describes the conservation of volume. Equation (C.3) represents the conservation of energy where $\bar{\rho}$ is the reference adiabatic density, C_p the specific heat capacity, T the temperature, k the thermal conductivity, H the radiogenic heating, and α the thermal expansivity. As right-hand-side heating terms, we include radioactive heating and adiabatic heating, in that order. Finally, we solve the advection equation (C.4) for each compositional field c_i (e.g., upper crust, lower crust, and accumulated plastic strain) with reaction rate q_i nonzero only for the plastic strain field.

C.1.2 Rheology

We use a visco-plastic rheology (Glerum et al., 2018), which additionally includes plastic weakening based on accumulated plastic strain. In the viscous regime, we use a composite of diffusion and dislocation creep (Karato & Wu, 1993), formulated as:

$$\eta_{eff}^{diff|dis} = \frac{1}{2} A_{diff|dis}^{\frac{-1}{n}} d^m \dot{\varepsilon}_e^{\frac{1-n}{n}} \exp\left(\frac{(E_{diff|dis} + PV_{diff|dis})}{nRT}\right), \tag{C.5}$$

where A is a scalar prefactor, d the grain size, $\dot{\varepsilon}_e$ the square root of second invariant of the deviatoric strain rate, E the activation energy, P the pressure, V the activation volume, R the gas constant, T the temperature, and n the stress exponent. For diffusion, n = 1 and the equation becomes independent of strain rate. For dislocation creep, the grain size exponent m vanishes, rendering dislocation creep independent of grain size. Values for A, E, V, and n used in our models are composition-dependent and can be found in supplementary Table C.1.

In the plastic regime, when viscous stresses exceed the yield stress, we use the Drucker-Prager yield criterion (Davis & Selvadurai, 2002). The effective plastic viscosity is given by

$$\eta_{\mathrm{eff}}^{\mathrm{pl}} = \frac{\frac{6C\cos\phi}{\sqrt{3}(3-\sin\phi)} + \frac{6P\sin\phi}{\sqrt{3}(3-\sin\phi)}}{2\dot{\varepsilon}_{\mathrm{e}}}, \tag{C.6}$$

where C is the cohesion and ϕ the internal angle of friction. The accumulation of plastic strain is tracked as a compositional field. This field is used to linearly weaken ϕ from an initial value of 30° to a final value of 7.5° over the accumulated plastic strain interval of 0 to 1. The time-integrated value of the strain reaction rate q_i is approximated as $\dot{\varepsilon}_e \cdot dt$ when plastic yielding occurs (with dt the current timestep size).

Text C.2: FastScape Methods

FastScape is a landscape evolution code that changes the topographic surface through uplift, advection, the stream-power law, and hillslope diffusion (Braun & Willett, 2013). It can additionally deposit fluvial sediment (Yuan et al., 2019a) and include a marine component, which handles marine sediment (sand/silt) transport and deposition, and layer compaction based on sand/silt porosity (Yuan et al., 2019b). It uses a 2D horizontal mesh with a uniform resolution. For simplicity, we here assume that the entire model surface is submarine, with uniform properties (i.e., sand and silt transport coefficients are the same), and that there is no compaction (porosity is zero). Hence, FastScape deforms the surface through the uplift rate and marine diffusion equation only as

$$\frac{dh}{dt} = \mathbf{U} + K_m \nabla^2 h, \tag{C.7}$$

where h is the topographic elevation, $\mathbf{U}$ the uplift rate and K_m the marine sediment diffusion coefficient.

Text C.3: ASPECT/FastScape coupling

In this paper we use a two-way coupling of the tectonic ASPECT code and the landscape evolution FastScape code. For this coupling, a FastScape shared library is called by an ASPECT plugin to deform its surface as described in the previous section. The plugin has three main components: 1) Copy the surface height and velocity values from ASPECT. 2) Initialize and run FastScape at a resolution equivalent to or greater than the one used at the surface of ASPECT. If it is the first timestep of the tectonic model run, FastScape is initialized using height and velocity values from ASPECT. In subsequent timesteps, as FastScape runs separately and can be at a higher resolution than ASPECT, only the velocity values from ASPECT are transferred to FastScape. Before running FastScape, the initial topography values are saved. After running FastScape, the new and previous topography are compared to determine a nodal vertical (Z) velocity,

$$\mathbf{V_z} = \frac{h_c - h_p}{dt_a}, \tag{C.8}$$

where h_p is the surface height at the start of the timestep (previous surface), and h_f the surface height after FastScape has been run (current surface), and dt_a the ASPECT timestep. 3) Using

the overarching mesh deformation functionality (see Rose et al., 2017), the Z velocity field is interpolated onto the ASPECT surface to determine the displacement of the mesh surface and interior. From there, ASPECT responds to the change in topography calculated by FastScape due to the induced change in forces that is included in the Stokes equations. At the beginning of the next timestep, the updated velocities computed in the previous timestep are sent to FastScape once again.

The FastScape mesh includes an additional element-size layer of ghost nodes compared to the ASPECT surface mesh. The values of surface height on these nodes are not considered when interpolating the surface back to ASPECT and are used primarily to avoid FastScape boundary artifacts being sent to the ASPECT model (e.g., the boundaries do not uplift from advected topography). To avoid possible erroneous sediment flux out or into the model from artificial slopes, each timestep the ghost nodes are updated with the topography and velocity values of the nearest inward node (an ASPECT boundary node).

Besides passing ASPECT's uplift velocities, we use the plugin's FastScape interface to supply additional input to the surface process model in two ways: 1) to add marine background sedimentation via the sediment rain effect, and 2) to add a boundary sediment flux using the ghost nodes. For the sediment rain, at each nodal point we update FastScape with a flat height increase every ASPECT timestep. Through the diffusion component in equation (C.7), we prescribe a constant sediment flux at the boundary, assuming that

$$\mathbf{Q} = K_m S, \tag{C.9}$$

where **Q** is the sediment flux and S the slope. Since K_m and Q are user-set parameters, to achieve this we alter S by uplifting the boundary ghost nodes every ASPECT timestep so that **Q** remains constant.

Text C.4: Model setup

In this study we examine how a strike-slip fault responds to sedimentation. We therefore set up a 3D box model with dimensions 100×8×120 km (X, Y, and Z, where Z is the vertical component) and 5 compositions representing a wet quartzite upper crust (Rutter & Brodie, 2004), wet anorthite lower crust (Rybacki et al., 2006), dry olivine lithospheric mantle, wet olivine asthenosphere (Hirth and Kohlstedt, 2003), and a sediment layer that has rheologic parameters identical to wet quartzite, but with density and temperature parameters consistent with sediment (Sippel et al., 2017). The total crustal thickness is set to 8 km (4 km upper crust, 4 km lower crust) based on crustal estimates of the area (7-10 km; Mahattanachai et al., 2021). The lithospheric mantle extends between the Moho and the lithosphere-asthenosphere boundary (LAB) at 40 km depth. The LAB depth, like the crust, has been perturbed by a previous extensional period. The remaining material beneath the LAB is considered asthenosphere (Fig. C.1). While there is no initial sediment layer, the top boundary is fixed to a sediment composition so that any top-inflow of material due to topography changes other than uplift is sediment.

The ASPECT model mesh consists of two element sizes: 1 km and 2 km. The upper 8 km of the model is refined at 1 km to best resolve the crust and the forming sediment layer. This high-resolution area additionally extends to a depth of 35 k from X = 42 km to X = 52 km to better resolve the strike-slip fault. All other areas are kept at 2 km resolution.

The initial temperature above the LAB is determined by a steady-state geotherm (Turcotte & Schubert, 2013), and below by a mantle adiabat. For simplicity, an initial weak zone is seeded through a small perturbation: we raise the LAB locally by 10% of the lithospheric mantle thickness. We fix the top boundary temperature at 0 °C and the bottom boundary at the temperature initially determined from the mantle adiabat at that depth. All other boundaries are set to zero heat-flux.

The coupled model is run for 10 Myr, where the model in the first 5 Myr includes non-zero velocity boundary conditions. During this time, the western boundary is given a strike-slip component of 20 mm/yr (in Y), and an extensional component of 0.2 mm/yr (in X), while the Z-component of velocity is set to no-slip. This gives a total of 100 km of dextral strike-slip motion and 1 km of extension. The small extensional component is introduced to avoid compressional pop-ups that form at the shear zone as the lithosphere subsides due to the sediment load (Fig. C.2). The exact extensional value is chosen to accommodate horizontal stress forces related to isostatic compensation. From 5-10 Myr, extension and strike-slip motion stop as the western boundary is set to no-slip in all directions. All other boundary conditions are constant for the entire model run, with the eastern boundary being no-slip in all directions, the north and south boundaries set to periodic to simulate an infinitely long strike-slip fault, the initial lithostatic pressure computed at a reference location prescribed on the bottom boundary to allow for outflow in response to sedimentation, and the top boundary deformed through the use of FastScape.

FastScape is set up with an arbitrarily high sea level so that the entire model is considered submarine. This setup leads to a model with no acting stream power law, and sediment being moved solely through marine sediment diffusion. For simplicity, we additionally assume that there is no compaction and no difference between sand and silt. As such, we use a diffusion coefficient of 500 m^2/y for both, a value consistent with open marine environments in previous modelling studies (e.g., Rouby et al., 2013). During the syn-strike-slip phase of the tectonic model (0-5 Myr) we supply sediment to the model in two ways: 1) To account for pelagic/hemipelagic sedimentation (sediment rain), we deposit at a constant and uniform sedimentation rate of 0.2 mm/yr. 2) We assume there is an asymmetric off-model source of sediment, similar to the eastern Mergui Ridge for the East Andaman Basin, that inputs sediment into the system from the eastern boundary at a rate of 40 m^2/yr. This is done through equation (C.9), wherein we uplift the ghost nodes at each timestep so that a constant flux is prescribed through marine diffusion. After this syn-tectonic stage spanning 5 Myr, sediment

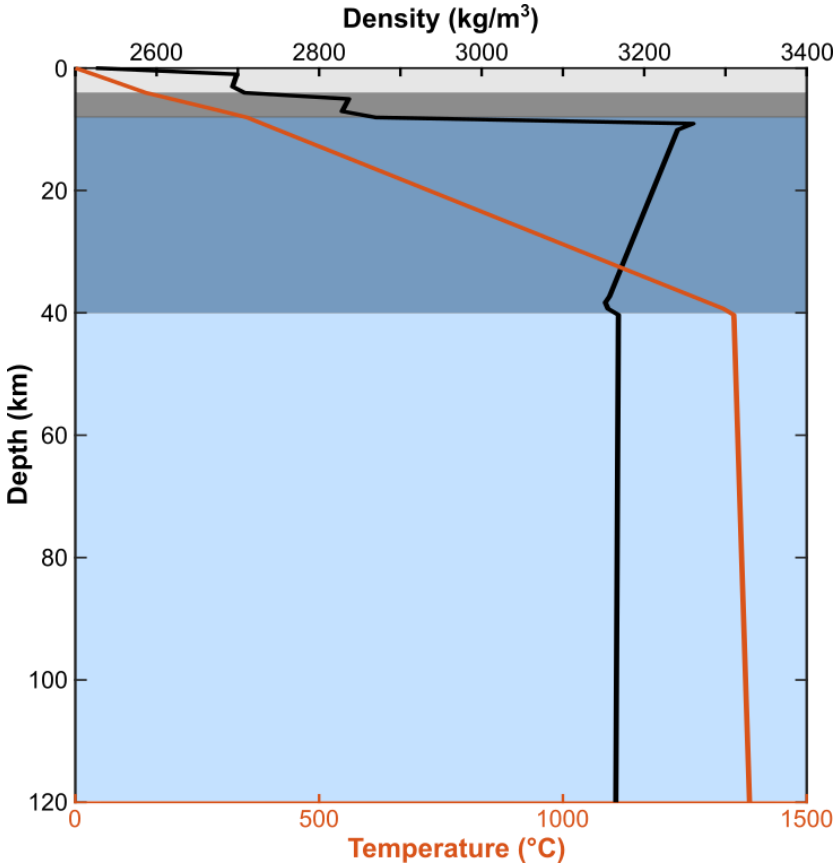

Figure C.1 Initial density (black) and temperature (red) profiles with depth. Colored backgrounds represent the initial compositions, with light gray representing the upper crust, dark gray the lower crust, dark blue the mantle lithosphere, and light blue the asthenosphere.

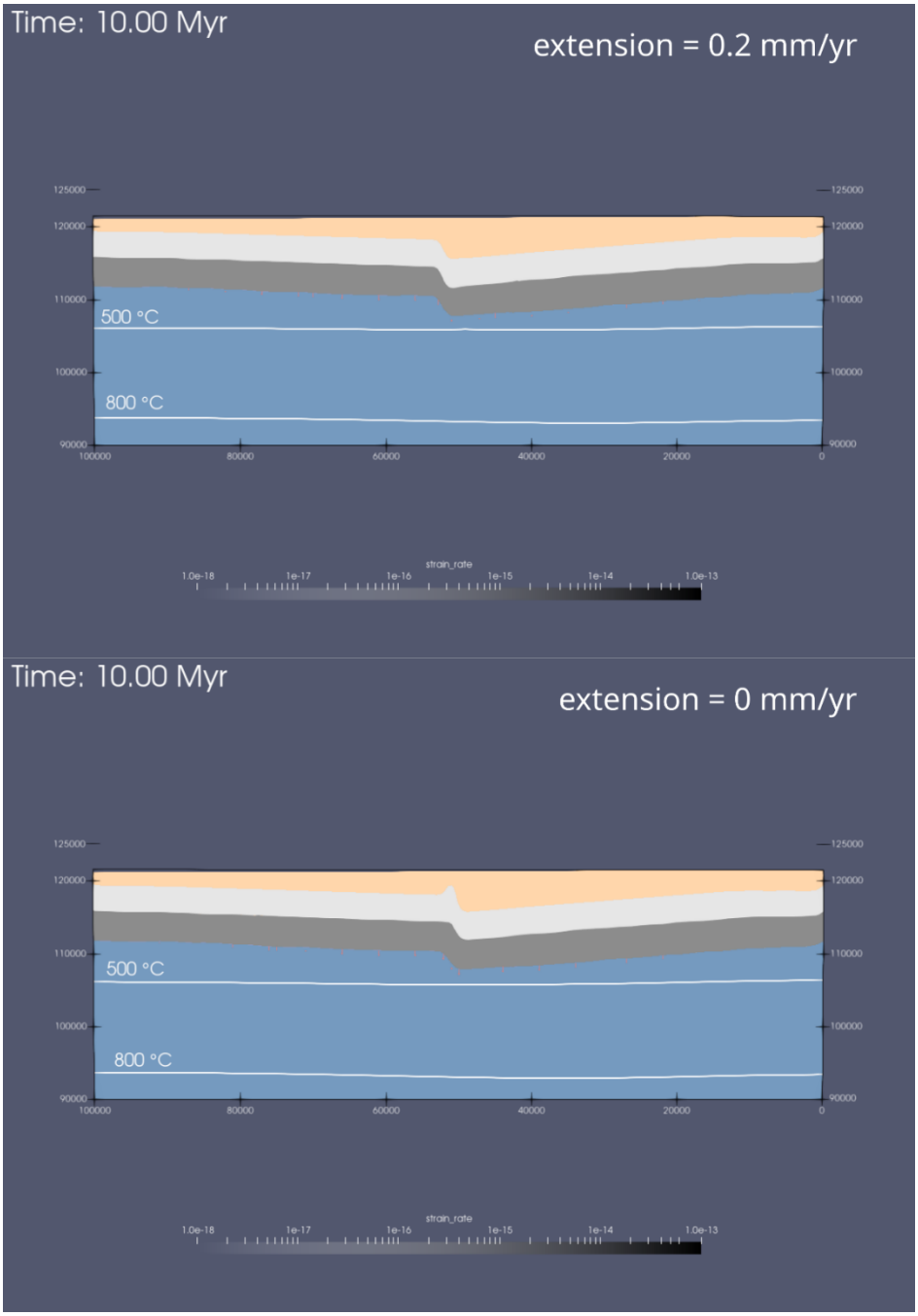

Figure C.2 Comparison showing the reference model with A) a 0.2 mm/yr extensional component. B) no extensional component, leading to the formation of a small compressional pop-up in the center.

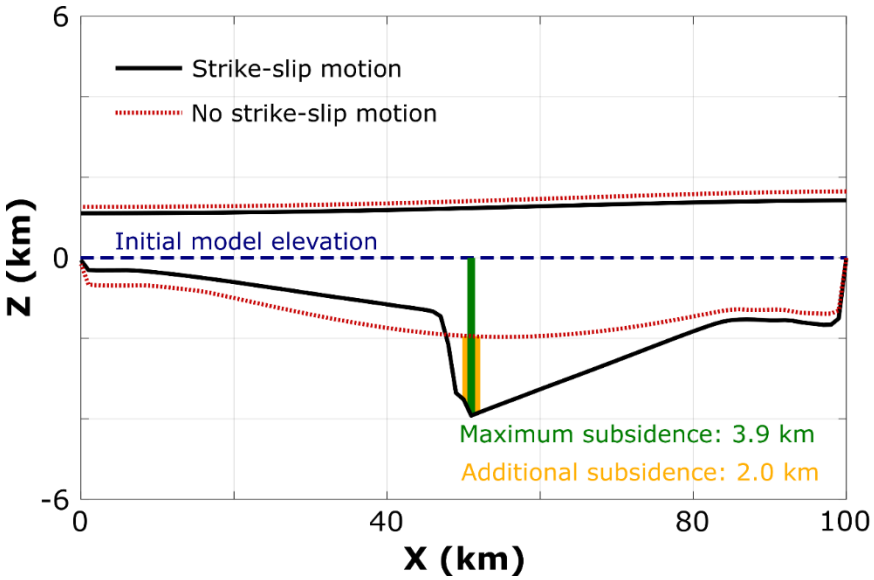

Figure C.3 Comparison of the FastScape basement and topography from two models runs: The black curves represent the reference model; the dotted red curves show the reference model without strike-slip motion. The dashed blue line represents the initial model elevation, the green line indicates the total subsidence in the reference model with strike-slip motion, and the yellow line shows the difference in subsidence when comparing models with and without strike-slip motion. In the case without strike-slip motion, maximum subsidence and basin asymmetry are both greatly reduced.

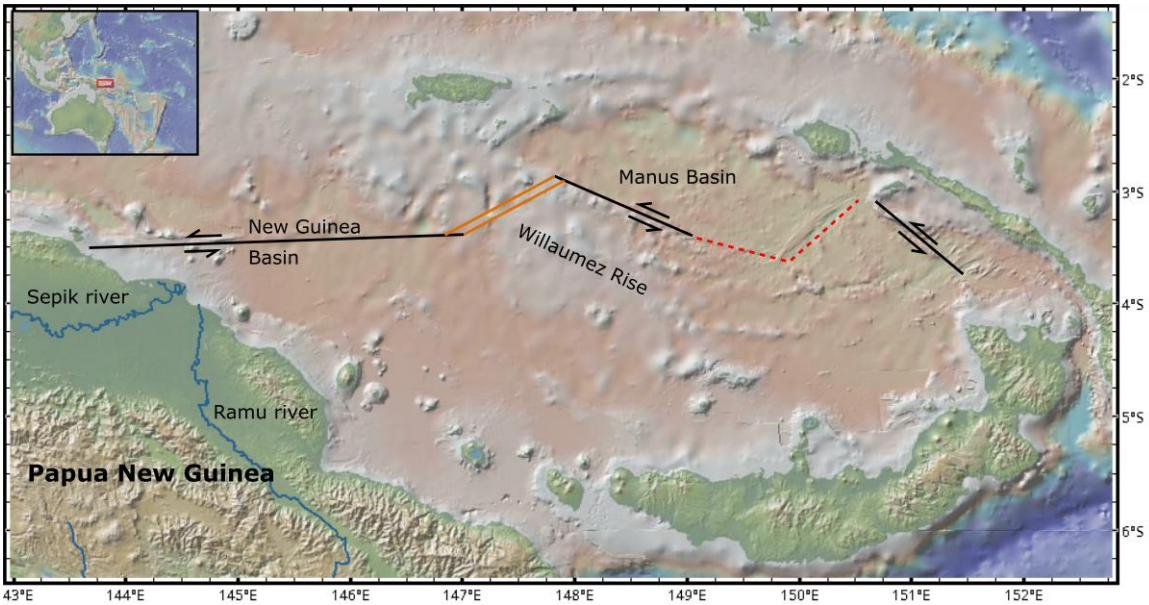

Figure C.4 Regional map of the Manus back-arc region, with fault locations based on Fig. 1 in Martinez and Taylor, 1996. Black lines indicate strike-slip faults, parallel orange lines spreading centers, dashed red lines lava fields, and blue lines major rivers. This figure was made using GeoMappApp (www.geomapapp.org; Ryan et al., 2009).

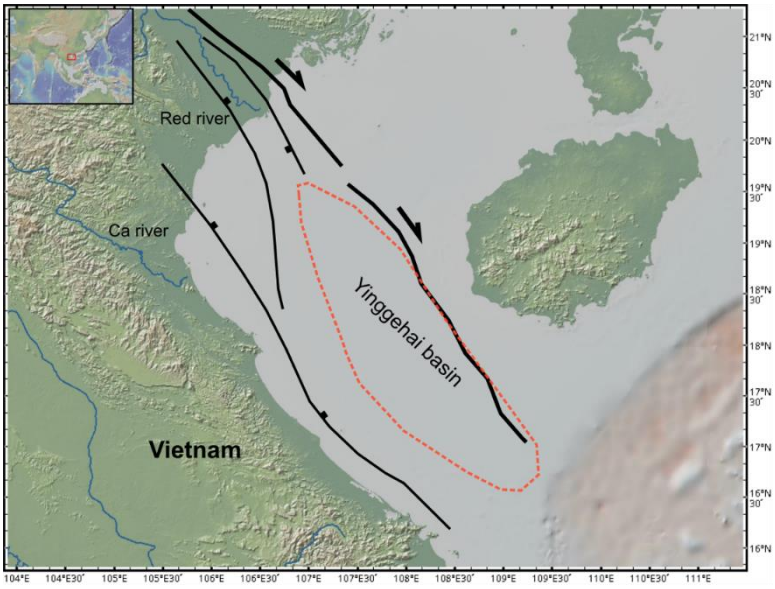

Figure C.5 Regional map showing the Red River Fault Zone and location of the Yinggehai basin. Fault locations based on Fig. 10 in Noda, 2013. Black lines show faults, blue lines major rivers, and the Yinggehai basin is outlined in the dashed orange circle. This figure was made using GeoMappApp (www.geomapapp.org; Ryan et al., 2009).

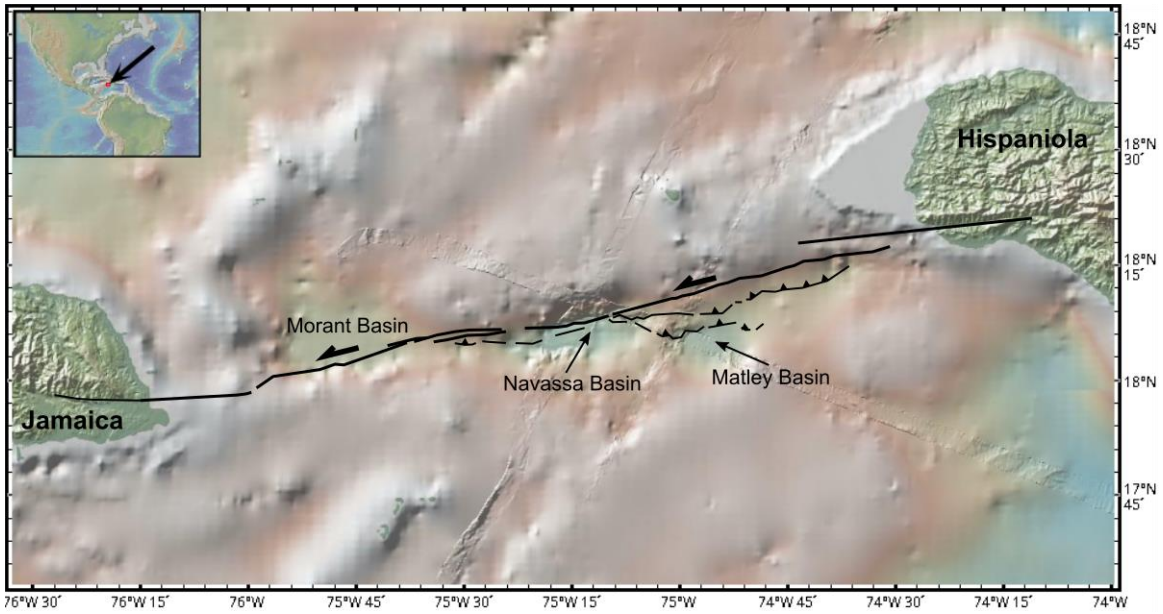

Figure C.6 Regional map of the Jamaica Passage showing the Navassa strike-slip basin along the Enriquillo-Plantain-Garden Fault Zone. Fault locations based on Fig. 6 in Corbeau et al., 2016. This figure was made using GeoMappApp (www.geomapapp.org; Ryan et al., 2009).

Parameter	Symbol	Units	Sediment	Upper crust	Lower crust	Lithospheric mantle	Asthenosphere
Reference density (at surface conditions)	ρ_0	kg m^{-3}	2520	2700	2850	3280	3300
Thermal expansivity	α	K^{-1}	$3.7 \cdot 10^{-5}$	$2.7 \cdot 10^{-5}$	$2.7 \cdot 10^{-5}$	$3.0 \cdot 10^{-5}$	$3.0 \cdot 10^{-5}$
Thermal diffusivity	κ	$m^2 s^{-1}$	$7.28 \cdot 10^{-7}$	$9.26 \cdot 10^{-7}$	$5.85 \cdot 10^{-7}$	$8.38 \cdot 10^{-7}$	$8.33 \cdot 10^{-7}$
Heat capacity	C_p	J kg^{-1} K^{-1}	1200	1200	1200	1200	1200
Heat production	H	W m^{-3}	$1.2 \cdot 10^{-6}$	$1.5 \cdot 10^{-6}$	$0.2 \cdot 10^{-6}$	0	0
Cohesion	C	Pa	$20 \cdot 10^6$	$20 \cdot 10^6$	$20 \cdot 10^6$	$20 \cdot 10^6$	$20 \cdot 10^6$
Internal friction angle (unweakened)	ϕ	◦	30	30	30	30	30
Strain weakening interval	-	-	[0,1]	[0,1]	[0,1]	[0,1]	[0,1]
Strain weakening factor	ϕ_{wf}	-	0.25	0.25	0.25	0.25	0.25
Creep properties			Sediment	Wet quartzite	Wet anorthite	Dry olivine	Wet olivine
Stress exponent (dis)	n	-	4.0	4.0	3.0	3.5	3.5
Constant prefactor (dis)	A_{dis}	Pa^{-n} s^{-1}	$8.57 \cdot 10^{-28}$	$8.57 \cdot 10^{-28}$	$7.13 \cdot 10^{-18}$	$6.52 \cdot 10^{-16}$	$2.12 \cdot 10^{-15}$
Activation energy (dis)	E_{dis}	J mol^{-1}	$223 \cdot 10^3$	$223 \cdot 10^3$	$345 \cdot 10^3$	$530 \cdot 10^3$	$480 \cdot 10^3$
Activation volume (dis)	V_{dis}	m^3 mol^{-1}	0	0	$38 \cdot 10^{-6}$	$18 \cdot 10^{-6}$	$11 \cdot 10^{-6}$
Constant prefactor (diff)	A_{diff}	Pa^{-1} s^{-1}	$5.79 \cdot 10^{-19}$	$5.79 \cdot 10^{-19}$	$2.99 \cdot 10^{-25}$	$2.25 \cdot 10^{-9}$	$1.5 \cdot 10^{-9}$
Activation energy (diff)	E_{diff}	J mol^{-1}	$223 \cdot 10^3$	$223 \cdot 10^3$	$159 \cdot 10^3$	$375 \cdot 10^3$	$335 \cdot 10^3$
Activation volume (diff)	V_{diff}	m^3 mol^{-1}	0	0	$38 \cdot 10^{-6}$	$6 \cdot 10^{-6}$	$4 \cdot 10^{-6}$
Grain size (diff)	d	m	0.001	0.001	0.001	0.001	0.001
Grain size exponent (diff)	m	-	2.0	2.0	3.0	0	0

Table C.1 ASPECT model parameters. Abbreviations: dis – dislocation creep, diff – diffusion creep.

Parameter	Symbol	Unit	Value
Marine sand transport coefficient	K_{sand}	m^2/yr	500
Surface sand porosity	φ_{sand}	-	0
Sand e-folding depth	z_{sand}	m	0
Marine silt transport coefficient	K_{silt}	m^2/yr	500
Surface silt porosity	φ_{silt}	-	0
Silt e-folding depth	z_{silt}	m	0
Sand-shale ratio	F	-	1
Thickness of transport layer	L	m	100
Sea level	h_{sea}	m	5000

Table C.2 FastScape model parameters.

References

Acocella, V. (2008). Transform faults or Overlapping Spreading Centers? Oceanic ridge interactions revealed by analogue models. *Earth and Planetary Science Letters*, *265*(3–4), 379–385. https://doi.org/10.1016/j.epsl.2007.10.025

Agostini, A., Corti, G., Zeoli, A., & Mulugeta, G. (2009). Evolution, pattern, and partitioning of deformation during oblique continental rifting: Inferences from lithospheric-scale centrifuge models. *Geochemistry, Geophysics, Geosystems*, *10*(11). https://doi.org/10.1029/2009GC002676

Albaric, J., Déverchère, J., Petit, C., Perrot, J., & Le Gall, B. (2009). Crustal rheology and depth distribution of earthquakes: Insights from the central and southern East African Rift System. *Tectonophysics*, *468*(1–4), 28–41. https://doi.org/10.1016/J.TECTO.2008.05.021

Albers, E., Bach, W., Pérez-Gussinyé, M., McCammon, C., & Frederichs, T. (2021). Serpentinization-Driven H2 Production From Continental Break-Up to Mid-Ocean Ridge Spreading: Unexpected High Rates at the West Iberia Margin. *Frontiers in Earth Science*, *9*, 487. https://doi.org/10.3389/FEART.2021.673063/BIBTEX

Allen, P. A., & Allen, J. R. (2013). *Basin Analysis 3rd edition*. https://doi.org/10.1017/CBO9781107415324.004

Allken, V., Huismans, R. S., & Thieulot, C. (2011). Three-dimensional numerical modeling of upper crustal extensional systems. *Journal of Geophysical Research: Solid Earth*, *116*(10), 1–15. https://doi.org/10.1029/2011JB008319

Allken, V., Huismans, R. S., & Thieulot, C. (2012). Factors controlling the mode of rift interaction in brittle-ductile coupled systems: A 3D numerical study. *Geochemistry, Geophysics, Geosystems*, *13*(5), 1–18. https://doi.org/10.1029/2012GC004077

Ammann, N., Liao, J., Gerya, T., & Ball, P. (2017). Oblique continental rifting and long transform fault formation based on 3D thermomechanical numerical modeling. *Tectonophysics*, (February), 1–16. https://doi.org/10.1016/j.tecto.2017.08.015

Andrés-Martínez, M., Pérez-Gussinyé, M., Armitage, J., & Morgan, J. P. (2019). Thermomechanical Implications of Sediment Transport for the Architecture and Evolution of Continental Rifts and Margins. *Tectonics*, *38*(2), 641–665. https://doi.org/10.1029/2018TC005346

Armitage, J. J., Dunkley Jones, T., Duller, R. A., Whittaker, A. C., & Allen, P. A. (2013). Temporal buffering of climate-driven sediment flux cycles by transient catchment response. *Earth and Planetary Science Letters*, *369–370*, 200–210. https://doi.org/10.1016/J.EPSL.2013.03.020

Artemieva, I. M. (2006). Global 1° × 1° thermal model TC1 for the continental lithosphere: Implications for lithosphere secular evolution. *Tectonophysics*, *416*(1–2), 245–277. https://doi.org/10.1016/j.tecto.2005.11.022

Artemieva, I. M., & Mooney, W. D. (2001). Thermal thickness and evolution of Precambrian lithosphere: A global study. *Journal of Geophysical Research: Solid Earth*, *106*(B8), 16387–16414. https://doi.org/https://doi.org/10.1029/2000JB900439

Bahadori, A., & Holt, W. E. (2019). Geodynamic evolution of southwestern North America since the Late Eocene. *Nature Communications*, *10*(1), 5213. https://doi.org/10.1038/s41467-019-12950-8

Bangerth, W., Dannberg, J., Gassmoeller, R., & Heister, T. (2019). ASPECT v2.1.0. *Zenodo*. Retrieved from https://doi.org/10.5281/zenodo.2653531

Barnett-Moore, N., Müller, D. R., Williams, S., Skogseid, J., & Seton, M. (2018). A reconstruction of the North Atlantic since the earliest Jurassic. *Basin Research*, *30*, 160–185. https://doi.org/10.1111/bre.12214

Baxter, A. T., Hannington, M. D., Stewart, M. S., Emberley, J. M., Breker, K., Krätschell, A., … Anderson, M. O. (2020). Shallow Seismicity and the Classification of Structures in the Lau Back-Arc Basin. *Geochemistry, Geophysics, Geosystems*, *21*(7), e2020GC008924. https://doi.org/https://doi.org/10.1029/2020GC008924

Bayrakci, G., Minshull, T. A., Sawyer, D. S., Reston, T. J., Klaeschen, D., Papenberg, C., … Morgan, J. K. (2016). Fault-controlled hydration of the upper mantle during continental rifting. *Nature Geoscience 2016 9:5*, *9*(5), 384–388. https://doi.org/10.1038/ngeo2671

Beniest, A., Koptev, A., Leroy, S., Sassi, W., & Guichet, X. (2017). Two-Branch Break-up Systems by a Single Mantle Plume: Insights from Numerical Modeling. *Geophysical Research Letters*, *44*(19), 9589–9597. https://doi.org/https://doi.org/10.1002/2017GL074866

Beucher, R., & Huismans, R. S. (2020). Morphotectonic Evolution of Passive Margins Undergoing Active Surface Processes: Large-Scale Experiments Using Numerical Models. *Geochemistry, Geophysics, Geosystems*, *21*(5). https://doi.org/10.1029/2019GC008884

Bickert, M., Lavier, L., & Cannat, M. (2020). How do detachment faults form at ultraslow mid-ocean ridges in a thick axial lithosphere? *Earth and Planetary Science Letters*, *533*, 116048. https://doi.org/10.1016/J.EPSL.2019.116048

Boettcher, M. S., & Jordan, T. H. (2004). Earthquake scaling relations for mid-ocean ridge transform faults. *Journal of Geophysical Research : Solid Earth*, *109*(2), 1–21.

Borges, T. A., & Gambôa, L. A. P. (2015). Sismoestratigrafia Do Limite Sul Da Bacia de Santos e Suas Implicações Na Evolução Do Atlântico Sul Primordial. *Boletim de Geociências Da Petrobras*, *23*(1/2). Retrieved from http://publicacoes.petrobras.com.br/main.jsp?lumPageId=8A9E308F545405DE0154A04B46AD0C9E&lumItemId=8A9D2AAF5CA274FD015D746F91B218E5&previewItemId=8A9D2AAF5CA274FD015D746F91A818E4&publicacaoId=8A9D2AAF5A284744015A2958DE4D3BC9&lastItem=1

Braun, J., & Willett, S. D. (2013a). A very efficient O(n), implicit and parallel method to solve the stream power equation governing fluvial incision and landscape evolution. *Geomorphology*, *180–181*, 170–179. https://doi.org/10.1016/j.geomorph.2012.10.008

Braun, J., & Willett, S. D. (2013b). A very efficient O(n), implicit and parallel method to solve the stream power equation governing fluvial incision and landscape evolution. *Geomorphology*, *180–181*, 170–179. https://doi.org/10.1016/J.GEOMORPH.2012.10.008

Bredow, E., Steinberger, B., Gassmöller, R., & Dannberg, J. (2017). How plume-ridge interaction shapes the crustal thickness pattern of the Réunion hotspot track. *Geochemistry, Geophysics, Geosystems*, *18*(8), 2930–2948. https://doi.org/10.1002/2017GC006875

Brune, S., Corti, G., & Ranalli, G. (2017). Controls of inherited lithospheric heterogeneity on rift linkage: Numerical and analog models of interaction between the Kenyan and Ethiopian rifts across the Turkana depression. *Tectonics*, *36*(9), 1767–1786. https://doi.org/10.1002/2017TC004739

Brune, S., Heine, C., Clift, P. D., & Pérez-Gussinyé, M. (2017). Rifted margin architecture and crustal rheology: Reviewing Iberia-Newfoundland, Central South Atlantic, and South China Sea. *Marine and Petroleum Geology*, *79*, 257–281. https://doi.org/10.1016/j.marpetgeo.2016.10.018

Brune, S., Heine, C., Pérez-Gussinyé, M., & Sobolev, S. V. (2014). Rift migration explains continental margin asymmetry and crustal hyper-extension. *Nature Communications*, *5*, 1–9. https://doi.org/10.1038/ncomms5014

Brune, S., Williams, S. E., Butterworth, N. P., & Müller, R. D. (2016). Abrupt plate accelerations shape rifted continental margins. *Nature*, *536*(7615), 201–204. https://doi.org/10.1038/nature18319

Buck, W. R. (2015). *The Dynamics of Continental Breakup and Extension*. *Treatise on Geophysics: Second Edition* (Vol. 6). Elsevier B.V. https://doi.org/10.1016/B978-0-444-53802-4.00118-4

Buck, W. Roger. (1988). flexural rotation of normal faults. *Tectonics*, *7*(5), 959–973. https://doi.org/10.1029/TC007I005P00959

Buck, W Roger, Lavier, L. L., & Poliakov, A. N. B. (1999). How to make a rift wide. *Phil. Trans. R. Soc., A. 357*, 671–693.

Buiter, S. J. H. (2021). A discussion on how, when and where surface processes interplay with extensional tectonic deformation. *EGU General Assembly 2021*, *EGU21-8665*. https://doi.org/https://doi.org/10.5194/egusphere-egu21-8665

Buiter, S. J. H., Huismans, R. S., & Beaumont, C. (2008). Dissipation analysis as a guide to mode selection during crustal extension and implications for the styles of sedimentary basins. *Journal of Geophysical Research: Solid Earth*, *113*(6). https://doi.org/10.1029/2007JB005272

Buiter, S. J. H., & Torsvik, T. H. (2014, September 1). A review of Wilson Cycle plate margins: A role for mantle plumes in continental break-up along sutures? *Gondwana Research*. Elsevier Inc. https://doi.org/10.1016/j.gr.2014.02.007

C. Beck, Grieser, J., Kottek, M., Rubel, F., & Rudolf, B. (2006). Characterizing global climate change by means of Köppen climate classification.

Calais, E., Ebinger, C., Hartnady, C., & Nocquet, J. M. (2006). Kinematics of the East African Rift from GPS and earthquake slip vector data. *Geological Society, London, Special Publications*, *259*, 9–22.

Chang, H. K., Kowsmann, R. O., Figueiredo, A. M. F., & Bender, A. (1992). Tectonics and Stratigraphy of the East Brazil Rift System: An Overview. *Tectonophysics*, *213*(1–2), 97–138. https://doi.org/10.1016/0040-1951(92)90253-3

Chenin, P., Manatschal, G., Decarlis, A., Schmalholz, S. M., Duretz, T., & Beltrando, M. (2019). Emersion of Distal Domains in Advanced Stages of Continental Rifting Explained by Asynchronous Crust and Mantle Necking. *Geochemistry, Geophysics, Geosystems*, *20*(8), 3821–3840. https://doi.org/https://doi.org/10.1029/2019GC008357

Chenin, P., Manatschal, G., Ghienne, J.-F. J.-F., & Chao, P. (2021). The syn-rift tectono-stratigraphic record of rifted margins (Part II): A new model to break through the proximal/distal interpretation frontier. *Basin Research*, *00*, 1–44. https://doi.org/10.1111/bre.12628

Chenin, P., Manatschal, G., Picazo, S., Müntener, O., Karner, G., Johnson, C., & Ulrich, M. (2017). Influence of the architecture of magma-poor hyperextended rifted margins on orogens produced by the closure of narrow versus wide oceans. *Geosphere*, *13*(2), 559–576. https://doi.org/10.1130/GES01363.1

Chian, D., Reid, I., & Jackson, H. (2001). Crustal structure beneath Orphan Basin and implications for nonvolcanic continental rifting. *Journal of Geophysical Research*, *106*, 10,923-10,940.

Choi, E., Buck, W. R., Lavier, L. L., & Petersen, K. D. (2013). Using core complex geometry to constrain fault strength. *Geophysical Research Letters*, *40*(15), 3863–3867. https://doi.org/10.1002/GRL.50732

Clerc, C., Ringenbach, J. C., Jolivet, L., & Ballard, J. F. (2018). Rifted margins: Ductile deformation, boudinage, continentward-dipping normal faults and the role of the weak lower crust. *Gondwana Research*, *53*, 20–40. https://doi.org/10.1016/J.GR.2017.04.030

Clift, P. D., Brune, S., & Quinteros, J. (2015). Climate changes control offshore crustal structure at South China Sea continental margin. *Earth and Planetary Science Letters*, *420*, 66–72. https://doi.org/10.1016/j.epsl.2015.03.032

Clift, P. D., & Sun, Z. (2006). The sedimentary and tectonic evolution of the Yinggehai-Song Hong basin and the southern Hainan margin, South China Sea: Implications for Tibetan uplift and monsoon intensification. *Journal of Geophysical Research: Solid Earth*, *111*(6), 1–28. https://doi.org/10.1029/2005JB004048

Conder, J. A., & Wiens, D. A. (2011). Shallow seismicity and tectonics of the central and northern Lau Basin. *Earth and Planetary Science Letters*, *304*(3–4), 538–546. https://doi.org/10.1016/j.epsl.2011.02.032

Corbeau, J., Rolandone, F., Leroy, S., Mercier de Lépinay, B., Meyer, B., Ellouz-Zimmermann, N., & Momplaisir, R. (2016). The northern Caribbean plate boundary in the Jamaica Passage: Structure and seismic stratigraphy. *Tectonophysics*, *675*, 209–226. https://doi.org/10.1016/j.tecto.2016.03.022

Corti, G. (2012). Evolution and characteristics of continental rifting: Analog modeling-inspired view and comparison with examples from the East African Rift System. *Tectonophysics*, *522–523*(1), 1–33. https://doi.org/10.1016/j.tecto.2011.06.010

Corti, G., Cioni, R., Franceschini, Z., Sani, F., Scaillet, S., Molin, P., … Glerum, A. (2019). Aborted propagation of the Ethiopian rift caused by linkage with the Kenyan rift. *Nature Communications*, *10*(1), 1–11. https://doi.org/10.1038/s41467-019-09335-2

Crameri, F. (2018). Scientific colour maps. Zenodo. https://doi.org/http://doi.org/10.5281/zenodo.1243862

Crameri, Fabio, Shephard, G. E., & Heron, P. J. (2020). The misuse of colour in science communication. *Nature Communications 2020 11:1*, *11*(1), 1–10. https://doi.org/10.1038/s41467-020-19160-7

Curray, J. R. (2005). Tectonics and history of the Andaman Sea region. *Journal of Asian Earth*

Sciences, *25*(1), 187–232. https://doi.org/10.1016/j.jseaes.2004.09.001

Davis, R. O., & Selvadurai, A. P. . (2002). *Plasticity and Geomechanics*. Cambridge University Press.

de Wit, M. J., Stankiewicz, J., & Reeves, C. (2008). Restoring pan-African-Brasiliano connections: More Gondwana control, less Trans-Atlantic corruption. *Geological Society Special Publication*, *294*, 399–412. https://doi.org/10.1144/SP294.20

Densmore, A. L., Allen, P. A., & Simpson, G. (2007). Development and response of a coupled catchment fan system under changing tectonic and climatic forcing. *Journal of Geophysical Research: Earth Surface*, *112*, 1002. https://doi.org/10.1029/2006JF000474

Depolo, C. M., & Anderson, J. G. (2000). Estimating the slip rates of normal faults in the Great Basin, USA. *Basin Research*, *12*(3–4), 227–240. https://doi.org/10.1111/J.1365-2117.2000.00131.X

Dong, M., Zhang, J., Brune, S., Wu, S., Fang, G., & Yu, L. (2020). Quantifying Postrift Lower Crustal Flow in the Northern Margin of the South China Sea. *Journal of Geophysical Research: Solid Earth*, *125*(2). https://doi.org/10.1029/2019JB018910

Dubinin, E. P., Grokholsky, A. L., & Makushkina, A. I. (2018). Physical modeling of the formation conditions of microcontinents and continental marginal plateaus. *Izvestiya, Physics of the Solid Earth*, *54*(1), 66–78. https://doi.org/10.1134/S1069351318010056

Dunbar, J., & Sawyer, D. (1988). Continental rifting at pre-existing lithospheric weaknesses. *Nature*, *333*(6172), 450–452. https://doi.org/10.1038/333450a0

Eagles, G., Pérez-Díaz, L., & Scarselli, N. (2015). Getting over continent ocean boundaries. *Earth-Science Reviews*, *151*, 244–265.

Eagles, G., Gloaguen, R., & Ebinger, C. (2002). Kinematics of the Danakil microplate. *Earth and Planetary Science Letters*, *203*(2), 607–620. https://doi.org/10.1016/S0012-821X(02)00916-0

Ebinger, C., & Scholz, C. A. (2012). Continental Rift Basins: The East African Perspective. In *Tectonics of Sedimentary Basins: Recent Advances* (pp. 183–208). John Wiley & Sons, Ltd. https://doi.org/10.1002/9781444347166.ch9

Emmanuel, S., & Berkowitz, B. (2006). Suppression and stimulation of seafloor hydrothermal convection by exothermic mineral hydration. *Earth and Planetary Science Letters*, *243*(3–4), 657–668. https://doi.org/10.1016/J.EPSL.2006.01.028

Evain, M., Afilhado, A., Rigoti, C., Loureiro, A., Alves, D., Klingelhoefer, F., … Aslanian, D. (2015). Deep Structure of the Santos Basin-São Paulo Plateau System, SE Brazil. *Journal of Geophysical Research: Solid Earth*, *120*, 5401–5431. https://doi.org/10.1002/2014jb011561

Fromm, T., Planert, L., Jokat, W., Ryberg, T., Behrmann, J. H., Weber, M. H., & Haberland, C. (2015). South Atlantic opening: A plume-induced breakup? *Geology*, *43*(10), 931–934. https://doi.org/10.1130/G36936.1

Funck, T. (2003). Crustal structure of the ocean-continent transition at Flemish Cap: Seismic refraction results. *Journal of Geophysical Research*, *108*(B11), 1–20. https://doi.org/10.1029/2003jb002434

Garfunkel, Z., & Ben-Avraham, Z. (1996). The structure of the Dead Sea basin. *Tectonophysics*, *266*(1–4), 155–176. https://doi.org/10.1016/S0040-1951(96)00188-6

Gassmöller, R., Dannberg, J., Bredow, E., Steinberger, B., & Torsvik, T. H. (2016). Major influence of plume-ridge interaction, lithosphere thickness variations, and global mantle flow on hotspot volcanism—The example of Tristan. *Geochemistry Geophysics Geosystems*, 1454–1479. https://doi.org/doi:10.1002/ 2015GC006177

Gassmöller, Rene, Lokavarapu, H., Heien, E., Puckett, E. G., & Bangerth, W. (2018). Flexible and Scalable Particle-in-Cell Methods With Adaptive Mesh Refinement for Geodynamic Computations. *Geochemistry, Geophysics, Geosystems*, *19*(9), 3596–3604. https://doi.org/10.1029/2018GC007508

Gawthorpe, R. L., & Leeder, M. R. (2000). Tectono-sedimentary evolution of active extensional basins. *Basin Research*, *12*(3–4), 195–218. https://doi.org/10.1111/J.1365-2117.2000.00121.X

Gerlings, J., Louden, K. E., & Jackson, H. R. (2011). Crustal structure of the Flemish Cap Continental Margin (eastern Canada): An analysis of a seismic refraction profile. *Geophysical Journal International*, *185*(1), 30–48. https://doi.org/10.1111/j.1365-246X.2011.04931.x

Gernigon, L., Gaina, C., Olesen, O., Ball, P. J., Péron-Pinvidic, G., & Yamasaki, T. (2012). The Norway Basin revisited: From continental breakup to spreading ridge extinction. *Marine and Petroleum Geology*, *35*(1), 1–19. https://doi.org/10.1016/j.marpetgeo.2012.02.015

Gerya, Taras. (2010). Dynamical Instability Produces Transform Faults at Mid-Ocean Ridges. *Science*, *329*(August), 1047–1050. https://doi.org/10.1126/science.1189134

Gerya, Taras. (2012). Origin and models of oceanic transform faults. *Tectonophysics*, *522–523*, 34–54. https://doi.org/10.1016/j.tecto.2011.07.006

Gerya, Taras. (2013a). Initiation of transform faults at rifted continental margins: 3D petrological-thermomechanical modeling and comparison to the Woodlark Basin. *Petrology*, *21*(6), 550–560.

Gerya, Taras. (2013b). Three-dimensional thermomechanical modeling of oceanic spreading initiation and evolution. *Physics of the Earth and Planetary Interiors*, *214*, 35–52. https://doi.org/10.1016/j.pepi.2012.10.007

Gerya, T V, Stern, R. J., Baes, M., Sobolev, S. V, & Whattam, S. A. (2015). Plate tectonics on the Earth triggered by plume-induced subduction initiation. *Nature*, *527*(7577), 221–225. https://doi.org/10.1038/nature15752

Gibbons, A. D., Whittaker, J. M., & Müller, R. D. (2013). The breakup of East Gondwana: Assimilating constraints from Cretaceous ocean basins around India into a best-fit tectonic model. *Journal of Geophysical Research: Solid Earth*, *118*(3), 808–822. https://doi.org/https://doi.org/10.1002/jgrb.50079

Glerum, A., Brune, S., Stamps, D. S., & Strecker, M. R. (2020). Victoria continental microplate dynamics controlled by the lithospheric strength distribution of the East African Rift. *Nature Communications*, *11*(1), 1–15. https://doi.org/10.1038/s41467-020-16176-x

Glerum, A., Thieulot, C., Fraters, M., Blom, C., & Spakman, W. (2018). Nonlinear viscoplasticity in ASPECT: Benchmarking and applications to subduction. *Solid Earth*,

9(2), 267–294. https://doi.org/10.5194/se-9-267-2018

Goldsworthy, M., & Jackson, J. (2001). Migration of activity within normal fault systems: examples from the Quaternary of mainland Greece. *Journal of Structural Geology*, *23*(2–3), 489–506. https://doi.org/10.1016/S0191-8141(00)00121-8

Gouiza, M., Hall, J., & Welford, J. K. (2017). Tectono-stratigraphic evolution and crustal architecture of the Orphan Basin during North Atlantic rifting. *International Journal of Earth Sciences*, *106*(3), 917–937. https://doi.org/10.1007/s00531-016-1341-0

Guerit, L., Yuan, X. P., Carretier, S., Bonnet, S., Rohais, S., Braun, J., & Rouby, D. (2019). Fluvial landscape evolution controlled by the sediment deposition coefficient: Estimation from experimental and natural landscapes. *Geology*, *47*(9), 853–856. https://doi.org/10.1130/G46356.1

Guiraud, M., Buta-Neto, A., & Quesne, D. (2010). Segmentation and Differential Post-Rift Uplift at the Angola Margin as Recorded by the Transform-Rifted Benguela and Oblique-to-Orthogonal-Rifted Kwanza Basins. *Marine and Petroleum Geology*, *27*(5), 1040–1068. https://doi.org/10.1016/j.marpetgeo.2010.01.017

Guo, Z., & Hall, R. W. (1992). Fast fully parallel thinning algorithms. *CVGIP: Image Understanding*, *55*(3), 317–328. https://doi.org/10.1016/1049-9660(92)90029-3

Gurbuz, A. (2010). Geometric characteristics of pull-apart basins. *Lithosphere*, *2*(3), 199–206. https://doi.org/10.1130/L36.1

Haworth, R., & Keen, C. E. (1979). The Canadian Atlantic margin: a passive continental margin encompassing an active past. *Tectonophysics*, *59*, 83–126.

Heckenbach, E. L., Brune, S., Glerum, A. C., & Bott, J. (2021). Is there a Speed Limit for the Thermal Steady-State Assumption in Continental Rifts? *Geochemistry, Geophysics, Geosystems*, *n/a*(n/a), e2020GC009577. https://doi.org/https://doi.org/10.1029/2020GC009577

Heidbach, O., Reinecker, J., Tingay, M., Müller, B., Sperner, B., Fuchs, K., & Wenzel, F. (2007). Plate boundary forces are not enough: Second- and third-order stress patterns highlighted in the World Stress Map database. *Tectonics*, *26*(6), 1–19. https://doi.org/10.1029/2007TC002133

Heine, C, & Müller, R. D. (2005). Late Jurassic rifting along the Australian North West Shelf: margin geometry and spreading ridge configuration. *Australian Journal of Earth Sciences*, *52*(1), 27–39. https://doi.org/10.1080/08120090500100077

Heine, Christian, Zoethout, J., & Müller, R. D. (2013). Kinematics of the South Atlantic rift. *Solid Earth*, *4*(2), 215–253. https://doi.org/10.5194/se-4-215-2013

Heister, T., Dannberg, J., Gassmöller, R., & Bangerth, W. (2017). High Accuracy Mantle Convection Simulation through Modern Numerical Methods – II: Realistic Models and Problems. *Geophysical Journal International*, *210*, 833–851. https://doi.org/doi:10.1093/gji/ggx195

Heron, P. J., Peace, A. L., McCaffrey, K. J. W., Welford, J. K., Wilson, R., van Hunen, J., & Pysklywec, R. N. (2019). Segmentation of Rifts Through Structural Inheritance: Creation of the Davis Strait. *Tectonics*, *38*(7), 2411–2430. https://doi.org/10.1029/2019TC005578

Hirth, G., & Kohlstedt, D. (2003). Rheology of the upper mantle and the mantle wedge: a view

from the experimentalists. *Inside the Subudction Factory Geophysical Monograph (American Geophysical Union)*, *183*.

Hoffmann, H. J., & Reston, T. J. (1992). Nature of the S reflector beneath the Galicia Banks rifted margin: preliminary results from prestack depth migration. *Geology*, *20*(12), 1091–1094. https://doi.org/10.1130/0091-7613(1992)020<1091:NOTSRB>2.3.CO;2

Huismans, R., & Beaumont, C. (2011). Depth-dependent extension, two-stage breakup and cratonic underplating at rifted margins. *Nature*, *473*, 74–78.

Huismans, R. S., & Beaumont, C. (2003). Symmetric and asymmetric lithospheric extension: Relative effects of frictional-plastic and viscous strain softening. *Journal of Geophysical Research: Solid Earth*, *108*(B10), 1–22. https://doi.org/10.1029/2002jb002026

Huismans, R. S., & Beaumont, C. (2014). Rifted continental margins: The case for depth-dependent extension. *Earth and Planetary Science Letters*, *407*, 148–162. https://doi.org/10.1016/J.EPSL.2014.09.032

Illsley-Kemp, F., Bull, J. M., Keir, D., Gerya, T., Pagli, C., Gernon, T., … Kendall, J. M. (2018). Initiation of a Proto-transform Fault Prior to Seafloor Spreading. *Geochemistry, Geophysics, Geosystems*, *19*(12), 4744–4756. https://doi.org/10.1029/2018GC007947

Jammes, S., & Lavier, L. L. (2016). The effect of bimineralic composition on extensional processes at lithospheric scale. *Geochemistry, Geophysics, Geosystems*, *17*(8), 3375–3392. https://doi.org/10.1002/2016GC006399

Jolie, E., Scott, S., Faulds, J., Chambefort, I., Axelsson, G., Gutiérrez-Negrín, L. C., … Zemedkun, M. T. (2021). Geological controls on geothermal resources for power generation. *Nature Reviews Earth & Environment 2021 2:5*, *2*(5), 324–339. https://doi.org/10.1038/s43017-021-00154-y

Jourdon, A, Kergaravat, C., Duclaux, G., & Huguen, C. (2021). Looking beyond kinematics: 3D thermo-mechanical modelling reveals the dynamics of transform margins. *Solid Earth*, *12*(5), 1211–1232. https://doi.org/10.5194/se-12-1211-2021

Jourdon, Anthony, Le Pourhiet, L., Mouthereau, F., & May, D. (2020). Modes of Propagation of Continental Breakup and Associated Oblique Rift Structures. *Journal of Geophysical Research: Solid Earth*, *125*(9), 1–27. https://doi.org/10.1029/2020JB019906

Karato, S., & Wu, P. (1993). Rheology the Upper Mantle : Synthesis, *260*(May).

Katz, R. F., Ragnarsson, R., & Bodenschatz, E. (2005). Tectonic microplates in a wax model of sea-floor spreading. *New Journal of Physics*, *7*. https://doi.org/10.1088/1367-2630/7/1/037

Kaus, B. J. P., Popov, A. A., Baumann, T. S., Pusok, A. E., Bauville, A., Fernandez, N., & Collignon, M. (2016). Forward and Inverse Modelling of Lithospheric Deformation on Geological Timescales, *48*, undefined-undefined. Retrieved from https://www.mendeley.com/catalogue/08bd7b8a-748b-39df-8664-6c03eecd0665/?utm_source=desktop&utm_medium=1.19.8&utm_campaign=open_catalog&userDocumentId=%7B1514b609-6e07-42b5-902b-6038caea45ae%7D

Keary, P., Klepeis, K. A., & Vine, F. J. (2009). *Global Tectonics*. John Wiley & Sons, LTD.

Keen, C., & de Voogd, B. (1988). The continent-ocean boundary at the rifted margin of eastern Canada: new results from deep seismic reflection stud- ies. *Tectonics*, *7*, 107–124.

King, M. T., Welford, J. K., & Peace, A. L. (2020). Investigating the role of the Galicia Bank on the formation of the North West Iberian margin using deformable plate tectonic models. *Tectonophysics*, *789*, 228537. https://doi.org/10.1016/j.tecto.2020.228537

Klingelhoefer, F., Evain, M., Afilhado, A., Rigoti, C., Loureiro, A., Alves, D., … Aslanian, D. (2014). Imaging Proto-Oceanic Crust off the Brazilian Continental Margin. *Geophysical Journal International*, *200*(1), 471–488. https://doi.org/10.1093/gji/ggu387

Koptev, A. I., & Ershov, A. V. (2011). Thermal thickness of the Earth's lithosphere: a numerical model. *Moscow University Geology Bulletin*, *66*(5), 323–330. https://doi.org/10.3103/S014587521105005X

Koptev, A, Calais, E., Burov, E., Leroy, S., & Gerya, T. (2015). Dual continental rift systems generated by plume–lithosphere interaction. *Nature Geoscience*, *8*(5), 388–392. https://doi.org/10.1038/ngeo2401

Koptev, Alexander, Burov, E., Gerya, T., Le Pourhiet, L., Leroy, S., Calais, E., & Jolivet, L. (2018). Plume-induced continental rifting and break-up in ultra-slow extension context: Insights from 3D numerical modeling. *Tectonophysics*, *746*, 121–137. https://doi.org/10.1016/j.tecto.2017.03.025

Krob, F. C., Glasmacher, U. A., Bunge, H.-P., Friedrich, A. M., & Hackspacher, P. C. (2020). Application of Stratigraphic Frameworks and Thermochronological Data on the Mesozoic SW Gondwana Intraplate Environment to Retrieve the {{Paraná}}-{{Etendeka}} Plume Movement. *Gondwana Research*, *84*, 81–110. https://doi.org/10.1016/j.gr.2020.02.010

Kronbichler, M., Heister, T., & Bangerth, W. (2012). High Accuracy Mantle Convection Simulation through Modern Numerical Methods. *Geophysical Journal International*, *191*. https://doi.org/doi:10.1111/j.1365-246x.2012.05609.x.

Kumar, N., & Gambôa, L. a. P. (1979). Evolution of the São Paulo Plateau (Southeastern Brazilian Margin) and Implications for the Early History of the South Atlantic. *GSA Bulletin*, *90*(3), 281–293. https://doi.org/10.1130/0016-7606(1979)90<281:EOTSPP>2.0.CO;2

Lamb, S., & Davis, P. (2003). Cenozoic climate change as a possible cause for the rise of the Andes. *Nature*, *425*(6960), 792–797. https://doi.org/10.1038/nature02049

Lau, K. H., Watremez, L., E., L. K. ., & Nedimovic, M. R. (2015). Structure of thinned continental crust across the Orphan Basin from a dense wide- angle seismic profile and gravity data. *Geophysical Journal International*, *202*, 1969–1992.

Lavecchia, A., Thieulot, C., Beekman, F., Cloetingh, S., & Clark, S. (2017). Lithosphere erosion and continental breakup: Interaction of extension, plume upwelling and melting. *Earth and Planetary Science Letters*, *467*, 89–98. https://doi.org/10.1016/j.epsl.2017.03.028

Lavier, L. L., & Manatschal, G. (2006). A mechanism to thin the continental lithosphere at magma-poor margins. *Nature*, *440*(7082), 324–328. https://doi.org/10.1038/nature04608

Le Calvez, J. H., & Vendeville, B. C. (2002). Experimental designs to model along- strike fault interaction. *Journal of the Virtual Explorer*, *7*(November). https://doi.org/10.3809/jvirtex.2002.00043

Le Fort, P. (1975). Himalayas: the collided range. Present knowledge of the continental arc. *American Journal of Science*, 1–44.

Le Pichon, X., Sibuet, J. C., & Francheteau, J. (1977). The fit of continent around the North Atlantic Ocean. *Tectonophysics*, *38*.

Le Pourhiet, L., Chamot-Rooke, N., Delescluse, M., May, D. A., Watremez, L., & Pubellier, M. (2018). Continental break-up of the South China Sea stalled by far-field compression. *Nature Geoscience*, *11*(8), 605–609. https://doi.org/10.1038/s41561-018-0178-5

Le Pourhiet, L., May, D. A., Huille, L., Watremez, L., & Leroy, S. (2017). A genetic link between transform and hyper-extended margins. *Earth and Planetary Science Letters*, *465*, 184–192. https://doi.org/10.1016/j.epsl.2017.02.043

Leeder, M. R., & Gawthorpe, R. L. (1987). Sedimentary models for extensional tilt-block/half-graben basins. *Geological Society, London, Special Publications*, *28*(1), 139 LP – 152. https://doi.org/10.1144/GSL.SP.1987.028.01.11

Lefeuvre, N., Truche, L., Donzé, F. V., Ducoux, M., Barré, G., Fakoury, R. A., … Gaucher, E. C. (2021). Native H2 Exploration in the Western Pyrenean Foothills. *Geochemistry, Geophysics, Geosystems*, *22*(8), e2021GC009917. https://doi.org/10.1029/2021GC009917

Lithospheric Strength and Rift Migration Controls on Synrift Stratigraphy and Breakup Unconformities at Rifted Margins: Examples From Numerical Models, the Atlantic and South China Sea Margins - Pérez-Gussinyé - 2020 - Tectonics - Wiley Online Library. (n.d.). Retrieved November 15, 2021, from https://agupubs.onlinelibrary.wiley.com/doi/full/10.1029/2020TC006255

Longley, I.M. Buessenschuett, C. Clydsdale, L., Cubitt, C. J., Davis, R. C., Johnson, M. K., Marshall, N. M., Murray, A. P., … Thompson, N. B. (2002). The North West Shelf of Australia - A Woodside Perspective. *In M. Keep and S. Moss, Editors, The Sedimentary Basins of Western Australia 3, Volume 3 of Proceedings of the Petroleum Exploration Society of Australia Symposium, Perth, Petroleum Exploration Society of Australia.*, *3*. Retrieved from http://www.searchanddiscovery.com/documents/longley/.

Lymer, G., Cresswell, D. J. F., Reston, T. J., Bull, J. M., Sawyer, D. S., Morgan, J. K., … Shillington, D. J. (2019). 3D development of detachment faulting during continental breakup. *Earth and Planetary Science Letters*, *515*, 90–99. https://doi.org/10.1016/j.epsl.2019.03.018

Macdonald, K. C., Scheirer, D. S., & Carbotte, S. M. (1991). Mid-ocean ridges: Discontinuities, segments and giant cracks. *Science*, *253*(5023), 986–994. https://doi.org/10.1126/science.253.5023.986

Magee, C., Pichel, L. M., Madden-Nadeau, A. L., Jackson, C. A.-L., & Mohriak, W. (2021). Salt–magma interactions influence intrusion distribution and salt tectonics in the Santos Basin, offshore Brazil. *Basin Research*, *n/a*(n/a). https://doi.org/https://doi.org/10.1111/bre.12537

Mahattanachai, T., Morley, C. K., Charusiri, P., & Kanjanapayont, P. (2021). The Andaman Basin Central Fault Zone, Andaman Sea: Characteristics of a major deepwater strike-slip fault system in a polyphase rift. *Marine and Petroleum Geology*, 104997. https://doi.org/10.1016/j.marpetgeo.2021.104997

Maniatis, G., Kurfeß, D., Hampel, A., & Heidbach, O. (2009). Slip acceleration on normal faults due to erosion and sedimentation - Results from a new three-dimensional numerical model coupling tectonics and landscape evolution. *Earth and Planetary Science Letters*,

284(3–4), 570–582. https://doi.org/10.1016/J.EPSL.2009.05.024

Mann, P., Hempton, M. R., Dwight, C. B., & Burke, K. (1983). Development of Pull-Apart Basins Authors: Paul Mann , Mark R . Hempton , Dwight C . Bradley and Kevin Burke Published by : The University of Chicago Press Stable URL : http://www.jstor.org/stable/30064017 . All use subject to JSTOR Terms and Conditio. *The Journal of Geology*, *91*(5), 529–554.

Mansour, J., Giordani, J., Moresi, L., Beucher, R., Kaluza, O., Velic, M., … Beall, A. (2020). Underworld2: Python Geodynamics Modelling for Desktop, HPC and Cloud. *Journal of Open Source Software*, *5*(47), 1797. https://doi.org/10.21105/JOSS.01797

Martin, Y. (2000). Modelling hillslope evolution: linear and nonlinear transport relations. *Geomorphology*, *34*(1–2), 1–21. https://doi.org/10.1016/S0169-555X(99)00127-0

Martinez, F., & Taylor, B. (1996). Backarc spreading, rifting, and microplate rotation, between transform faults in the Manus Basin. *Marine Geophysical Researches*, *18*(2), 203–224. https://doi.org/10.1007/BF00286078

Maurin, T., Masson, F., Rangin, C., Min, U. T., & Collard, P. (2010). First global positioning system results in northern Myanmar: Constant and localized slip rate along the Sagaing fault. *Geology*, *38*(7), 591–594. https://doi.org/10.1130/G30872.1

May, D. A., Brown, J., & Le Pourhiet, L. (2015). A scalable, matrix-free multigrid preconditioner for finite element discretizations of heterogeneous Stokes flow. *Computer Methods in Applied Mechanics and Engineering*, *290*, 496–523. https://doi.org/10.1016/J.CMA.2015.03.014

May, Dave A., Brown, J., & Le Pourhiet, L. (2014). PTatin3D: High-Performance Methods for Long-Term Lithospheric Dynamics. *International Conference for High Performance Computing, Networking, Storage and Analysis, SC*, *2015-January*(January), 274–284. https://doi.org/10.1109/SC.2014.28

McClay, K., & Bonora, M. (2001). Analog models of restraining stepovers in strike-slip fault systems. *AAPG Bulletin*, *85*(2), 233–260. https://doi.org/10.1306/8626c7ad-173b-11d7-8645000102c1865d

McDermott, K., & Reston, T. (2015). To see, or not to see? Rifted margin extension. *Geology*, *43*(11), 967–970. https://doi.org/10.1130/G36982.1

McKenzie, D. (1978). Some remarks on the development of sedimentary basins. *Earth and Planetary Science Letters*, *40*(1), 25–32. https://doi.org/10.1016/0012-821X(78)90071-7

Meisling, K. E., Cobbold, P. R., & Mount, V. S. (2001). Reactivation of an Obliquely Rifted Margin, Campos and Santos Basins, Southeastern Brazil. *AAPG Bulletin*, *85*, 1903–1924. https://doi.org/10.1306/8626D0B3-173B-11D7-8645000102C1865D

Mohriak, W. U., J. M. Macedo, R. T. Castellani, H. D. Rangel, A. Z. N. Barros, M. A. L., Latgé, J. A. Ricci, A. M. P. Mizusaki, P. Szatmari, L. S. Demercian, J. G. R., & Aires, J. R. (1995). Salt Tectonics and Structural Styles in the Deep-Water Province of the Cabo Frio Region, Rio de Janeiro, Brazil. *Salt Tectonics: A Global Perspective*, (July 2015), 273–304. https://doi.org/10.1306/m65604c13

Mohriak, W. U., Nóbrega, M., Odegard, M. E., Gomes, B. S., & Dickson, W. G. (2010). Geological and Geophysical Interpretation of the Rio Grande Rise, South-Eastern Brazilian Margin: Extensional Tectonics and Rifting of Continental and Oceanic Crusts.

Petroleum Geoscience, *16*(3), 231–245. https://doi.org/10.1144/1354-079309-910

Mooney, W. D. (2010). *Crust and Lithospheric Structure - Global Crustal Structure. Treatise on Geophysics: Second Edition* (Vol. 1). Published by Elsevier Inc. https://doi.org/10.1016/B978-0-444-53802-4.00010-5

Moreira, J. L. P., Madeira, C. V., Gil, J. A., & Machado, M. A. P. (2007). Bacia de Santos. *Boletim de Geociências Da Petrobras*, *15*(2), 531–549. Retrieved from http://publicacoes.petrobras.com.br/main.jsp?lumPageId=8A9E308F545405DE0154A04B46AD0C9E&lumItemId=8A9D2A985A2833C5015B1A2064E029CF&previewItemId=8A9D2A985A2833C5015B1A2064D529CE&publicacaoId=8A9D2AAF5A284744015A2958DE4D3BC9#

Morley, C. K. (2016). The impact of multiple extension events, stress rotation and inherited fabrics on normal fault geometries and evolution in the Cenozoic rift basins of Thailand. *Geological Society, London, Special Publications*, *439*, 413–445. https://doi.org/https://doi.org/10.1144/SP439.3

Morley, C. K. (2017). Cenozoic rifting, passive margin development and strike-slip faulting in the Andaman Sea: A discussion of established v. New tectonic models. *Geological Society Memoir*, *47*(1), 27–50. https://doi.org/10.1144/M47.4

Morley, C. K., & Alvey, A. (2015). Is spreading prolonged, episodic or incipient in the Andaman Sea? Evidence from deepwater sedimentation. *Journal of Asian Earth Sciences*, *98*, 446–456. https://doi.org/10.1016/j.jseaes.2014.11.033

Morley, C. K., & Arboit, F. (2019). Dating the onset of motion on the Sagaing fault: Evidence from detrital zircon and titanite U-Pb geochronology from the North Minwun Basin, Myanmar. *Geology*, *47*(6), 581–585. https://doi.org/10.1130/G46321.1

Morley, C. K., & Westaway, R. (2006). Subsidence in the super-deep Pattani and Malay basins of Southeast Asia: A coupled model incorporating lower-crustal flow in response to post-rift sediment loading. *Basin Research*, *18*(1), 51–84. https://doi.org/10.1111/j.1365-2117.2006.00285.x

Moulin, M., Aslanian, D., Rabineau, M., & Matias, L. (2013). Kinematic keys of the Santos-Namibe basins. *Geological Society, London, Special Publications*, *369*. https://doi.org/10.1144/SP369.3

Muirhead, J. D., Kattenhorn, S. A., Lee, H., Mana, S., Turrin, B. D., Fischer, T. P., … Stamps, D. S. (2016). Evolution of upper crustal faulting assisted by magmatic volatile release during early-stage continental rift development in the East African Rift. *Geosphere*, *12*(6), 1670–1700. https://doi.org/10.1130/GES01375.1

Muldashev, I. A., Pérez-Gussinyé, M., & de Araújo, M. N. C. (2021). KineDyn: Thermomechanical forward method for validation of seismic interpretations and investigation of dynamics of rifts and rifted margins. *Physics of the Earth and Planetary Interiors*, *317*, 106748. https://doi.org/10.1016/J.PEPI.2021.106748

Müller, R. D., Gaina, C., Roest, W. R., & Hansen, D. L. (2001). A recipe for microcontinent formation. *Geology*, *29*(3), 203–206. https://doi.org/10.1130/0091-7613(2001)029<0203:arfmf>2.0.co;2

Muluneh, A. A., Brune, S., Illsley-Kemp, F., Corti, G., Keir, D., Glerum, A., … Mori, J. (2020). Mechanism for Deep Crustal Seismicity: Insight From Modeling of Deformation

Processes at the Main Ethiopian Rift. *Geochemistry, Geophysics, Geosystems*, *21*(7), e2020GC008935. https://doi.org/https://doi.org/10.1029/2020GC008935

Naar, D. F., & Hey, R. N. (1991). Tectonic evolution of the Easter microplate. *Journal of Geophysical Research*, *96*(B5), 7961–7993. https://doi.org/10.1029/90JB02398

Nagel, T. J., & Buck, W. R. (2004). Symmetric alternative to asymmetric rifting models. *Geology*, *32*(11), 937–940. https://doi.org/10.1130/G20785.1

Naliboff, J., & Buiter, S. J. H. (2015). Rift reactivation and migration during multiphase extension. *Earth and Planetary Science Letters*, *421*, 58–67. https://doi.org/10.1016/j.epsl.2015.03.050

Naliboff, J B, Glerum, A., Brune, S., Péron-Pinvidic, G., & Wrona, T. (2020). Development of 3-D Rift Heterogeneity Through Fault Network Evolution. *Geophysical Research Letters*, *47*(13), e2019GL086611. https://doi.org/https://doi.org/10.1029/2019GL086611

Naliboff, John B., Buiter, S. J. H., Péron-Pinvidic, G., Osmundsen, P. T., & Tetreault, J. (2017). Complex fault interaction controls continental rifting. *Nature Communications*, *8*(1). https://doi.org/10.1038/S41467-017-00904-X

Neuharth, D., Brune, S., Glerum, A., Morley, C. K., Yuan, X. P., & Braun, J. (2021). Flexural strike-slip basins. *GEOLOGY*.

Neves, B. B. de B., Fuck, R. A., Pimentel, M. M., Neves, B. B. de B., Fuck, R. A., & Pimentel, M. M. (2014). The Brasiliano Collage in South America: A Review. *Brazilian Journal of Geology*, *44*(3), 493–518. https://doi.org/10.5327/Z2317-4889201400030010

Nguyen, L. C., Hall, S. A., Bird, D. E., & Ball, P. J. (2016). Reconstruction of the East Africa and Antarctica continental margins. *Journal OfGeophysical Research: Solid Earth*, *121*, 4156–4179.

Nirrengarten, M., Manatschal, G., Tugend, J., Kusznir, N., & Sauter, D. (2018). Kinematic evolution of the southern North Atlantic: implications for the formation of hyperextended rift systems. *Tectonics*, *37*, 89–118.

Noda, A. (2013). Strike-Slip Basin – Its Configuration and Sedimentary Facies. *Mechanism of Sedimentary Basin Formation - Multidisciplinary Approach on Active Plate Margins*, (January). https://doi.org/10.5772/56593

Norton, I. O., Carruthers, D. T., & Hudec, M. R. (2016). Rift to Drift Transition in the South Atlantic Salt Basins: A New Flavor of Oceanic Crust. *Geology*, *44*(1), 55–58. https://doi.org/10.1130/g37265.1

Olive, J.-A. A., Behn, M. D., & Malatesta, L. C. (2014). Modes of extensional faulting controlled by surface processes. *Geophysical Research Letters*, *41*(19), 6725–6733. https://doi.org/https://doi.org/10.1002/2014GL061507

Pasyanos, M. E., Masters, T. . G., Laske, G., & Ma, Z. (2014). LITH1.0: An updated crust and lithospheric model of the Earth. *Journal of Geophysical Research: Solid Earth*, *119*, 2153–2173. https://doi.org/10.1002/2014JB011376.Received

Peace, A. L., Welford, J. K., Ball, P. J., & Nirrengarten, M. (2019). Deformable plate tectonic models of the southern North Atlantic. *Journal of Geodynamics*, *8*, 11–37.

Pérez-Gussinyé, M., Andrés-Martínez, M., Araújo, M., Xin, Y., Armitage, J., & Morgan, J. P.

(2020). Lithospheric Strength and Rift Migration Controls on Synrift Stratigraphy and Breakup Unconformities at Rifted Margins: Examples From Numerical Models, the Atlantic and South China Sea Margins. *Tectonics*, *39*(12), e2020TC006255. https://doi.org/10.1029/2020TC006255

Pérez-Gussinyé, M., Reston, T. J., & Morgan, J. P. (2001). Serpentinization and magmatism during extension at non-volcanic margins: The effect of initial lithospheric structure. *Geological Society Special Publication*, *187*, 551–576. https://doi.org/10.1144/GSL.SP.2001.187.01.27

Pérez-Gussinyé, Marta, Morgan, J. P., Reston, T. J., & Ranero, C. R. (2006). The rift to drift transition at non-volcanic margins: Insights from numerical modelling. *Earth and Planetary Science Letters*, *244*(1–2), 458–473. https://doi.org/10.1016/J.EPSL.2006.01.059

Péron-Pinvidic, G., & Manatschal, G. (2010). From microcontinents to extensional allochthons: Witnesses of how continents rift and break apart. *Petroleum Geoscience*, *16*(3), 189–197. https://doi.org/10.1144/1354-079309-903

Peron-Pinvidic, G., Manatschal, G., & Osmundsen, P. T. (2013). Structural comparison of archetypal Atlantic rifted margins: A review of observations and concepts. *Marine and Petroleum Geology*, *43*, 21–47.

Powell, R. E., & Weldon, R. J. (1992). Evolution of the San Andreas Fault. *Annual Review of Earth and Planetary Sciences. Vol. 20*, 431–468. https://doi.org/10.1146/annurev.ea.20.050192.002243

Premarathne, U., Suzuki, N., Ratnayake, N., & Kularathne, C. (2016). BURIAL AND THERMAL HISTORY MODELLING OF THE MANNAR BASIN, OFFSHORE SRI LANKA. *Journal of Petroleum Geology*, *39*(2), 193–213. https://doi.org/https://doi.org/10.1111/jpg.12640

Provost, A.-S., & Houston, H. (2003). Stress orientations in northern and central California: Evidence for the evolution of frictional strength along the San Andreas plate boundary system. *Journal of Geophysical Research: Solid Earth*, *108*(B3), 1–18. https://doi.org/10.1029/2001jb001123

Purucker, M. E., & Dyment, J. (2000). Satellite magnetic anomalies related to seafloor spreading in the South Atlantic Ocean. *Geophysical Research Letters*, *27*(17), 2765–2768. https://doi.org/10.1029/1999GL008437

Püthe, C., & Gerya, T. (2014). Dependence of mid-ocean ridge morphology on spreading rate in numerical 3-D models. *Gondwana Research*, *25*(1), 270–283. https://doi.org/10.1016/j.gr.2013.04.005

Ranero, C. R., & Pérez-Gussinyé, M. (2010). Sequential faulting explains the asymmetry and extension discrepancy of conjugate margins. *Nature*, *468*(7321), 294–299. https://doi.org/10.1038/NATURE09520

Reston, T. J., Booth-Rea, G., Leythaeuser, T., Sawyer, D., Klaeschen, D., & Long, C. (2007). Movement along a low-angle normal fault: The S reflector west of Spain. *Geochemistry, Geophysics, Geosystems*, *8*(6). https://doi.org/10.1029/2006GC001437

Reston, T. J., & Pérez-Gussinyé, M. (2007). Lithospheric extension from rifting to continental breakup at magma-poor margins: Rheology, serpentinisation and symmetry. *International*

Journal of Earth Sciences, *96*(6), 1033–1046. https://doi.org/10.1007/S00531-006-0161-Z/FIGURES/9

Reston, Tim J. (2010). The opening of the central segment of the South Atlantic: Symmetry and the extension discrepancy. *Petroleum Geoscience*, *16*(3), 199–206. https://doi.org/10.1144/1354-079309-907

Richter, M. J. E. A., Brune, S., Riedl, S., Glerum, A., Neuharth, D., & Strecker, M. R. (2021). Controls on Asymmetric Rift Dynamics: Numerical Modeling of Strain Localization and Fault Evolution in the Kenya Rift. *Tectonics*, *40*(5), e2020TC006553. https://doi.org/10.1029/2020TC006553

Rose, I., Buffett, B., & Heister, T. (2017). Stability and Accuracy of Free Surface Time Integration in Viscous Flows. *Physics of the Earth and Planetary Interiors*, *262*, 90–100. https://doi.org/doi:10.1016/j.pepi.2016.11.007

Rouby, D., Braun, J., Robin, C., Dauteuil, O., & Deschamps, F. (2013). Long-term stratigraphic evolution of Atlantic-type passive margins: A numerical approach of interactions between surface processes, flexural isostasy and 3D thermal subsidence. *Tectonophysics*, *604*, 83–103. https://doi.org/10.1016/j.tecto.2013.02.003

Rutter, E. H., & Brodie, K. H. (2004). Experimental grain size-sensitive flow of hot-pressed Brazilian quartz aggregates. *Journal of Structural Geology*, *26*(11), 2011–2023. https://doi.org/10.1016/j.jsg.2004.04.006

Ryan, W. B. F., Carbotte, S. M., Coplan, J. O., O'Hara, S., Melkonian, A., Arko, R., … Zemsky, R. (2009). Global Multi-Resolution Topography synthesis. *Geochemistry, Geophysics, Geosystems*, *10*(3). https://doi.org/https://doi.org/10.1029/2008GC002332

Rybacki, E., Gottschalk, M., Wirth, R., & Dresen, G. (2006). Influence of water fugacity and activation volume on the flow properties of fine-grained anorthite aggregates. *Journal of Geophysical Research: Solid Earth*, *111*(3). https://doi.org/10.1029/2005JB003663

Salles, T. (2016). Badlands: A parallel basin and landscape dynamics model. *SoftwareX*, *5*, 195–202. https://doi.org/10.1016/J.SOFTX.2016.08.005

Sandiford, D., Brune, S., Glerum, A., Naliboff, J., & Joanne, M. (2021). Kinematics of footwall exhumation at oceanic detachment faults : solid-block rotation and apparent unbending. *[Preprint]*, 1–25. https://doi.org/https://doi.org/10.1002/essoar.10506103.1

Scholz, C. H. (2019). *The mechanics of earthquakes and faulting*. Cambridge university press.

Schouten, H., Klitgord, K., Gallo, G. (1993). Edge-Driven Microplate Kinematics. *Journal of Geophysical Research*, *98*, 6689–6701.

Scotchman, I. C., Gilchrist, G., Kusznir, N. J., Roberts, A. M., & Fletcher, R. (2010). The Breakup of the South Atlantic Ocean: Formation of Failed Spreading Axes and Blocks of Thinned Continental Crust in the Santos Basin, Brazil and Its Consequences for Petroleum System Development. *Petroleum Geology Conference Series*, *7*, 855–866. https://doi.org/10.1144/0070855

Seeber, L., Emre, O., Cormier, M. H., Sorlien, C. C., McHugh, C. M. G., Polonia, A., … Cagatay, N. (2004). Uplift and subsidence from oblique slip: The Ganos-Marmara bend of the North Anatolian Transform, Western Turkey. *Tectonophysics*, *391*(1-4 SPEC.ISS.), 239–258. https://doi.org/10.1016/j.tecto.2004.07.015

SERPA, L., DE VOOGD, B., WRIGHT, L., WILLEMIN, J., OLIVER, J., HAUSER, E., & TROXEL, B. (1988). Structure of the central Death Valley pull-apart basin and vicinity from COCORP profiles in the southern Great Basin. *GSA Bulletin*, *100*(9), 1437–1450. https://doi.org/10.1130/0016-7606(1988)100<1437:SOTCDV>2.3.CO;2

Sibuet, J.-C., Srivastava, S. P., & Spakman, W. (2004). Pyrenean orogeny and plate kinematics. *Journal of Geophysical Research: Solid Earth*, *109*(8), 1–18. https://doi.org/10.1029/2003JB002514

Sibuet, J. C. (1992). New constraints on the formation of the non-volcanic continental Galicia–Flemish Cap conjugate margins. *Journal of the Geological Society*, *149*(5), 829–840. https://doi.org/10.1144/GSJGS.149.5.0829

Sibuet, J. C., Srivastava, S. P., Enachescu, M., & Karner, G. D. (2007). Early Cretaceous motion of Flemish Cap with respect to North America: Implications on the formation of Orphan Basin and SE Flemish Cap-Galicia Bank conjugate margins. *Geological Society Special Publication*, *282*, 63–76. https://doi.org/10.1144/SP282.4

Sippel, J., Meeßen, C., Cacace, M., Mechie, J., Fishwick, S., Heine, C., … Strecker, M. (2017). The Kenya rift revisited: Insights into lithospheric strength through data-driven 3-D gravity and thermal modelling. *Solid Earth*, *8*, 45–81. https://doi.org/10.5194/se-8-45-2017

Sobolev, S. V., Petrunin, A., Garfunkel, Z., & Babeyko, A. Y. (2005). Thermo-mechanical model of the Dead Sea Transform. *Earth and Planetary Science Letters*, *238*(1–2), 78–95. https://doi.org/10.1016/j.epsl.2005.06.058

Sobolev, Stephan V., & Brown, M. (2019). Surface erosion events controlled the evolution of plate tectonics on Earth. *Nature 2019 570:7759*, *570*(7759), 52–57. https://doi.org/10.1038/s41586-019-1258-4

Srisuriyon, K., & Morley, C. K. (2014). Pull-apart development at overlapping fault tips: Oblique rifting of a Cenozoic continental margin, northern Mergui Basin, Andaman Sea. *Geosphere*, *10*(1), 80–106. https://doi.org/10.1130/GES00926.1

Srivastava, S., Roest, W., Kovacs, L., Oakey, G., Le vesque, S., Verhoef, J., & Macnab, R. (1990). Motion of Iberia since the Late Jurassic: results from detailed aeromagnetic measurements in the Newfoundland Basin. *Tectonophysics*, *184*, 229–260.

Srivastava, S., & Verhoef, J. (1992). Evolution of Mesozoic sedimentary basins around the North Central Atlantic: a preliminary plate kinematic solution. *Geological Society, London, Special Publications*, *62*, 397–420.

Stamps, D. S., Flesch, L. M., & Calais, E. (2010). Lithospheric buoyancy forces in Africa from a thin sheet approach. *International Journal of Earth Sciences*, *99*(7), 1525–1533. https://doi.org/10.1007/S00531-010-0533-2/FIGURES/6

Stamps, D. Sarah, Calais, E., Saria, E., Hartnady, C., Nocquet, J. M., Ebinger, C. J., & Fernandes, R. M. (2008). A kinematic model for the East African Rift. *Geophysical Research Letters*, *35*, 1–6. https://doi.org/10.1029/2007GL032781

Stamps, D S, Kreemer, C., Fernandes, R., Rajaonarison, T. A., & Rambolamanana, G. (2021). Redefining East African Rift System kinematics. *Geology*, *49*(2), 150–155. https://doi.org/10.1130/G47985.1

Stanca, R. M., Paton, D. A., Hodgson, D. M., McCarthy, D. J., & Mortimer, E. J. (2019). A

revised position for the rotated Falkland Islands microplate. *Journal of the Geological Society*, *176*(3), 417–429. https://doi.org/10.1144/jgs2018-163

Steinberger, B., Bredow, E., Lebedev, S., Schaeffer, A., & Torsvik, T. H. (2019). Widespread volcanism in the Greenland–North Atlantic region explained by the Iceland plume. *Nature Geoscience*, *12*(1), 61–68. https://doi.org/10.1038/s41561-018-0251-0

Stern, R. J., & Johnson, P. R. (2019). Constraining the Opening of the Red Sea: Evidence from the Neoproterozoic Margins and Cenozoic Magmatism for a Volcanic Rifted Margin. *Geological Setting, Palaeoenvironment and Archaeology of the Red Sea*, 53–79. https://doi.org/10.1007/978-3-319-99408-6_4

Stock, J. D., & Montgomery, D. R. (1999). Geologic constraints on bedrock river incision using the stream power law. *Journal of Geophysical Research: Solid Earth*, *104*(B3), 4983–4993.

Svartman Dias, A. E., Lavier, L. L., & Hayman, N. W. (2015). Conjugate rifted margins width and asymmetry: The interplay between lithospheric strength and thermomechanical processes. *Journal of Geophysical Research: Solid Earth*, *120*, 8672–8700. https://doi.org/doi:10.1002/2015JB012074

Szatmari, P., & Milani, E. J. (1999). Microplate rotation in northeast Brazil during South Atlantic rifting: Analogies with the Sinai microplate. *Geology*, *27*(12), 1115–1118. https://doi.org/10.1130/0091-7613(1999)027<1115:MRINBD>2.3.CO;2

Tentler, T. (2003). Analogue modeling of overlapping spreading centers: Insights into their propagation and coalescence. *Tectonophysics*, *376*(1–2), 99–115. https://doi.org/10.1016/j.tecto.2003.08.011

Tentler, T., & Acocella, V. (2010). How does the initial configuration of oceanic ridge segments affect their interaction ? Insights from analogue models, *115*. https://doi.org/10.1029/2008JB006269

Tetreault, J. L., & Buiter, S. J. H. (2018). The influence of extension rate and crustal rheology on the evolution of passive margins from rifting to break-up. *Tectonophysics*, *746*, 155–172. https://doi.org/10.1016/j.tecto.2017.08.029

Thatcher, W. (2007). Microplate model for the present-day deformation of Tibet. *Journal of Geophysical Research: Solid Earth*, *112*(1), 1–13. https://doi.org/10.1029/2005JB004244

Theunissen, T., & Huismans, R. S. (2019). Long-Term Coupling and Feedback Between Tectonics and Surface Processes During Non-Volcanic Rifted Margin Formation. *Journal of Geophysical Research: Solid Earth*, *124*(11), 12323–12347. https://doi.org/10.1029/2018JB017235

Turcotte, D. L., & Schubert, G. (2013). *Geodynamics* (3rd ed.). Cambridge University Press.

van Wijk, J., Axen, G., & Abera, R. (2017). Initiation, evolution and extinction of pull-apart basins: Implications for opening of the Gulf of California. *Tectonophysics*, *719–720*, 37–50. https://doi.org/10.1016/j.tecto.2017.04.019

Vendeville, B., & Le Calvez, J. (1995). Physical models of normal-fault relays between variably offset grabens. *AAPG Bulletin*, *79*.

Vigny, C., Socquet, A., Rangin, C., Chamot-Rooke, N., Pubellier, M., Bouin, M.-N., … Becker, M. (2003). Present-day crustal deformation around Sagaing fault, Myanmar.

Journal of Geophysical Research: Solid Earth, *108*(B11). https://doi.org/https://doi.org/10.1029/2002JB001999

Watremez, L., Lau, K. H., Nedimovic, M. R., & Louden, K. E. (2015). Traveltime tomography of a dense wide-angle profile across Orphan Basin. *Geophysics*, *80(3)*, B69–B82.

Welford, J. K., Dehler, S. A., & Funck, T. (2020). Crustal velocity structure across the Orphan Basin and Orphan Knoll to the continent–ocean transition, offshore Newfoundland, Canada. *Geophysical Journal International*, *221*(1), 37–59. https://doi.org/10.1093/gji/ggz575

Welford, J. K., Shannon, P. M., O'Reilly, B. M., & Hall, J. (2012). Comparison of lithosphere structure across the Orphan Basin-Flemish Cap and Irish Atlantic conjugate continental margins from constrained 3D gravity inversions. *Journal of the Geological Society*, *169*(4), 405–420. https://doi.org/10.1144/0016-76492011-114

Wessel, P., Luis, J. F., Uieda, L., Scharroo, R., Wobbe, F., Smith, W. H. F., & Tian, D. (2019). The Generic Mapping Tools Version 6. *Geochemistry, Geophysics, Geosystems*, *20*(11), 5556–5564. https://doi.org/https://doi.org/10.1029/2019GC008515

Whipple, K. X., & Tucker, G. E. (1999a). Dynamics of the stream-power river incision model: Implications for height limits of mountain ranges, landscape response timescales, and research needs. *Journal of Geophysical Research: Solid Earth*, *104*(B8), 17661–17674. https://doi.org/10.1029/1999JB900120

Whipple, K. X., & Tucker, G. E. (1999b). Dynamics of the stream-power river incision model: Implications for height limits of mountain ranges, landscape response timescales, and research needs. *Journal of Geophysical Research: Solid Earth*, *104*(B8), 17661–17674.

Whitmarsh, R. B., Manatschal, G., & Minshull, T. A. (2001). Evolution of magma-poor continental margins from rifting to seafloor spreading. *Nature 2001 413:6852*, *413*(6852), 150–154. https://doi.org/10.1038/35093085

Wilkinson, J. J. (2014). Sediment-Hosted Zinc–Lead Mineralization: Processes and Perspectives. *Treatise on Geochemistry: Second Edition*, *13*, 219–249. https://doi.org/10.1016/B978-0-08-095975-7.01109-8

Williams, H. (1984). Miogeoclines and suspect terranes of the Caledonian- Appalachian orogen: tectonic patterns in the North Atlantic region. *Canadian Journal of Earth Sciences*, *21*, 887–901.

Williams, H. (1995). Geology of the Appalachian-Caledonian orogen in Canada and Greenland. *Geological Survey of Canada, Geology of Canada*, *6*.

Williams, J. N., Fagereng, Å., Wedmore, L. N. J., Biggs, J., Mphepo, F., Dulanya, Z., … Blenkinsop, T. (2019). How Do Variably Striking Faults Reactivate During Rifting? Insights From Southern Malawi. *Geochemistry, Geophysics, Geosystems*, *20*(7), 3588–3607. https://doi.org/10.1029/2019GC008219

Wolf, S. G., Huismans, R. S., Muñoz, J. A., Curry, M. E., & van der Beek, P. (2021). Growth of Collisional Orogens From Small and Cold to Large and Hot—Inferences From Geodynamic Models. *Journal of Geophysical Research: Solid Earth*, *126*(2), e2020JB021168. https://doi.org/10.1029/2020JB021168

Wu, K., Otoo, E., & Suzuki, K. (2009). Optimizing two-pass connected-component labeling algorithms. *Pattern Analysis and Applications*, *12*(2), 117–135.

https://doi.org/10.1007/S10044-008-0109-Y/FIGURES/8

Yang, P., & Welford, J. K. (2021). Investigating the Porcupine Atlantic margin, offshore Ireland, through integration of new seismic reflection and gravity data. *Tectonophysics*, *807*, 228809. https://doi.org/10.1016/j.tecto.2021.228809

Yuan, X. P., Braun, J., Guerit, L., Rouby, D., & Cordonnier, G. (2019a). A New Efficient Method to Solve the Stream Power Law Model Taking Into Account Sediment Deposition. *Journal of Geophysical Research: Earth Surface*, *124*(6), 1346–1365. https://doi.org/10.1029/2018JF004867

Yuan, X. P., Braun, J., Guerit, L., Rouby, D., & Cordonnier, G. (2019b). A New Efficient Method to Solve the Stream Power Law Model Taking Into Account Sediment Deposition. *Journal of Geophysical Research: Earth Surface*, *124*(6), 1346–1365. https://doi.org/10.1029/2018JF004867

Yuan, X. P., Braun, J., Guerit, L., Simon, B., Bovy, B., Rouby, D., … Jiao, R. (2019). Linking continental erosion to marine sediment transport and deposition: A new implicit and O(N) method for inverse analysis. *Earth and Planetary Science Letters*, *524*(August), 115728. https://doi.org/10.1016/j.epsl.2019.115728

Zalán, P. V, Severino, M. do C. G., Rigoti, C. A., Magnavita, L. P., de Oliveira, J. A. B., & Vianna, A. R. (2011). An Entirely New 3D-View of the Crustal and Mantle Structure of a South Atlantic Passive Margin – Santos, Campos and Espírito Santo Basins, Brazil (p. Search and Discovery Article #30177). AAPG.

Zoback, M. D., Zoback, M. Lou, Van Mount, S., Suppe, J., Eaton, J. P., Healy, J. H., … Wentworth, C. (1987). New evidence on the state of stress of the san andreas fault system. *Science*, *238*(4830), 1105–1111. https://doi.org/10.1126/science.238.4830.1105

Zwaan, F., & Schreurs, G. (2017). How oblique extension and structural inheritance influence rift segment interaction: Insights from 4D analog models, *5*(1), 119–138.

Zwaan, F., & Schreurs, G. (2020). Rift segment interaction in orthogonal and rotational extension experiments: Implications for the large-scale development of rift systems. *Journal of Structural Geology*, *140*(March). https://doi.org/10.1016/j.jsg.2020.104119

Zwaan, F., Schreurs, G., & Adam, J. (2018). Effects of sedimentation on rift segment evolution and rift interaction in orthogonal and oblique extensional settings: Insights from analogue models analysed with 4D X-ray computed tomography and digital volume correlation techniques. *Global and Planetary Change*, *171*(November), 110–133. https://doi.org/10.1016/j.gloplacha.2017.11.002

Zwaan, F., Schreurs, G., Naliboff, J., & Buiter, S. J. H. (2016). Insights into the effects of oblique extension on continental rift interaction from 3D analogue and numerical models. *Tectonophysics*, *693*, 239–260. https://doi.org/10.1016/j.tecto.2016.02.036

Acknowledgements

This study was conducted within the Helmholtz Young Investigators Group CRYSTALS (grant VH-NG-1132) and used the North-German Supercomputing Alliance (HLRN, https://www.hlrn.de/) cluster for running models, and I would like to thank both institutions for their support. Without their resources, this work would not have been possible.

First and foremost, I sincerely thank Dr. Sascha Brune and Dr. Anne Glerum for the opportunity to study at GFZ Potsdam, and the immense amount of help and guidance they have given me throughout my time here. I would also like to thank Dr. Thilo Wrona for his help during the final portion of my stay here. Also, I would like to thank my second supervisor Dr. Stephan Sobolev, my mentor Dr. Judith Bott, and the entirety of section 2.5, I've had a truly great experience working with everyone and I will certainly miss being a part of the section. I would like to thank Dr. Jean Braun and Dr. Xiaoping Yuan, who helped make the ASPECT-FastScape coupling possible, as well as Dr. Chris K. Morley, Dr. J. Kim Welford, and Dr. Christian Heine, who helped with the studies presented in this thesis. I would like to thank some of the friends I've made along the way, Michael Pons, Constanza Rodriguez Piceda, Michele Vallati, Roman Feal, and many more that have helped me throughout my time in Potsdam. Finally, I thank my family who supported me in moving all the way to Germany.